

Evaluation of Geosynthetic Reinforced Flexible Pavement Systems Using Two Pavement Test Facilities

FHWA/MT-02-008/20040

Final Report

Prepared for the
U.S. DEPARTMENT OF TRANSPORTATION
FEDERAL HIGHWAY ADMINISTRATION
and the
STATE OF MONTANA
DEPARTMENT OF TRANSPORTATION
RESEARCH BUREAU

November 22, 2002

Prepared by

Dr. Steven W. Perkins
Associate Professor
Department of Civil Engineering
Western Transportation Institute
Montana State University – Bozeman
Bozeman, Montana 59717
Office Telephone: 406-994-6119
Fax: 406-994-6105
E-Mail: stevep@ce.montana.edu

1. Report No. FHWA/MT-02-008/20040	2. Government Accession No.	3. Recipient's Catalog No.
4. Title and Subtitle Evaluation of Geosynthetic Reinforced Flexible Pavement Systems Using Two Pavement Test Facilities	5. Report Date November 22, 2002	
	6. Performing Organization Code MSU G&C #427870 & #427143	
7. Author Steven W. Perkins, Ph.D., P.E.	8. Performing Organization Report No.	
9. Performing Organization Name and Address Department of Civil Engineering 205 Cobleigh Hall Montana State University Bozeman, Montana 59717	10. Work Unit No.	
	11. Contract or Grant No. 20040	
12. Sponsoring Agency Name and Address Montana Department of Transportation Research Bureau 2701 Prospect Avenue P.O. Box 201001 Helena, Montana 59620-1001	13. Type of Report and Period Covered Final: August 17, 1999 – November 30, 2002	
	14. Sponsoring Agency Code 5401	
15. Supplementary Notes Preparation in cooperation with the U.S. Department of Transportation, Federal Highway Administration		
16. Abstract <p>Montana State University has previously completed experimental test section, numerical modeling and design model development projects for the Montana Department of Transportation. Test section work has led to a fundamental understanding of mechanisms by which geosynthetics provide reinforcement when placed in the aggregate layer of flexible pavements. Finite element numerical models have relied upon this knowledge as their basis while design models derived from these numerical models have been calibrated against results from test sections. The test sections used for the development of these models were limited by the number of subgrade types, geosynthetic types and loading type employed.</p> <p>This project was initiated to provide additional test section data to better define the influence of traffic loading type and geosynthetic reinforcement type. The loading provided to the test sections forming the basis of the models described above consisted of a cyclic load applied to a stationary plate. In this project, four full-scale test sections were constructed and loaded with a heavy vehicle simulator (HVS) located at the US Army Corp of Engineers facility in Hanover, NH. The four test sections used three geosynthetics identical to those used in previous test sections and pavement layer materials and thickness similar to previous sections.</p> <p>Additional test sections were constructed in the pavement test box used in previous studies to examine the influence of base aggregate type, base course thickness reduction levels and reinforcement type. A rounded pit run aggregate was used in test sections to evaluate the influence of geosynthetic-aggregate shear interaction parameters on reinforcement benefit. The 1993 AASHTO Design Guide was used to backcalculate the base course thickness reduction from previous test section results where a traffic benefit ratio (extension of life) was known. Sections were built to this base course thickness reduction to see if equivalent life to an unreinforced section was obtained. Finally, six different geosynthetic products were used in test sections to evaluate the influence of reinforcement type on pavement performance.</p> <p>The four test sections loaded with the HVS tended to show pavement distress that was dominated by surface rutting due to the development of permanent strain in the asphalt concrete, base aggregate and subgrade layers. Several asphalt cracking areas were due to delamination between the binder and surface courses. The order of performance of the test sections generally followed that seen in previous studies. An evaluation of reinforcement benefit in terms of rutting behavior was complicated by the observation of significant differences in rut level between the two ends of a given section for two of the four sections. Benefit values, defined in terms of a Traffic Benefit Ratio (TBR), were similar between these sections and previously constructed sections for the geotextile product used. For sections with geogrid products, TBR was generally lower in the sections loaded with the HVS. The sequence of loading of the sections may have influenced the development of pore water pressure under adjacent sections and had a bearing on the results obtained. Instrumentation contained in the sections tended to show reinforcement mechanisms similar to those observed previously in smaller scale sections.</p> <p>Smaller scale test sections constructed to evaluate base reduction factors where the reduced thickness was based on estimates using the 1993 AASHTO flexible pavement design equations and TBR values from previous tests sections indicated that the use of this approach is largely conservative except for conditions where the aggregate is excessively thin (less than 150 mm in thickness).</p>		

Values of base course reduction from the design model developed previously for the Montana DOT are conservative with respect to the results obtained from this portion of the study.

Unreinforced small scale test sections constructed with a rounded aggregate having a maximum particle size of 38 mm indicated superior performance as compared to unreinforced sections constructed with a crushed aggregate having a maximum particle size of 19 mm. The performance of reinforced sections using the rounded aggregate were generally inferior relative to those using a crushed aggregate. In addition, the order of performance of sections using two geosynthetic types was reversed when using the rounded aggregate. Results from direct shear tests yielding geosynthetic-aggregate interaction properties did not correspond to the results obtained.

The response of the test sections using different geosynthetic products was dominated by pore water pressure generation due to several factors. The subgrade used in these test sections readily develops positive pore water pressure during construction and pavement loading. The initial magnitude of pore water pressure prior to pavement loading has a significant impact on pavement response during loading as defined in terms of rutting. The magnitude of pore water pressure generation during pavement loading appears to be dependent on the initial value of pore water pressure at the start of loading and the set-up time of the subgrade. The initial pore water pressure in turn appears to be dependent on the amount of compaction energy imparted to the constructed layers, the time for construction, and the time between end of construction and start of loading.

The response of the majority of the reinforced sections for this portion of the study was dominated by the pore water pressure issues described above. The last two sections constructed used a technique that involved two loading stages with a significant wait period in between. Results from the first loading stage when set-up time of the subgrade was relatively short showed a rapid development of rut depth and pore water pressure in the subgrade. Loading during the 2nd stage produced a much lower rate of rutting and pore pressure generation. Construction of test sections by this technique when using a subgrade which is highly susceptible to pore water pressure generation is believed to yield a method where comparison of test sections is possible.

17. Key Words

Pavements, Highways, Geogrid, Geotextile, Geosynthetic, Reinforcement, Base Course, Test Section, Instrumentation, Mechanical Response, Montana

18. Distribution Statement

Unrestricted. This document is available through the National Technical Information Service, Springfield, VA 21161.

19. Security Classif. (of this report)

Unclassified

20. Security Classif. (of this page)

Unclassified

21. No. of Pages

120

22. Price

PREFACE

DISCLAIMER STATEMENT

This document is disseminated under the sponsorship of the Montana Department of Transportation and the United States Department of Transportation in the interest of information exchange. The State of Montana and the United States Government assume no liability of its contents or use thereof.

The contents of this report reflect the views of the authors, who are responsible for the facts and accuracy of the data presented herein. The contents do not necessarily reflect the official policies of the Montana Department of Transportation or the United States Department of Transportation

The State of Montana and the United States Government do not endorse products of manufacturers. Trademarks or manufacturers' names appear herein only because they are considered essential to the object of this document

This report does not constitute a standard, specification, or regulation.

ALTERNATIVE FORMAT STATEMENT

The Montana Department of Transportation attempts to provide reasonable accommodations for any known disability that may interfere with a person participating in any service, program, or activity of the Department. Alternative accessible formats of this document will be provided upon request. For further information, call (406)444-7693 or TTY (406)444-7696.

ACKNOWLEDGMENTS

The author gratefully acknowledges the generous financial and technical support of the principal sponsors of this project, the Montana Department of Transportation and the Federal Highway Administration. The author also recognizes the sponsorship offered by the following geosynthetic manufacturers: Colbond, Inc., Synthetic Industries, Ten Cate Nicolon, Tenax Corporation, and Tensar Earth Technologies, Inc. The author is indebted to the following former staff of MSU who contributed to this project: Mr. Jim Penman, Mr. Bill Cowan, Dr. Muhannad Ismeik, Mr. Todd Rorer, Mr. Matt Miller, Mr. Eli Cuelho and Mr. Scott Lee. The author recognizes the services provided under contract by GeoTesting Express, Inc. in the construction of test sections and materials testing and the additional support services provided above and beyond the contract specifications. Finally, the technical support and review services provided by Dr. Barry Christopher are gratefully acknowledged.

TABLE OF CONTENTS

LIST OF TABLES	viii
LIST OF FIGURES	ix
CONVERSION FACTORS	xiii
EXECUTIVE SUMMARY	xiv
1.0 INTRODUCTION	1
2.0 SUMMARY OF PREVIOUS WORK	2
2.1 Test Section Construction	3
2.2 Numerical and Design Model Development	7
3.0 PAVEMENT TEST FACILITIES	9
3.1 CRREL FERF/HVS	9
3.1.1 Facility Geometry and Loading	10
3.1.2 Test Section Construction Process	12
3.1.3 Instrumentation	15
3.2 MSU/GTX Test Box	19
3.2.1 Facility Geometry and Loading	20
3.2.2 Construction Process	22
3.2.3 Instrumentation	23
4.0 PAVEMENT MATERIALS	25
4.1 Asphalt Concrete	25
4.2 Base Aggregate	26
4.3 Subgrade	29
4.4 Geosynthetic	34
4.4.1 Basic Properties	34
4.4.2 Direct Shear Tests	36
5.0 PAVEMENT TEST SECTIONS AND LAYER PROPERTIES	41
5.1 Pavement Test Sections Constructed	41
5.1.1 CRREL FERF/HVS	41
5.1.2 MSU/GTX Test Box	41
5.2 Layer Properties and Quality Control Measures	42
5.2.1 CRREL FERF/HVS	42
5.2.2 MSU/GTX Test Box	54
6.0 RESULTS: CRREL/HVS/FERF	61
6.1 Rutting Behavior	61
6.2 Performance Behavior	68
6.3 Dynamic Response Behavior	79
6.3.1 Dynamic Stress Response	79
6.3.2 Dynamic Strain Response	86
6.4 Permanent Deformation/Strain Behavior	93
7.0 RESULTS: MSU TEST BOX	97
7.1 Thin (T) Sections	97
7.2 Rounded (R) Sections	101
8.0 RESULTS: GTX TEST BOX	102
8.1 Response of Unreinforced Sections	102
8.2 Response of Reinforced Sections	109

9.0 CONCLUSIONS	116
10.0 REFERENCES	120

LIST OF TABLES

Table 2.1.1	Constructed test section variables from Perkins (1999).	4
Table 2.2.1	Design model input parameters.	9
Table 3.1.1	Locations of stress and strain instrumentation.	18
Table 4.2.1	Base aggregate material properties.	27
Table 4.2.2	Base aggregate resilient modulus properties.	28
Table 4.2.3	Base aggregate strength (cohesion, friction angle) properties.	29
Table 4.3.1	Subgrade material properties.	29
Table 4.3.2	Undrained cohesion of GTX subgrade.	33
Table 4.3.3	Undrained cohesion of subgrade materials.	34
Table 4.4.1	Geosynthetics used in test sections.	34
Table 4.4.2	Geosynthetic properties.	35
Table 4.4.3	Geosynthetic/aggregate combinations for direct shear tests.	38
Table 4.4.4	Curve fit parameters, for Equations 4.4.2 and 4.4.3 for all geosynthetic/aggregate combinations.	39
Table 4.4.5	Efficiency coefficients from direct shear tests.	40
Table 5.1.1	CRREL test sections constructed.	41
Table 5.1.2	MSU/GTX test sections constructed.	42
Table 5.2.1	As-constructed asphalt concrete properties for CRREL sections.	43
Table 5.2.2	Temperature during HVS loading and resilient modulus values of asphalt concrete for CRREL sections.	43
Table 5.2.3	As-constructed base aggregate properties sections.	44
Table 5.2.4	As-constructed subgrade properties for CRREL sections.	51
Table 5.2.5	Coefficient of variation of as-constructed subgrade properties for CRREL sections.	51
Table 5.2.6	CBR results from DCP tests taken during excavation in CRREL subgrade.	53
Table 5.2.7	Field CBR results from tests taken during excavation in CRREL subgrade.	53
Table 5.2.8	Portable FWD modulus measurements during excavation in CRREL subgrade.	54
Table 5.2.9	Loading conditions for MSU/GTX sections.	55
Table 5.2.10	As-constructed asphalt concrete properties for MSU/GTX sections.	56
Table 5.2.11	Resilient modulus and tensile strength of asphalt concrete for MSU/GTX sections.	57
Table 5.2.12	General properties of asphalt concrete for MSU/GTX sections.	58
Table 5.2.13	As-constructed base aggregate properties for CRREL sections.	59
Table 5.2.14	As-constructed subgrade properties in MSU/GTX sections.	60
Table 5.2.15	Coefficient of variation of as-constructed subgrade properties for MSU/GTX sections.	61
Table 6.1.1	Traffic Benefit Ratios (TBR) for CRREL sections and from previous studies.	68
Table 6.3.1	Locations of stress sensors in CRREL subgrade.	82

LIST OF FIGURES

Figure 2.1.1	Permanent surface deformation versus load cycle (CS2, 5, 6, 7, 8, 11).	5
Figure 2.1.2	<i>TBR</i> for sections CS5, 6, 7 and 11 relative to section CS2.	5
Figure 2.1.3	Permanent radial strain 50 mm above the bottom of the base versus radial distance at 40,000 load cycles (CS2, CS5).	6
Figure 2.2.1	Lateral permanent strain in the bottom of the base versus lateral distance after 10 cycles of load.	8
Figure 2.2.2	Lateral permanent strain along the load plate centerline versus depth after 10 cycles of load.	8
Figure 3.1.1	Dimensions and locations of test sections	10
Figure 3.1.2	Heavy Vehicle Simulator used for CRREL test sections.	11
Figure 3.1.3	Location of wheel travel path within a test section.	12
Figure 3.1.4	Dimensions of dual tires used on the HVS.	12
Figure 3.1.5	Cross-section dimensions of CRREL test sections.	13
Figure 3.1.6	CRREL subgrade compaction.	14
Figure 3.1.7	CRREL paved test sections	15
Figure 3.1.8	Soil stress cells (Dynatest).	16
Figure 3.1.9	EMU strain coils.	17
Figure 3.2.1	Schematic diagram of the MSU/GTX pavement test facility.	20
Figure 3.2.2	Image of the pavement load plate and surface instrumentation.	21
Figure 3.2.3	Input load pulse and corresponding load cell measurement.	22
Figure 3.2.4	Soil strain cell.	25
Figure 4.2.1	Grain size distribution of base aggregate materials.	27
Figure 4.2.2	Base aggregate strength envelope from triaxial tests.	28
Figure 4.3.1	CBR versus compaction moisture content for the clay subgrade.	30
Figure 4.3.2	MSU and GTX subgrade compaction properties.	31
Figure 4.3.3	MSU subgrade strength envelopes from triaxial tests.	32
Figure 4.3.4	CRREL subgrade strength envelopes from triaxial tests.	32
Figure 4.4.1	Schematic of direct shear box.	36
Figure 4.4.2	Photograph of direct shear box.	36
Figure 4.4.3	Shear stress vs. shear displacement from direct shear tests for CRREL aggregate – geosynthetic A.	38
Figure 4.4.4	Interface shear modulus vs. normal stress for CRREL aggregate – geosynthetic A.	39
Figure 5.2.1	Grain size distribution of CRREL AC aggregate.	44
Figure 5.2.2	Grain size distribution of CRREL base aggregate at the top of the base under the wheel load.	45
Figure 5.2.3	Grain size distribution of CRREL base aggregate at the top of the base 0.6 m away from the wheel travel path.	45
Figure 5.2.4	Grain size distribution of CRREL base aggregate at the bottom of the base under the wheel load.	46
Figure 5.2.5	Grain size distribution of CRREL base aggregate at the bottom of the base 0.6 m away from the wheel travel path.	46
Figure 5.2.6	CBR from DCP tests in north end of section CRREL1 base aggregate a) under wheel load, b) 0.8 m away from centerline of wheel travel path.	47

Figure 5.2.7	CBR from DCP tests in south end of section CRREL1 base aggregate a) under wheel load, b) 0.8 m away from centerline of wheel travel path.	47
Figure 5.2.8	CBR from DCP tests in north end of section CRREL2 base aggregate a) under wheel load, b) 0.8 m away from centerline of wheel travel path.	48
Figure 5.2.9	CBR from DCP tests in south end of section CRREL2 base aggregate a) under wheel load, b) 0.8 m away from centerline of wheel travel path.	48
Figure 5.2.10	CBR from DCP tests in north end of section CRREL3 base aggregate a) under wheel load, b) 0.8 m away from centerline of wheel travel path.	49
Figure 5.2.11	CBR from DCP tests in south end of section CRREL3 base aggregate a) under wheel load, b) 0.8 m away from centerline of wheel travel path.	49
Figure 5.2.12	CBR from DCP tests in north end of section CRREL4 base aggregate a) under wheel load, b) 0.8 m away from centerline of wheel travel path.	50
Figure 5.2.13	CBR from DCP tests in south end of section CRREL4 base aggregate a) under wheel load, b) 0.8 m away from centerline of wheel travel path.	50
Figure 5.2.14	DCP tests in CRREL subgrade during construction.	52
Figure 6.1.1	Averaged and zeroed rut profile for test section CRREL1 (control), location 1, pass level 10,000.	62
Figure 6.1.2	Rut depth vs. position along the wheel path for test section CRREL1 (control).	63
Figure 6.1.3	Rut depth vs. position along the wheel path for test section CRREL2 (geosynthetic G).	64
Figure 6.1.4	Rut depth vs. position along the wheel path for test section CRREL3 (geosynthetic A).	64
Figure 6.1.5	Rut depth vs. position along the wheel path for test section CRREL4 (geosynthetic H).	65
Figure 6.1.6	Average rut depth vs. wheel pass for all CRREL test sections.	67
Figure 6.1.7	Maximum and minimum rut depth vs. wheel pass for all CRREL test sections.	67
Figure 6.2.1	Photo mosaic of section CRREL1 (control).	69
Figure 6.2.2	Photo mosaic of section CRREL2 (geosynthetic G).	70
Figure 6.2.3	Photo mosaic of section CRREL3 (geosynthetic A).	71
Figure 6.2.4	Photo mosaic of section CRREL4 (geosynthetic H).	72
Figure 6.2.5	Photo of all CRREL sections.	73
Figure 6.2.6	Photo of delamination in section CRREL1 (control).	74
Figure 6.2.7	Transverse cracking in test section CRREL3 (geosynthetic A).	75
Figure 6.2.8	Close-up photos of transverse cracking in test section CRREL3 (geosynthetic A).	75
Figure 6.2.9	Vertical shear cracking in test section CRREL3 (geosynthetic A).	76
Figure 6.2.10	Rutting in section CRREL4 (geosynthetic H).	77
Figure 6.2.11	Deformed cross section in section CRREL1 (control).	77
Figure 6.2.12	Cross section through CRREL asphalt concrete.	78
Figure 6.3.1	Vertical stress dynamic response of aggregate at $x=8\text{m}$, $y=4.77\text{m}$, $z=0.293\text{m}$.	80
Figure 6.3.2	Transverse stress dynamic response of aggregate at $x=5.25\text{m}$, $y=4.77\text{m}$, $z=0.18\text{m}$.	80

Figure 6.3.3	Longitudinal stress dynamic response of aggregate at $x=6.1m$, $y=4.77m$, $z=0.146m$.	81
Figure 6.3.4	Dynamic stress response of CRREL aggregate.	81
Figure 6.3.5	Dynamic stress response vs. wheel pass for stress sensor 1.	83
Figure 6.3.6	Dynamic stress response vs. wheel pass for stress sensor 2.	83
Figure 6.3.7	Dynamic stress response vs. wheel pass for stress sensor 3.	84
Figure 6.3.8	Dynamic stress response vs. wheel pass for stress sensor 4.	84
Figure 6.3.9	Dynamic stress response vs. wheel pass for stress sensor 5.	85
Figure 6.3.10	Dynamic stress response vs. lateral distance.	85
Figure 6.3.11	Dynamic vertical strain response vs. sample number for top of subgrade.	86
Figure 6.3.12	Dynamic transverse strain response vs. sample number for bottom of base.	87
Figure 6.3.13	Dynamic longitudinal strain response vs. sample number for bottom of base.	87
Figure 6.3.14	Dynamic vertical strain vs. wheel pass for base/subgrade interlayer.	88
Figure 6.3.15	Dynamic vertical strain vs. wheel pass for top of subgrade.	89
Figure 6.3.16	Dynamic transverse strain vs. wheel pass for bottom of base.	89
Figure 6.3.17	Dynamic vertical strain vs. depth at wheel pass 2500.	91
Figure 6.3.18	Dynamic transverse strain vs. transverse distance at the bottom of the base at wheel pass 2500.	92
Figure 6.3.19	Dynamic transverse strain vs. depth at wheel pass 2500.	93
Figure 6.4.1	Permanent vertical strain vs. wheel pass for middle of base.	94
Figure 6.4.2	Permanent vertical strain vs. wheel pass for base/subgrade interlayer.	94
Figure 6.4.3	Permanent vertical strain vs. wheel pass for top of subgrade.	95
Figure 6.4.4	Permanent vertical strain vs. depth at wheel pass 2500.	95
Figure 6.4.5	Permanent vertical strain vs. depth at wheel pass 10,000.	96
Figure 6.4.6	Permanent vertical strain vs. depth at wheel pass 2500, duplicate sensor set.	96
Figure 6.4.7	Permanent vertical strain vs. depth at wheel pass 10,000, duplicate sensor set.	97
Figure 7.1.1	Permanent surface deformation vs. load cycle for MSU “thin” sections.	99
Figure 7.1.2	Permanent vertical strain in the bottom of the base for T sections.	100
Figure 7.1.3	Permanent vertical strain in the top of the subgrade for T sections.	100
Figure 7.1.4	Dynamic radial strain on the geosynthetics for T sections.	101
Figure 7.2.1	Permanent surface deformation vs. load cycle for R sections.	102
Figure 8.1.1	Permanent surface deformation vs. load cycle for GTX unreinforced sections.	103
Figure 8.1.2	Pore water pressure vs. load cycle for GTX unreinforced sections at location $x=0$, $y=0$, $z=415$ mm.	104
Figure 8.1.3	Pore water pressure vs. load cycle for GTX unreinforced sections at location $x=0$, $y=350$ mm, $z=415$ mm.	105
Figure 8.1.4	Pore water pressure vs. load cycle for GTX unreinforced sections at location $x=0$, $y=0$, $z=675$ mm.	105
Figure 8.1.5	Pore water pressure vs. time during construction for GTX5 at location $x=0$, $y=0$, $z=675$ mm.	106
Figure 8.1.6	Starting value of pore water pressure vs. time from end of subgrade construction to start of loading.	107

Figure 8.1.7	Load cycles for 25, 20 or 12.5 mm rut vs. time from end of construction to start of loading for unreinforced sections.	107
Figure 8.1.8	Pore water pressure vs. rutting for four reinforced sections.	109
Figure 8.1.9	Load cycles for 25, 20 or 12.5 mm rut vs. time from end of construction to start of loading for three reinforced sections.	109
Figure 8.2.1	Pore water pressure vs. load cycles for two reinforced sections at different loading times.	110
Figure 8.2.2	Pore water pressure vs. rutting for two reinforced sections at different loading times.	111
Figure 8.2.3	Load cycles for 25, 20 or 12.5 mm rut vs. time from end of construction to start of loading for 5 reinforced sections.	112
Figure 8.2.4	Rutting vs. load cycles for GTX5 and first loading of GTX10 and GTX11	114
Figure 8.2.5	Pore water pressure vs. load cycles for section GTX5 and first loading of GTX10 and GTX11.	115
Figure 8.2.6	Rutting vs. load cycles for second loading of GTX10 and GTX11.	115
Figure 8.2.7	Pore water pressure vs. load cycles for second loading of GTX10 and GTX11.	116

CONVERSION FACTORS

The following conversion factors are required for interpretation of results contained in this report.

$$1 \text{ m} = 3.28 \text{ ft}$$

$$1 \text{ mm} = 0.0394 \text{ in}$$

$$1 \text{ kN} = 225 \text{ lb}$$

$$1 \text{ kN/m} = 68.6 \text{ lb/ft}$$

$$1 \text{ kPa} = 0.145 \text{ psi}$$

$$1 \text{ MN/m}^3 = 7.94 \times 10^{-6} \text{ lb/ft}^3$$

EXECUTIVE SUMMARY

Montana State University has previously completed experimental test section, numerical modeling and design model development projects for the Montana Department of Transportation. Test section work has led to a fundamental understanding of mechanisms by which geosynthetics provide reinforcement when placed in the aggregate layer of flexible pavements. Finite element numerical models have relied upon this knowledge as their basis while design models derived from these numerical models have been calibrated against results from test sections. The test sections used for the development of these models were limited by the number of subgrade types, geosynthetic types and loading type employed.

This project was initiated to provide additional test section data to better define the influence of traffic loading type and geosynthetic reinforcement type. The loading provided to the test sections forming the basis of the models described above consisted of a cyclic load applied to a stationary plate. In this project, four full-scale test sections were constructed and loaded with a heavy vehicle simulator (HVS) located at the US Army Corp of Engineers facility in Hanover, NH. The four test sections used three geosynthetics identical to those used in previous test sections and pavement layer materials and thickness similar to previous sections.

Additional test sections were constructed in the pavement test box used in previous studies to examine the influence of base aggregate type, base course thickness reduction levels and reinforcement type. A rounded pit run aggregate was used in test sections to evaluate the influence of geosynthetic-aggregate shear interaction parameters on reinforcement benefit. The 1993 AASHTO Design Guide was used to backcalculate the base course thickness reduction from previous test section results where a traffic benefit ratio (extension of life) was known. Sections were built to this base course thickness reduction to see if equivalent life to an unreinforced section was obtained. Finally, six different geosynthetic products were used in test sections to evaluate the influence of reinforcement type on pavement performance.

The four test sections loaded with the HVS tended to show pavement distress that was dominated by surface rutting due to the development of permanent strain in the asphalt concrete, base aggregate and subgrade layers. Several asphalt cracking areas were due to delamination between the binder and surface courses. The order of performance of the test sections generally followed that seen in previous studies. An evaluation of reinforcement benefit in terms of rutting

behavior was complicated by the observation of significant differences in rut level between the two ends of a given section for two of the four sections. Benefit values, defined in terms of a Traffic Benefit Ratio (TBR), were similar between these sections and previously constructed sections for the geotextile product used. For sections with geogrid products, TBR was generally lower in the sections loaded with the HVS. The sequence of loading of the sections may have influenced the development of pore water pressure under adjacent sections and had a bearing on the results obtained. Instrumentation contained in the sections tended to show reinforcement mechanisms similar to those observed previously in smaller scale sections.

Smaller scale test sections constructed to evaluate base reduction factors where the reduced thickness was based on estimates using the 1993 AASHTO flexible pavement design equations and TBR values from previous tests sections indicated that the use of this approach is largely conservative except for conditions where the aggregate is excessively thin (less than 150 mm in thickness). Values of base course reduction from the design model developed previously for the Montana DOT are conservative with respect to the results obtained from this portion of the study.

Unreinforced small scale test sections constructed with a rounded aggregate having a maximum particle size of 38 mm indicated superior performance as compared to unreinforced sections constructed with a crushed aggregate having a maximum particle size of 19 mm. The performance of reinforced sections using the rounded aggregate were generally inferior relative to those using a crushed aggregate. In addition, the order of performance of sections using two geosynthetic types was reversed when using the rounded aggregate. Results from direct shear tests yielding geosynthetic-aggregate interaction properties did not correspond to the results obtained.

The response of the test sections using different geosynthetic products was dominated by pore water pressure generation due to several factors. The subgrade used in these test sections readily develops positive pore water pressure during construction and pavement loading. The initial magnitude of pore water pressure prior to pavement loading has a significant impact on pavement response during loading as defined in terms of rutting. The magnitude of pore water pressure generation during pavement loading appears to be dependent on the initial value of pore water pressure at the start of loading and the set-up time of the subgrade. The initial pore water pressure in turn appears to be dependent on the amount of compaction energy imparted to the

constructed layers, the time for construction, and the time between end of construction and start of loading.

The response of the majority of the reinforced sections for this portion of the study was dominated by the pore water pressure issues described above. The last two sections constructed used a technique that involved two loading stages with a significant wait period in between. Results from the first loading stage when set-up time of the subgrade was relatively short showed a rapid development of rut depth and pore water pressure in the subgrade. Loading during the 2nd stage produced a much lower rate of rutting and pore pressure generation. Construction of test sections by this technique when using a subgrade which is highly susceptible to pore water pressure generation is believed to yield a method where comparison of test sections is possible.

1.0 INTRODUCTION

Montana State University (MSU) has previously completed experimental test section, numerical modeling and design model development projects for the Montana Department of Transportation (MDT). Test section work has led to a fundamental understanding of the mechanisms by which geosynthetics provide reinforcement when placed in the aggregate layer of flexible pavements (Perkins, 1999). This understanding has allowed finite element numerical models to be developed that are capable of describing these observed reinforcement mechanisms (Perkins 2001a). Response measures from the finite element model have been applied to traditional damage models for pavement rutting and calibrated against results from test sections to yield a predictive tool for pavement life for reinforced pavements (Perkins 2001b). The combined use of the numerical response and damage models in a parametric study has allowed for the development of generic design equations, expressed in the form of a spreadsheet program, to define reinforcement benefit as a function of critical pavement cross-section variables and pavement layer and geosynthetic properties.

The design model resulting from the work described above is based primarily on test sections employing a limited number of pavement geometries, subgrade conditions, geosynthetic types and traffic loadings. This project was initiated to provide additional test section data to better define the influence of traffic loading type and geosynthetic reinforcement type. The loading provided to the test sections described above consisted of a cyclic load of 40 kN applied to a stationary plate having a diameter of 305 mm. An objective of this project was to examine whether reinforcement benefit is influenced by how traffic loading is experimentally modeled and whether benefit values observed from previous test sections subject to idealized traffic loading differs significantly from that observed when more realistic moving wheel traffic loading is applied. To examine this issue, four full-scale pavement test sections having layer thicknesses and layer material properties similar to previous test sections were constructed in the Frost Effects Research Facility (FERF) at the US Army Corp of Engineers, Engineer Research and Development Center, Cold Regions Research and Engineering Laboratory (CRREL) located in Hanover, NH. The four test sections used three geosynthetics identical to those used in previous test sections. Test sections were loaded with a Heavy Vehicle Simulator (HVS) supplying a 40 kN load to a single set of rolling dual wheels.

Given the relatively high expense associated with constructing full-scale pavement test sections, additional test sections were constructed in the pavement test box at MSU used in a previous study (Perkins 1999) to examine the influence of base aggregate type, base course thickness reduction levels and reinforcement type. A rounded pit run aggregate was used in test sections to evaluate the influence of geosynthetic-aggregate shear interaction parameters on reinforcement benefit. The 1993 AASHTO Design Guide was used to backcalculate the base course thickness reduction from previous test section results where a traffic benefit ratio (extension of life) was known. Sections were built to this base course thickness reduction to see if equivalent life to an unreinforced section was obtained. Finally, six different geosynthetic products were used in test sections to evaluate the influence of reinforcement type on pavement performance.

2.0 SUMMARY OF PREVIOUS WORK

The State of Montana, like many rural, particularly western states, contains many miles of paved roadways with a relatively light traffic volume, but with a critical number of heavily loaded transport vehicles. The combination of a large number of lane miles, low traffic volumes and a small population base has traditionally meant that non-interstate roads are constructed with comparatively thin surface and base aggregate layers. Many regions of the state contain silty to clayey subsoils that become wet and weak during the spring as freezing fronts recede and precipitation is seasonably high. As a consequence of these conditions, maintenance and rehabilitation needs and costs are high.

The Montana Department of Transportation (MDT) identified geosynthetic reinforcement as a design and construction option suitable for new roads and existing roads requiring significant rehabilitation. This option has the potential to reduce construction costs by the use of less base aggregate, increase service life and reduce maintenance costs. The absence of non-proprietary design methods made it difficult to design a reinforced road taking into account the influence of various geosynthetics and their properties on improvement to pavement performance. In addition, design solutions did not exist that could account for the influence of pavement layer thickness and subgrade foundation properties.

To assist MDT in being able to take advantage of a promising technology, Montana State University has completed two principal research projects designed to provide a fundamental

understanding of the mechanical behavior of reinforced roads leading to tools by which reinforced roads could be designed. The first project involved the construction and monitoring of well-instrumented test sections. An earlier preliminary project (Perkins 1996) established the feasibility of instrumentation used in the subsequent test section project. The second involved the development of a finite element response model, damage models and a design model for reinforced roads. The purpose of this section is to summarize the significant findings from those studies as they relate to this project.

2.1 Test Section Construction

A pavement test facility was developed at MSU to provide idealized pavement loading on a full-scale (with respect to layer thickness) pavement cross-section (Perkins 1999). The facility consisted of a large concrete box having inside dimensions of 2 m by 2 m by 1.5 m in height. Subgrade, base aggregate and asphalt concrete layers were placed with hand-operated, power-assisted compactors. Traffic loading was modeled by applying a 40 kN cyclic load to a steel plate having a diameter of 305 mm. A waffled rubber pad was placed beneath the load plate and the pavement surface to provide a uniform pressure. Instrumentation was included to measure applied pavement load, pavement surface displacement, stress and strain within the base aggregate and subgrade layers and strain in the geosynthetic reinforcement layer. Specific details concerning the test facility are given in Section 3.2.

A total of 21 pavement-loading tests were reported. Table 2.1.1 summarizes pertinent details for each section. Geogrid A and B and Geotextile A are also used in new test sections described in this report. Manufacturer and product names and material properties are given in Table 4.4.1. The clay subgrade was a CH or A7-(6) material prepared at a water content to yield an average CBR value of 1.5. The silty-sand subgrade was a SM or A-4 having a CBR of approximately 15.

Table 2.1.1 Constructed test section variables from Perkins (1999).

Section ^a	Subgrade	Base Thickness ^b (mm)	Geosynthetic	Geosynthetic Placement Position
PCS1	Clay	300	Control	N/A
CS1	Clay	300	Geogrid A	Base/subgrade interface
CS2	Clay	300	Control	N/A
CS3	Clay	300	Geogrid A	100 mm above base/subgrade interface
CS5	Clay	300	Geogrid B	Base/subgrade interface
CS6	Clay	300	Geotextile A	Base/subgrade interface
CS7	Clay	300	Geogrid A	100 mm above base/subgrade interface
CS8	Clay	300	Control	N/A
CS9	Clay	375	Control	N/A
CS10	Clay	375	Geogrid A	Base/subgrade interface
CS11	Clay	300	Geogrid A	Base/subgrade interface
SSS1	Silty-sand	200	Control	N/A
SSS2	Silty-sand	200	Geogrid A	40 mm above base/subgrade interface
SSS3	Silty-sand	200	Geotextile A	40 mm above base/subgrade interface
SSS4	Silty-sand	200	Control	N/A
SSS5	Silty-sand	200	Geogrid A	Base/subgrade interface
SSS6	Silty-sand	200	Control	N/A
SSS7	Silty-sand	200	Control	N/A
SSS8	Silty-sand	200	Geotextile A	Base/subgrade interface
SSS9	Silty-sand	200	Geogrid A	Base/subgrade interface

^a Nominal AC thickness = 75 mm for all sections.

^b Nominal thickness.

N/A = Not applicable.

Significant reinforcement benefit was observed from the sections using the clay subgrade. Pavement performance benefit was observed primarily in terms of effects on the permanent deformation or rutting behavior of the pavement surface. Figure 2.1.1 illustrates results of surface rutting versus applied load cycle for test sections having the clay subgrade and a base thickness of 300 mm. A Traffic Benefit Ratio (*TBR*) was defined as the load cycles carried by a reinforced section divided by that of an equivalent unreinforced section at a particular rut depth. Figure 2.1.2 illustrates *TBR* values computed for the reinforced sections shown in Figure 2.1.1 for rut depths ranging from 1 to 25 mm. No benefit was observed for the sections containing the silty-sand subgrade with the higher CBR value. These results showed the importance of subgrade strength/stiffness, base layer thickness and geosynthetic properties on reinforcement benefit.

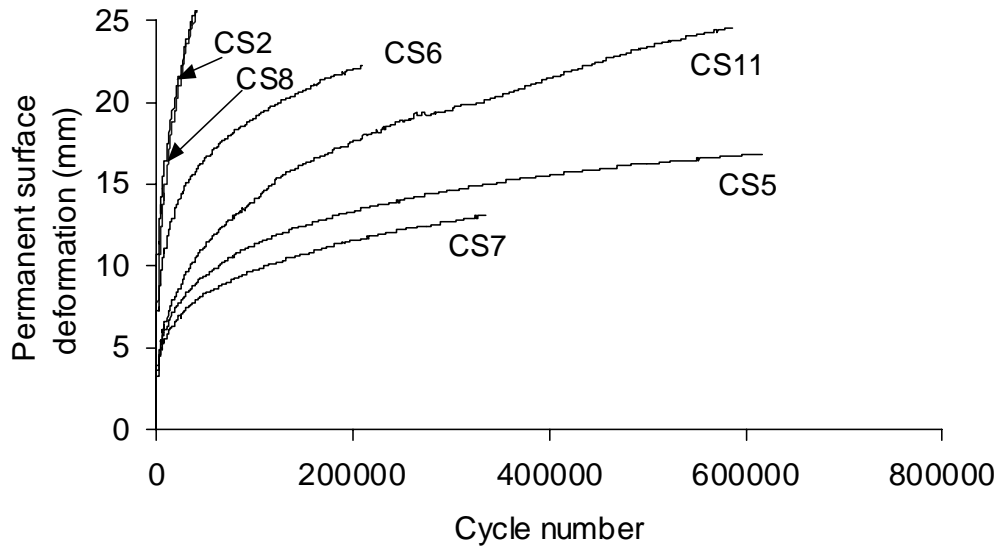


Figure 2.1.1 Permanent surface deformation versus load cycle (CS2, 5, 6, 7, 8, 11).

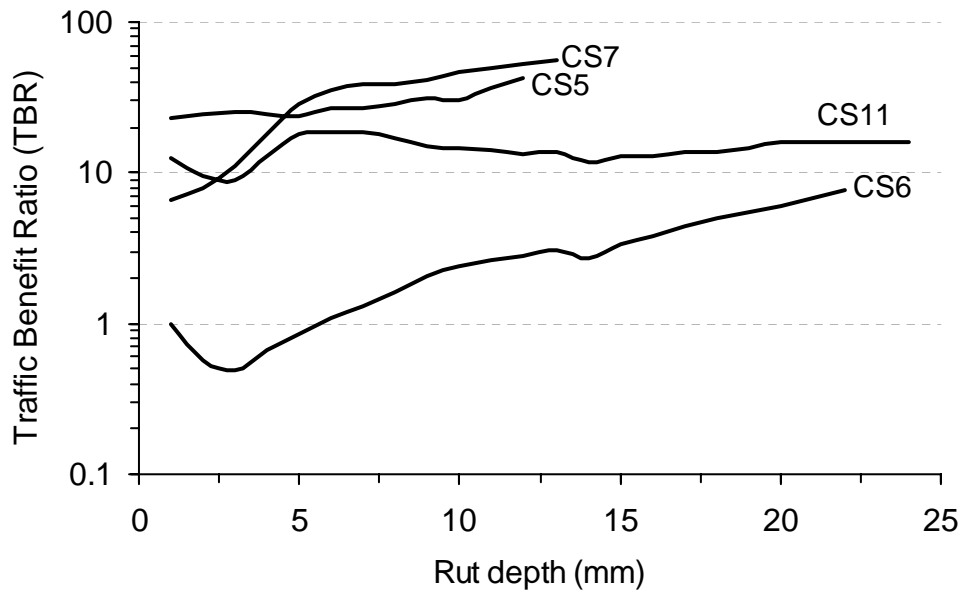


Figure 2.1.2 TBR for sections CS5, 6, 7 and 11 relative to section CS2.

Stress and strain instrumentation contained in the test sections provided a detailed understanding of the mechanisms by which reinforcement is provided. Measurement of radial strain at the bottom of the base indicated the tendency for significant extensional strains within a radius of 150 to 200 mm followed by compressional strain beyond this radius in unreinforced

sections (Figure 2.1.3). Sections containing reinforcement greatly reduced the lateral spreading occurring at this level in the base aggregate layer, as seen in Figure 2.1.3 for test section CS5.

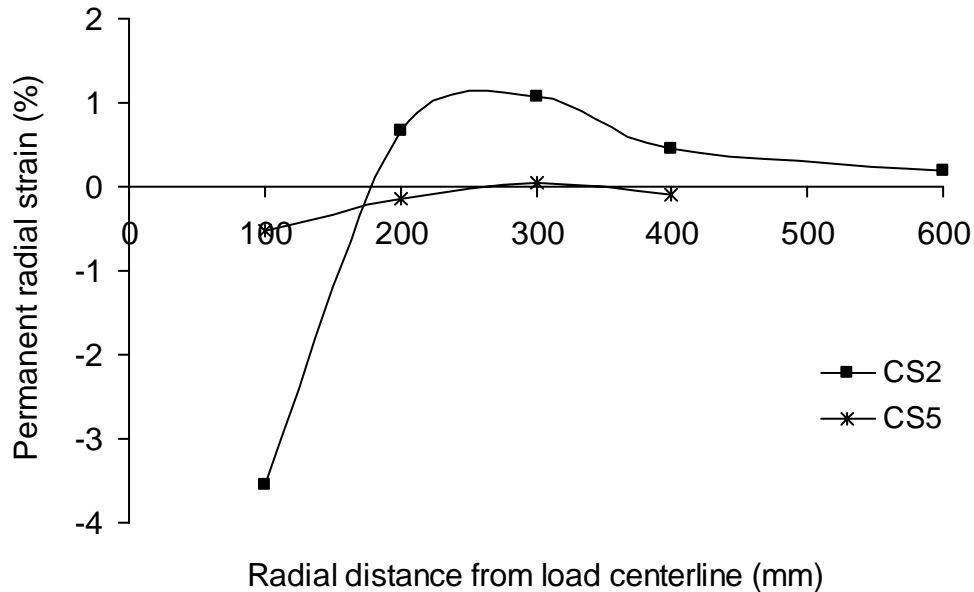


Figure 2.1.3 Permanent radial strain 50 mm above the bottom of the base versus radial distance at 40,000 load cycles (CS2, CS5).

It is expected that constraint of lateral movement of the aggregate layer provides an additional radial stress confinement, which in turn serves to increase the mean stress and reduce the deviatoric stress in the layer. Resilient modulus of aggregate materials is known to increase as mean stress increases and deviatoric stress decreases. Stress cell instrumentation was used to measure radial stress in the bottom of the aggregate, however the results could not conclusively illustrate this expectation. Other mechanical effects, however, that most likely stem from an increase in stiffness of a layer of aggregate adjacent to the geosynthetic were experimentally observed. These effects include a reduction of vertical stress on the subgrade beneath the load plate centerline and reduced lateral spreading in the top of the subgrade. The combined effect of these reinforcement mechanisms was a reduction of permanent vertical strain in the base and subgrade layers, leading to reduced surface deformation.

The test section data from this study provided a basis for subsequent numerical and design model development work.

2.2 Numerical and Design Model Development

A 3-D finite element model was developed to match the boundary and loading conditions contained in the MSU test facility described above. The model was originally developed to describe the cyclic, repeated load behavior observed in these sections. Relatively sophisticated plasticity based models were used for the base and subgrade layers (bounding surface plasticity), geosynthetic (isotropic hardening, anisotropic, with creep) and asphalt concrete (elastic-perfectly plastic) in order to be able to determine the accumulated strain and deformation with applied load cycle.

The model was able to describe the reinforcement mechanisms observed from test sections. Figure 2.2.1 shows the lateral strain at the bottom of the base for models of the clay subgrade sections with 300 mm of base aggregate. Three cases are shown corresponding to an unreinforced section, a section with geosynthetic reinforcement and a section with ideal reinforcement modeled by preventing lateral displacement of the nodes at the bottom of the base. Results of permanent lateral strain are shown after 10 cycles of load and are seen to qualitatively match those from Figure 2.1.3. Figure 2.2.2 shows the lateral permanent strain plotted along the load plate centerline where it is seen that the effect of lateral restraint of the bottom of the base is seen well up into the base and also effects the lateral spreading of the subgrade. The model was also able to show an increase in mean stress in the base, a reduction of vertical stress on the top of the subgrade and a reduction of vertical strain in the base and subgrade layers.

While the model was able to show an accumulation of strain with repeated load, excessive run times prevented the use of the model for prediction of multiple test sections subject to thousands of load cycles. In lieu of using the model for multiple load cycles, the model was then used to examine stress and strain response measures for a single cycle of load. Damage models were then developed to relate the response measures to long-term pavement performance. The first damage model used the vertical compressive strain in the top of the subgrade to predict the number of traffic loads to reach 12.5 mm of permanent surface deformation. The second damage model used the mean stress in a representative volume of the base aggregate layer to define average modulus of the base. This was then used within the context of the 1993 AASHTO guide to estimate the traffic load increase that could be applied to a reinforced pavement. The damage models were calibrated from test section results. Formulation of the model in this way allowed for the definition of *TBR* for any pavement configuration.

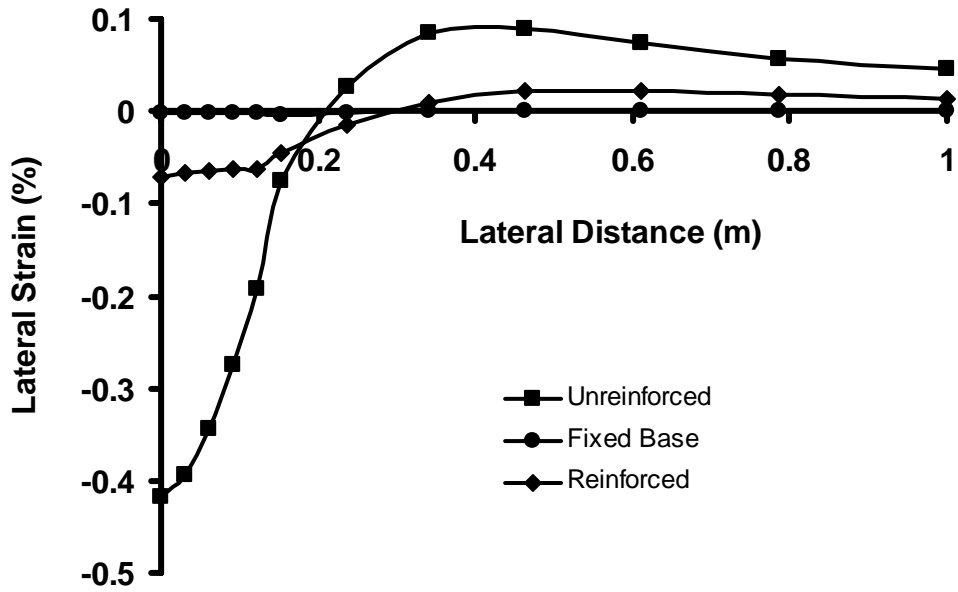


Figure 2.2.1 Lateral permanent strain in the bottom of the base versus lateral distance after 10 cycles of load.

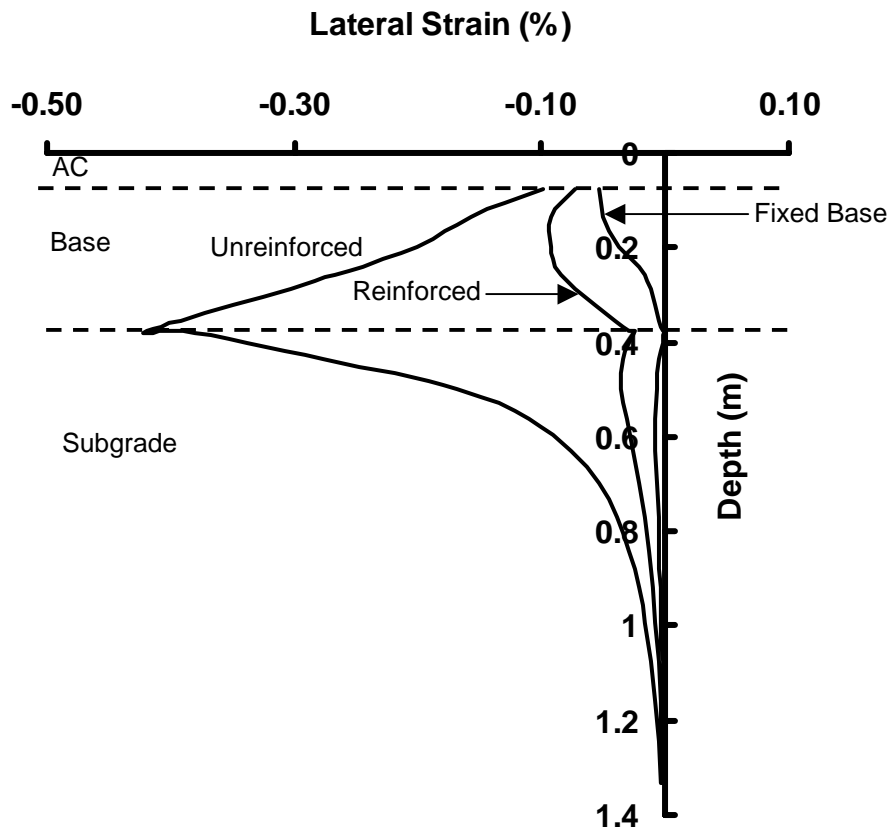


Figure 2.2.2 Lateral permanent strain along the load plate centerline versus depth after 10 cycles of load.

The model was then used in a parametric study involving the analysis of over 465 pavement cross sections where the thickness of the AC and base aggregate layers, subgrade strength and stiffness properties and geosynthetic properties were varied. Reinforcement benefit, defined in terms of *TBR* and Base Course reduction Ratio (*BCR*) were defined for each analysis. Regression equations were then developed to relate benefit values to the input parameters. The equations were programmed into a spreadsheet program to perform all necessary calculations to define benefit. Benefit values could then be used to alter the base thickness or service life of an unreinforced section designed by any acceptable technique. A design guide was included as an appendix in the report (Perkins 2001b). Life-cycle cost analyses were performed using DARWin to illustrate cost benefit of various alternatives (Perkins 2001c). Table 2.2.1 lists the input that is used in the model.

Table 2.2.1 Design model input parameters.

a_1	Asphalt concrete structural layer coefficient (unitless)
a_2	Base aggregate structural layer coefficient (unitless)
a_3	Subbase aggregate structural layer coefficient (unitless)
<i>CBR</i>	Subgrade California Bearing Ratio (%)
D_1	Asphalt concrete thickness (mm)
D_2	Base aggregate thickness (mm)
D_3	Subbase aggregate thickness (mm)
G_{MR}	Ratio of minimum to maximum 2 % secant modulus of the geosynthetic (unitless)
$G_{SM-2\%}$	Secant tensile modulus from ASTM 4595 measured at 2 % axial strain (kN/m)
m_2	Base layer drainage coefficient (unitless)
m_3	Subbase layer drainage coefficient (unitless)
R_{GI}	Reduction factor for interface shear (unitless)
R_{Gv}	Reduction for geosynthetic Poisson's ratio (unitless)
R_{GG}	Reduction for geosynthetic shear modulus (unitless)

3.0 PAVEMENT TEST FACILITIES

3.1 CRREL FERF/HVS

Four test sections were constructed in the Frost Effects Research Facility (FERF) located at the US Army Cold Regions Research and Engineering Laboratory (CRREL). Three test sections contained geosynthetics while one served as an unreinforced control section. The test sections were constructed using similar pavement thickness and material layer types as test sections previously constructed using the MSU test box and reported by Perkins (1999). The purpose of

these test sections was to compare reinforcement benefit values (namely *TBR*) between similar test sections using two types of loading. Test sections previously reported by Perkins (1999) were constructed in a large concrete box with traffic load modeled by applying a 40 kN cyclic load to a 305 mm diameter stationary plate resting on the AC surface. The CRREL test sections are larger test sections loaded by a moving wheel load using a Heavy Vehicle Simulator (HVS).

3.1.1 Facility Geometry and Loading

All test sections were constructed in an indoor, climate controlled facility (FERF). The FERF consists of 12 cells constructed of reinforced concrete, below-grade channels. The four test sections constructed for this project were constructed in two interconnected cells having a total length of 19.82 m, 6.36 m in width and 3.66 m in depth. The material layers comprising the test section (subgrade, geosynthetics, base aggregate, asphalt concrete) were uniformly placed across the entire area comprising the 4 test sections. The total area was divided into 4 equal areas of 9.91 m in length by 3.18 m in width. For the sections containing a geosynthetic, a geosynthetic was cut to the dimensions of 9.91 m by 3.18 m and placed directly on top of the subgrade prior to the placement of base aggregate. Figure 3.1.1 shows the dimensions and location of each test section.

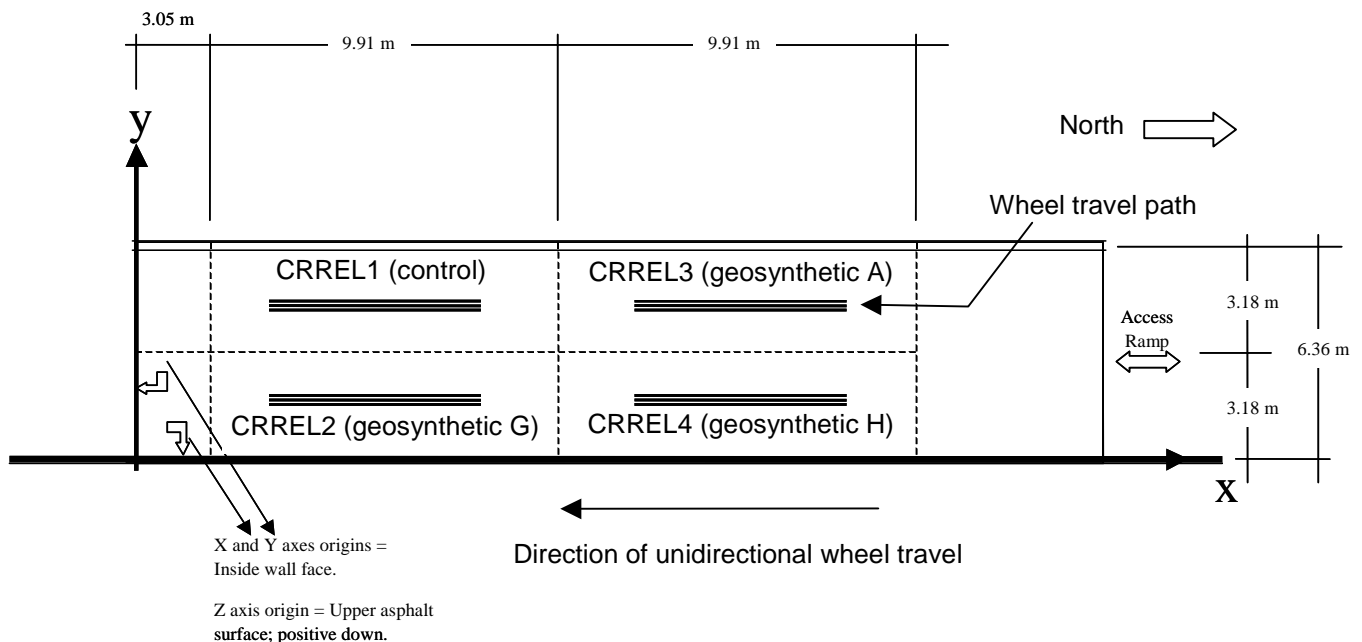


Figure 3.1.1 Dimensions and locations of test sections.

Traffic load was applied using a Mark IV Heavy Vehicle Simulator (HVS). A picture of the HVS and the dual wheel system used is shown in Figure 3.1.2. Wheel loading was applied unidirectionally from North to South and was applied individually within each test section. The travel length of the wheels once full pavement load is applied is 6.09 m. Additional travel length is used at the beginning and ends of the travel path for wheel touch-down/acceleration and lift-off/deceleration. The length of these zones is 0.91 m for both the acceleration and deceleration zones. The travel path of the wheel was centered within each of the 4 sectioned areas as shown in Figures 3.1.1 and Figure 3.1.3. The wheel load is applied unidirectional with the wheel raised completely off the pavement as it returns to its starting position. The wheel speed across the travel path is 13 km/hr with 700 passes/hr being applied for 22 hours a day, 7 days a week. The geometry of the dual wheels used is shown in Figure 3.1.4. The wheels were inflated to 690 kPa with a load of 40 kN applied.



Figure 3.1.2 Heavy Vehicle Simulator used for CRREL test sections.

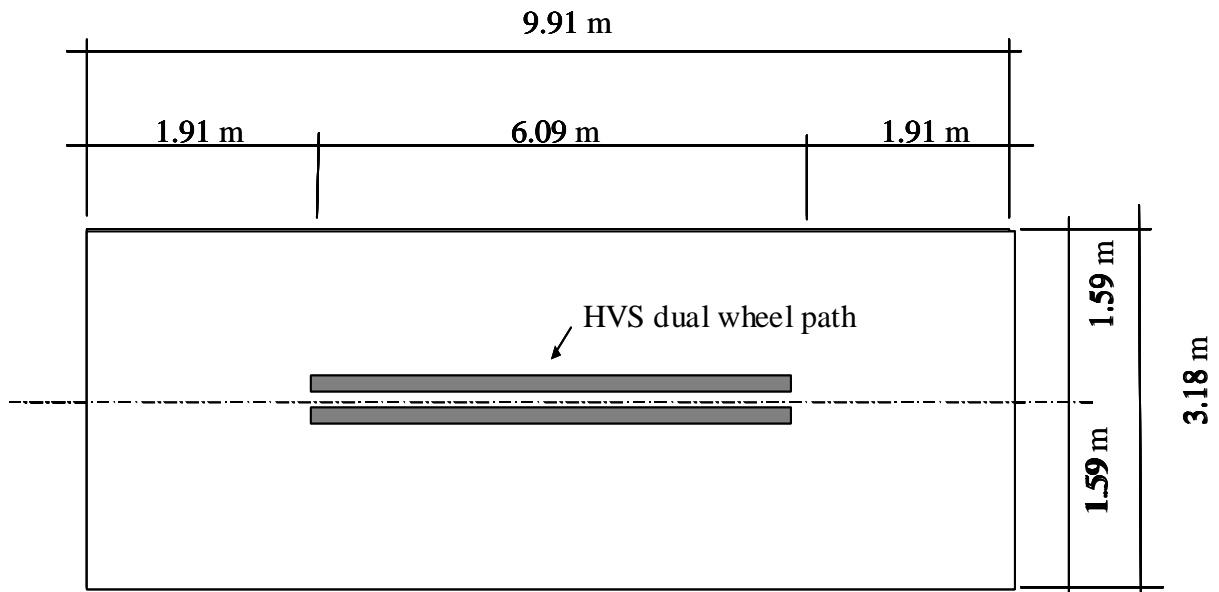


Figure 3.1.3 Location of wheel travel path within a test section.

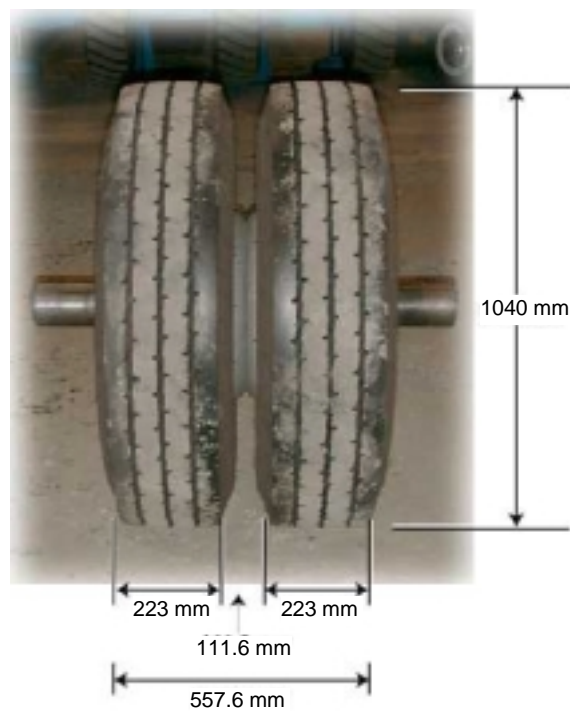


Figure 3.1.4 Dimensions of dual tires used on the HVS.

3.1.2 Construction Process

The overall cross-section of the 4 test sections is shown in Figure 3.1.5. The lower subgrade soil layer having an AASHTO classification of A-2-4 was left in place from a previous project and

served as the foundation soil for the construction of the remaining cross-section. The upper subgrade layer having an AASHTO classification of A-7-6 served as the subject subgrade for the test sections. The material was obtained from a borrow pit located in St Albans, Vermont. The soil was processed by drying and sieving over a large screen with 19 mm openings. A 150 mm layer of this soil was prepared at a high water content was first placed on top of the A-2-4 subgrade to serve as a moisture barrier between the two subgrade types. The remaining A-7-6 subgrade was processed in sufficient quantities to produce 150 mm thick layers for placement. Material was dumped on the prepared subgrade surface and spread with a bulldozer. A tractor equipped with a rototiller and a metered water spray bar applied and distributed water to the placed soil. Water content was adjusted to be within the target range prior to compaction. Compaction took place with a 9000 kg steel wheel roller (Figure 3.1.6). The A-7-6 subgrade was placed in seven layers. Nuclear density (verified by sand cone tests) and oven-dried moisture content readings were taken from the compacted lifts. Rod and level measurements were taken on the finished subgrade surface. Dynamic Cone Penetrometer (DCP) measurements were at selected locations on the subgrade.

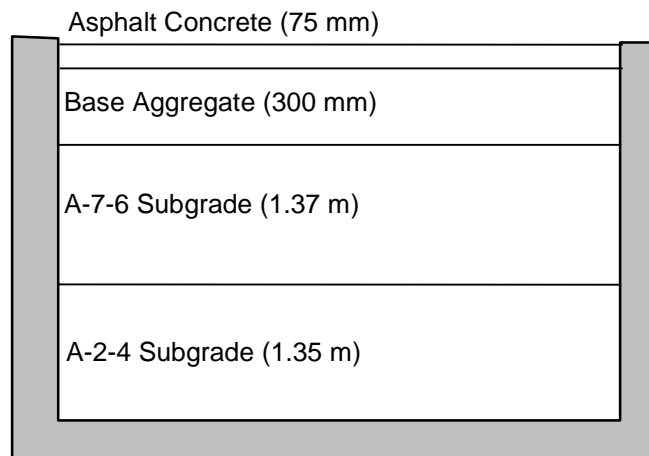


Figure 3.1.5 Cross-section dimensions of CRREL test sections.



Figure 3.1.6 CRREL subgrade compaction.

The geosynthetic reinforcement placed in sections 2-4 was laid directly on the finished subgrade. The reinforcement was stretched to lay flat on the subgrade with no wrinkles or folds. The aggregate was placed on the north end of the test section area and spread to the south using a bulldozer. The base course aggregate was placed in two 150 mm lifts and compacted with a steel wheel roller operated in the static mode. Nuclear density (verified by sand cone tests) and oven-dried moisture content readings were taken from the compacted lifts. Rod and level measurements were taken on the finished base aggregate surface.

The asphalt pavement was placed in two layers. A hot mix asphalt produced at a local plant located 7 miles from the FERF was used. The material was placed by a paving contractor with a paver and compacted with a Hyster C350C roller operated in the static mode. The first lift was a base course mix having a specification with an asphalt content between 4.8 and 6 percent and a nominal maximum aggregate size of 19 mm. The second layer was a surface layer having a specification with an asphalt content between 6.25 and 7 percent and a nominal maximum aggregate size of 9.5 mm. The asphalt binder was a NH DOT PG 64-22. Figure 3.1.7 shows the completed test sections. Properties of the compacted pavement layers are presented in Section 4.



Figure 3.1.7 CRREL paved test sections.

The timeline followed for the construction of the CRREL test sections was as follows:

October 10, 2000: Subgrade placement began.

November 6, 2000: Subgrade placement was completed.

November 15, 2000: Base aggregate placement was completed.

November 16, 2000: Asphalt concrete placement was completed.

April 1, 2001: Loading of Test Section 1 began.

April 13, 2001: Loading of Test Section 1 completed.

April 17, 2001: Loading of Test Section 3 began.

May 3, 2001: Loading of Test Section 3 completed.

May 22, 2001: Loading of Test Section 2 began.

June 15, 2001: Loading of Test Section 2 completed.

June 24, 2001: Loading of Test Section 4 began.

July 31, 2001: Loading of Test Section 4 completed.

3.1.3 Instrumentation

Instrumentation was placed within the test sections to measure stress, strain, temperature and moisture. Instrumentation was also used to measure the pavement deformation profile. Cross-

sectional profiles were taken at 20 locations along the wheel track at 0.30 m intervals. Each cross-section consisted of 256 depth measurements at 9 mm intervals.

Stress instrumentation consisted of two types of stress cells. Five Dynatest (Ventura, CA) stress cells were installed in each section in the upper subgrade to measure vertical stress. These cells have a diameter of 68 mm and a thickness of 13 mm. The cells utilize a thin, 0.5 mm thick membrane that covers a layer of fluid. Fluid pressure is measured by a fully-bridged strain gauge pressure transducer inside the cell. The cells are coated with epoxy and sand to ensure proper bonding to soil materials. A typical stress cell is shown in Figure 3.1.8. Performance and calibration of these cells has been discussed in Ullidtz et al. (1996), Askegaard et al. (1997) and Selig et al. (1997). Table 3.1.1 lists the locations of the stress cells in reference to the center of the wheel path. An additional three Geokon (Lebanon, NH) stress cells were placed in the base aggregate of Section 1 to measure stress in the vertical, transverse and longitudinal directions. Table 3.1.1 also lists locations for these gauges.



Figure 3.1.8 Soil stress cells (Dynatest).

Soil strain was measured with EMU strain coils (Janoo et al., 1999) shown in Figure 3.1.9 and having a diameter of 100 mm. EMU strain coils operate in pairs with one acting as the transmitter and one as the receiver. Alternating current is passed through the transmitting coil,

which generates an alternating magnetic field. This field induces an alternating current in the receiving coil with the magnitude of this current being governed by the distance between the coils. The coils were calibrated to provide a relationship between current and distance between coils. Measures of both dynamic and permanent strain were made with the coils. The 37 coils installed in each test section allowed for 35 different measurements of strain. Table 3.1.1 provides locations of the strain measurements.

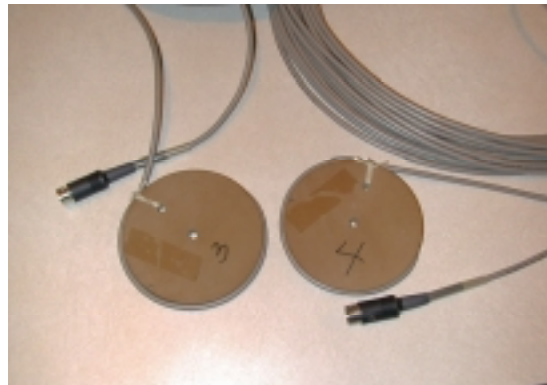


Figure 3.1.9 EMU strain coils.

Geosynthetic strain was measured by attaching foil strain gauges to the geogrid and geotextile sheets in the vicinity of the wheel travel path. Gauge types and mounting procedures followed those used in previous test sections constructed at MSU as described by Perkins (1999). Strain gauges were attached to 10 locations on each reinforcement sheet to measure strain in the longitudinal and transverse directions of the material.

Two sets of 8 thermocouples were installed at the boundary between Sections 1 and 2 and between Sections 3 and 4. The uppermost thermocouple was located in the base aggregate with the remainder installed in the subgrade to a maximum depth of 1.38 m below the pavement surface. Four moisture sensors were installed within the subgrade between Sections 1 and 2 and Sections 3 and 4. The sensors were installed at depths of 0.54 and 0.9 m below the pavement surface.

Table 3.1.1 Locations of stress and strain instrumentation.

Sensor	Response Measure	Layer	Y (m)	Z (m)
Dyna1	σ_z	S	0	0.46
Dyna2	σ_z	S	0	0.46
Dyna3	σ_z	S	0	0.61
Dyna4	σ_z	S	0.15	0.46
Dyna5	σ_z	S	0.35	0.46
GeoX	σ_x	B	0	0.146
GeoY	σ_y	B	0	0.180
GeoZ	σ_v	B	0	0.293
EMU1	ϵ_z	B	0	0.18
EMU2	ϵ_z	B	0	0.18
EMU3	ϵ_z	B	0	0.28
EMU4	ϵ_z	B	0	0.28
EMU5	ϵ_z	B/S	0	0.38
EMU6	ϵ_z	B/S	0	0.38
EMU7	ϵ_z	S	0	0.505
EMU8	ϵ_z	S	0	0.505
EMU9	ϵ_z	S	0	0.655
EMU10	ϵ_z	S	0	0.655
EMU11	ϵ_z	S	0	0.805
EMU12	ϵ_z	S	0	0.955
EMU13	ϵ_z	S	0	1.105
EMU14	ϵ_z	S	0	1.255
EMU15	ϵ_y	B	0.075	0.23
EMU16	ϵ_y	B	0.225	0.23
EMU17	ϵ_y	B	0.375	0.23
EMU18	ϵ_y	B	0.075	0.33
EMU19	ϵ_y	B	0.225	0.33
EMU20	ϵ_y	B	0.375	0.33
EMU21	ϵ_y	B	0.525	0.33
EMU22	ϵ_y	B	0.075	0.33
EMU23	ϵ_y	S	0.225	0.33
EMU24	ϵ_y	S	0.075	0.43
EMU25	ϵ_y	S	0.225	0.43
EMU26	ϵ_y	S	0.375	0.43
EMU27	ϵ_y	S	0.525	0.43
EMU28	ϵ_y	S	0.075	0.43
EMU29	ϵ_y	S	0.075	0.58
EMU30	ϵ_y	S	0.225	0.58
EMU31	ϵ_y	S	0.375	0.58
EMU32	ϵ_x	B	0	0.23
EMU33	ϵ_x	B	0	0.33
EMU34	ϵ_x	S	0	0.43
EMU35	ϵ_x	S	0	0.58

Data was acquired at the following pass levels: 0, 50, 100, 250, 500, 1000, 2500, 5000, 10000, 25000, 50000, 100000, 250000 or until failure occurred. Failure was defined as an average rut depth of 25 mm. Profile measurements and static readings of the EMU strain coils were made at each pass level. Static readings were used to determine permanent strain corresponding to that pass level. The HVS was then allowed to make 25 passes following the particular pass level where static measurements were obtained. For each of the 25 passes, the stress cells were monitored and recorded. The EMU strain coils acting as transmitters were activated one by one in order to obtain a dynamic strain response for all the coil pairs. Twenty five passes were required to cycle through all possible strain coil pairs. Data was stored in spreadsheet importable files for later use.

3.2 MSU/GTX Test Box

A test facility was previously designed and constructed for the purpose of conducting laboratory, large-scale experiments on reinforced and unreinforced pavement sections and has been described by Perkins (1999). The facility was designed to mimic pavement layer materials and geometry, and loading conditions encountered in the field as realistically as possible with an indoor, laboratory based facility using a stationary load. This type of facility was chosen for this phase of the work because of the control that could be exercised on the construction and control of pavement layer material properties, the relatively large number of test sections that could be constructed and the relatively low cost of operation for this facility. This facility was used for all sections having a label beginning with MSU. Subsequent test sections were constructed in a similar facility constructed at the laboratory of GeoTesting Express, Alpharetta, GA. The structure of the test box was altered, however the loading system, data acquisition and instrumentation was the same used in the MSU box. All test sections constructed in the GTX box have a label beginning with GTX.

Pavement layer materials are similar to those commonly used and encountered in the field. Asphalt concrete (AC) and base aggregate layer thickness were chosen to match sections commonly encountered on secondary and some primary roadways in Montana. A cyclic, non-moving load with a peak load of 40 kN was used to mimic dynamic wheel loads. An array of sensors to measure stress and strain in various pavement layers was used to characterize mechanical response with and without the presence of reinforcement. Descriptions of these

components of the facility are provided in the sections below, along with a description of test section construction techniques, quality control measures and test section configurations constructed.

3.2.1 Facility Geometry and Loading

A test box was constructed having inside dimensions of 2 m in width and length and 1.5 m in height. Walls consisted of 150 mm thick reinforced concrete. The front wall is removable in order to facilitate excavation of the test sections. Figure 3.2.1 shows a schematic of the pavement test facility.

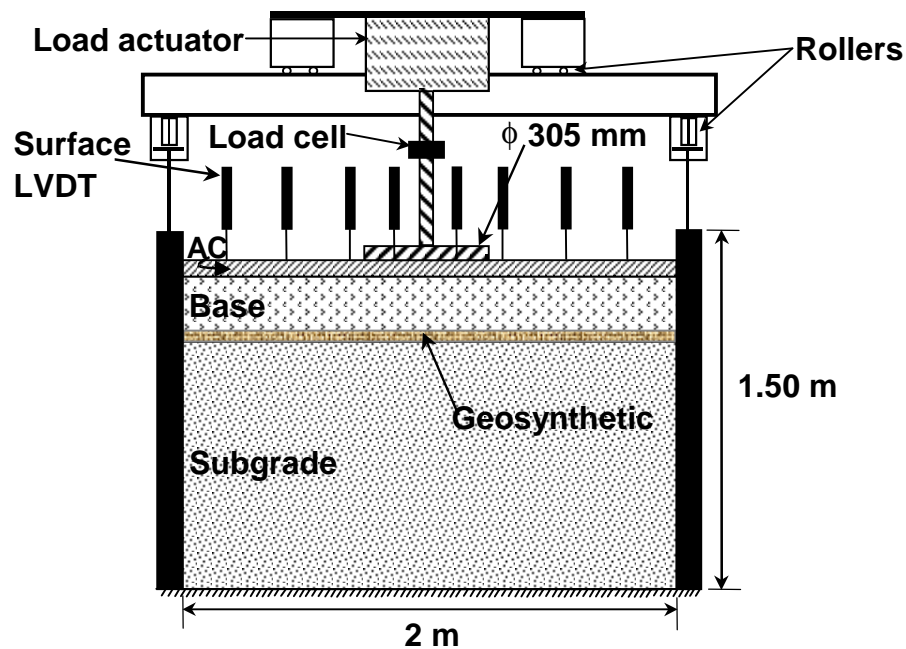


Figure 3.2.1 Schematic diagram of the MSU/GTX pavement test facility.

A load frame was constructed to support the load actuator. The frame consists of two I-beams that span the width of the box. A load actuator, consisting of a pneumatic cylinder with a 305 mm diameter bore and a stroke of 75 mm, was placed between the two I-beams of the frame. A 50 mm diameter steel rod 300 mm in length extends from the piston of the actuator. The rod is rounded at its tip and fits into a cup welded on top of the load plate that rests on the pavement surface.

The load plate consists of a 305 mm diameter steel plate with a thickness of 25 mm. A 4 mm thick, waffled butyl-rubber pad was placed beneath the load plate in order to provide a

uniform pressure and avoid stress concentrations along the plate's perimeter. Figure 3.2.2 shows an image of the load plate resting on the pavement surface.



Figure 3.2.2 Image of the pavement load plate and surface instrumentation.

A binary solenoid regulator attached to a computer controlled the load-time history applied to the plate. The software controlling the solenoid was the same software used to collect data from the instruments contained in the pavement sections. The software was set up to provide the load, or plate pressure pulse shown in Figure 3.2.3. This pulse has a linear load increase from zero to 40 kN over a 0.3 second rise time, followed by a 0.2 second period where the load is held constant, followed by a load decrease to zero over a 0.3 second period and finally followed by a 0.5 second period of zero load before the load cycle is repeated, resulting in a load pulse frequency of 0.67 Hz. For the GTX test sections, the zero load hold period was increased to 1.2 sec, resulting in a load pulse frequency of 0.5 Hz. The maximum applied load of 40 kN resulted in a pavement pressure of 550 kPa. This load represents one-half of an axle load from an equivalent single axle load (ESAL). The load frequency was selected to allow the data

acquisition system time to store data before the next load pulse was applied. The average peak plate pressure and standard deviation over the course of pavement loading are given in Section 5 for each test section reported. Also shown in Figure 3.2.3 is the corresponding output from the load cell for a typical load application. The hump seen on the descending branch of the curve is due to back venting of air pressure into the solenoid and was characteristic of all load pulses.

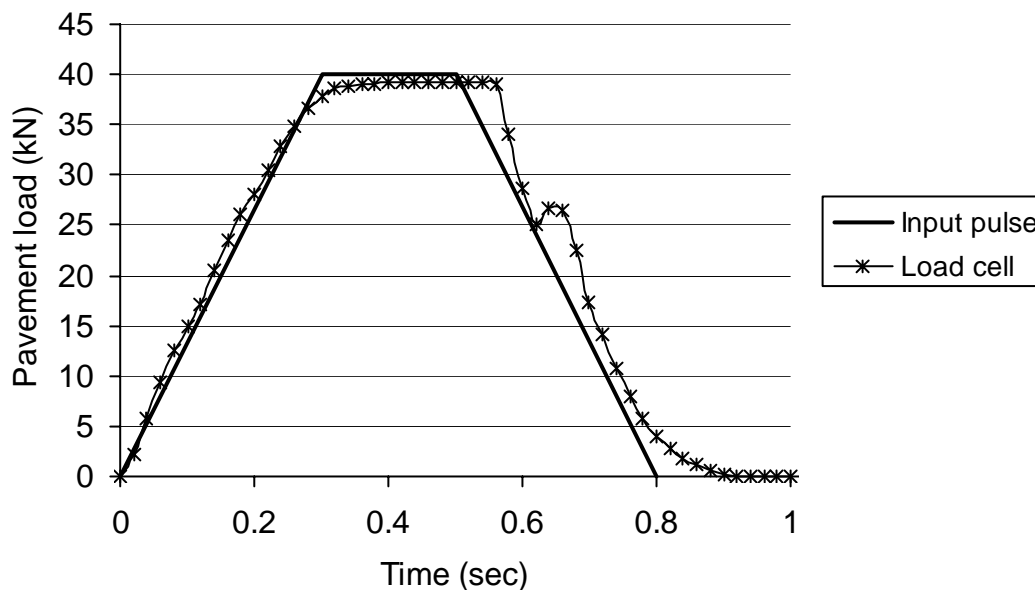


Figure 3.2.3 Input load pulse and corresponding load cell measurement.

3.2.2 Construction Process

Test sections built in the MSU/GTX boxes were built individually from the bottom up. All test sections consisted of a clay subgrade, a base aggregate layer and an asphalt concrete layer. Reinforcement was placed between the subgrade and the base aggregate layer for those sections that were reinforced.

The clay subgrade was constructed in approximately ten 75 mm lifts and compacted with a gasoline powered "jumping jack" trench compactor. The lift thickness of 75 mm was determined through trial and error so as to yield a uniform density in the layer without large void spaces. Thickness was measured with a standard auto-level and Philadelphia rod. The clay material was mixed to target moisture levels with a skid-steer loader. Numerous moisture content measurements were taken during mixing until the target value was achieved. Once a lift was compacted, approximately 5 samples were taken for oven drying to determine the in-place

moisture content. Five bulk density measurements were taken for each lift with a nuclear density gauge. The readings with this instrument were originally verified by sand-cone tests. Dry density was calculated from the oven dried moisture content and the measured bulk density. Moisture content and density measurements were also made during excavation of the test section to verify that only minor changes took place during loading for material outside the influence of the applied load. A DCP was used for the MSU test sections while a field vane shear test was performed on the GTX sections.

The base course material was also mixed with the skid steer loader to target moisture levels and placed in 100 mm lifts. Compaction was achieved with a vibratory plate compactor. Compacted moisture contents were determined by collecting samples and oven-drying this material. Densities were taken with a nuclear density meter and were originally verified with sand-cone tests. Moisture contents were also determined during excavation of the test sections. Layer surfaces were roughened with a rake prior to a subsequent lift placement in order to provide layer bonding.

The asphalt concrete layer was placed in two lifts corresponding to a target total thickness of 75 mm and compacted with a vibratory plate compactor. Hot-mix was typically placed at 138 degrees Celsius. The hot-mix was obtained from local batch plants. In-place density was measured with a nuclear gauge and later from drilled cores. Cores measuring 100 mm and 150 mm in diameter were taken from outside the loaded area after loading was completed. The asphalt layer was allowed to cure for a minimum of one day prior to loading.

3.2.3 Instrumentation

Instrumentation to measure applied load, stress, strain and pavement deformation has been used in the MSU and GTX test sections to quantify the mechanical response of the pavement materials to loading. Pore water pressure transducers were included in the GTX test sections. Instrumentation has been categorized into sensors measuring applied pavement load, asphalt surface deflection, stress and strain in the base course and subgrade, strain on the geosynthetic and pore pressure in the subgrade. Data acquisition software was configured to record information on the full time-history of response for prescribed load cycles and maximum and minimum sensor response for other load cycles.

A load cell was placed between the rod emerging from the pneumatic actuator and the load plate to measure applied pavement load. The load cell was manufactured by Sensotec (Columbus, OH) and has a range of 0-90 kN. Eight Linear Variable Differential Transducers (LVDT, RDP Electronics, Pottstown, PA) were used to monitor surface deformation of the asphalt concrete layer. Two different gauges were used with ranges of 25 mm and 50 mm. The LVDT's with the greatest range were placed closest to the center of the load plate where the largest surface deformations occurred. The other gauges were placed at increasing radii from the load centerline. The two LVDT's closest to the load plate centerline extended through the load plate and waffled rubber pad and rested on the pavement surface.

Foil strain gauges were mounted to geogrid and geotextile samples in order to quantify in-situ strain behavior during pavement loading. Strain gauge types and mounting procedures followed those used in previous test sections as described in Perkins (1999).

Soil stress cells (Dynatest, Inc., Ventura, CA) were placed in both the base course and the subgrade in order to quantify the dynamic stress behavior of the system. These cells are of the same make as the cells used in the CRREL test sections.

Soil strain was measured by alternating current (AC) LVDT's fitted with steel end plates measuring 50 mm × 15 mm × 5 mm in thickness. The LVDT's (model D5/400W) were obtained from RDP Electronics (Pottstown, PA). The gauges have a nominal gauge length of 70-80 mm, which corresponds to a 0.2-10 % strain range depending on the electronic amplification used for the sensor. A typical LVDT used in the test sections is shown in Figure 3.2.4.

Pore pressure transducers were supplied by Sensym. The tip of the transducer consists of a 6.5 cm in length by 0.6 cm in diameter 1 bar porous stone. The stone is connected to 3 mm diameter high pressure plastic tubing. The tubing is connected to a strain-gauged diaphragm pressure transducer located outside the test box. The stone and tubing leading up to the transducer are deaired and kept in deaired water until they are placed in the subgrade. Atmospheric air pressure is open to the opposite side of the transducer. The sensors have a range of 200 kPa.

The data acquisition system was configured to measure the peak and static responses of all sensors at a large number of load applications. The full time response of the sensors was recorded at a smaller number of preselected load application levels.



Figure 3.2.4 Soil strain cell.

4.0 PAVEMENT MATERIALS

The pavement materials used in the test sections consist of asphalt concrete, base aggregate, subgrade and geosynthetics. These materials differed between the CRREL, MSU and GTX test sections. For the MSU sections, different types of base aggregate were employed. The sections below provide general properties for each of the materials used. Properties pertaining to particular test sections are presented in Section 5.

4.1 Asphalt Concrete

Hot mix asphalt concrete from local batch plants was used for all test sections. The following tests were performed on materials from each test section:

1. In-place density from 100 and 150 mm cores
2. Marshall stability and flow
3. Asphalt content
4. Rice specific gravity
5. Grain size distribution
6. Asphalt penetration

7. Asphalt viscosity
8. Indirect tension (IDT) resilient modulus
9. Determination of asphalt core ultimate strength following IDT test

Results from these tests are reported in Section 5 for each individual test section.

4.2 Base Aggregate

Two types of aggregate were used in the MSU test sections. The first base course type (MSU1) is identical to that used in the test sections previously constructed in the MSU test box (Perkins, 1999). This material is a crushed-stone base course meeting the Montana Department of Transportation specifications for a “crushed base course Type “B”, grade 2” and meeting specifications for a “crushed top surfacing type “A”, grade 2”. The second gravel (MSU2) is a pit run material taken from a quarry immediately adjacent to the quarry where the crushed base course was obtained. The material was uncrushed and screened over a 50 mm sieve. Both quarries lie in a broad valley located adjacent to Belgrade, Montana, which is approximately 20 miles from the foothills of the mountains from which the valley’s alluvial soils were derived. Material in the quarries consists of rounded river cobbles, gravel and sand.

The GTX aggregate was obtained from a quarry in Lithonia, GA. The aggregate consists of blasted rock that was then crushed and recombined to produce the desired grain size curve. The parent rock is 97 % monzonite and 3 % granite. The CRREL aggregate was obtained from a quarry in West Lebanon, NH and consisted of crushed rock derived from blasted amphibolite bedrock. Results of various laboratory tests on these materials are given in Table 4.2.1. A grain size distribution for each material is given in Figure 4.2.1.

Resilient modulus tests were performed on each material per NCHRP 1-28a (NCHRP, 2000). The test protocol results in parameters k_1 , k_2 , k_3 for the stress dependent equation for resilient modulus given by Equation 4.2.1 where θ is the bulk stress, τ_{oct} is the octahedral shear stress and p_a is equal to atmospheric pressure . These parameters are summarized in Table 4.2.2.

$$M_R = p_a k_1 \left(\frac{\theta}{p_a} \right)^{k_2} \left(\frac{\tau_{oct}}{p_a} + 1 \right)^{k_3} \quad (4.2.1)$$

Table 4.2.1 Base aggregate material properties.

	Gravel Source			
	MSU1	MSU2	GTX	CRREL
Classification ¹	A-1-a GW	A-1-a GP-GM	A-1-a GW-GM	A-1-a SM
Maximum dry density (kN/m ³) ²	21.5	21.0	21.4	23.6
Optimum moisture content (%) ²	7.2	8.0	6.6	5.3
Specific gravity ³	2.63	2.63	2.64	2.94
Liquid limit (%) ⁴	NP ⁷	NP ⁷	NP ⁷	NP ⁷
Plastic limit (%) ⁴	NP ⁷	NP ⁷	NP ⁷	NP ⁷
LA Abrasion (%) ⁵	18	0	NA ⁸	NA ⁸
At least one fractured face (%) ⁶	73	32	100	100
At least two fractured faces (%) ⁶	70	19	100	100

¹Per AASHTO M145-87 and ASTM D2487

²Per ASTM D1557

³Per ASTM D854

⁴Per ASTM D4318

⁵Per AASHTO 96-87

⁶Per ASTM D5821

⁷NP = Non Plastic

⁸NA = Not Available

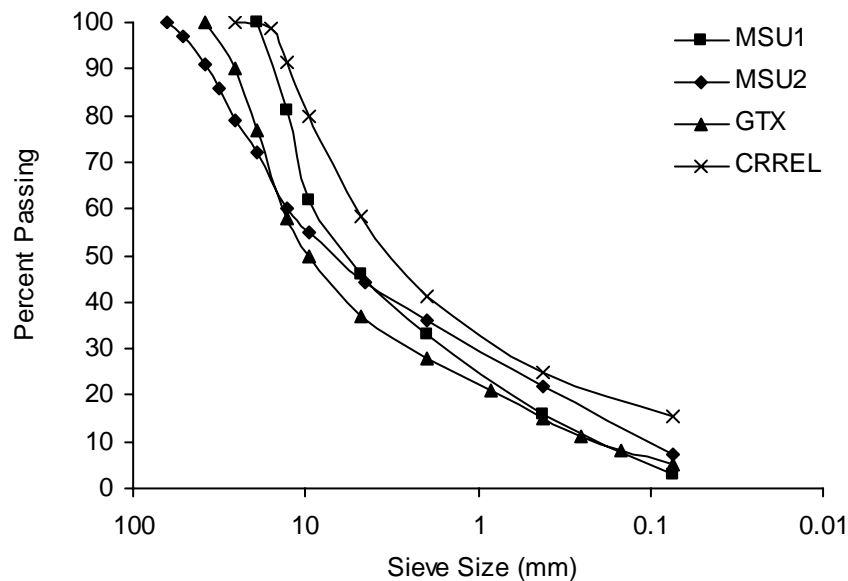


Figure 4.2.1 Grain size distribution of base aggregate materials.

Table 4.2.2 Base aggregate resilient modulus properties.

Material	k_1	k_2	k_3
MSU1	957	0.906	-0.614
MSU2	685	1.113	-0.580
GTX	741	1.091	-0.653
CRREL	662	1.010	-0.584

Conventional consolidated-drained triaxial compression tests have been performed on each of the aggregates. Three tests were performed on each material at confining stress levels of 25, 50 and 150 kPa. Figure 4.2.2 shows strength envelopes for each material on a p' - q stress diagram. A linear regression of the failure envelope resulted in the cohesion and friction angle values listed in Table 4.2.3. It should be noted that the strength envelopes have a curvature indicating an intercept that most likely goes through the origin, indicating that the cohesion values listed in Table 4.2.3 are artificially high.

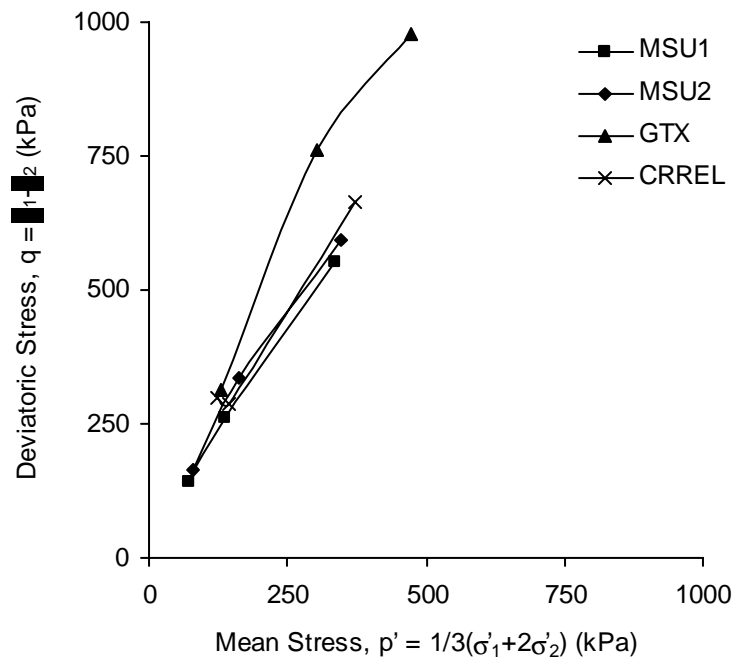


Figure 4.2.2 Base aggregate strength envelope from triaxial tests.

Table 4.2.3 Base aggregate strength (cohesion, friction angle) properties.

Material	c (kPa)	ϕ (degrees)
MSU1	19.6	38.0
MSU2	28.5	38.5
GTX	49.9	46.8
CRREL	42.0	38.2

4.3 Subgrade

Two types of subgrades were used in the test sections. The material used in the MSU test sections consisted of a highly plastic clay subgrade obtained from a uniform pit located south of Three Forks, MT. This subgrade was the same material used in previous test sections reported by Perkins (1999) and previously labeled as “CS”. The subgrade used in the CRREL test sections was a clay obtained from a pit located in St Albans, VT. This same material (after the processing described in Section 3.1.1) was shipped to GTX for use in those test sections. Table 4.3.1 lists properties of these two subgrade materials.

Table 4.3.1 Subgrade material properties.

	Subgrade Type	
	MSU	CRREL/GTX
Classification ¹	A-7 (6) CH	A-7 (6) CH
Maximum dry density (kN/m ³) ²	16.0	17.6
Optimum moisture content (%) ²	20.0	17.9
Specific gravity ³	2.70	2.76
Liquid limit (%) ⁴	73	56
Plastic limit (%) ⁴	28	20
Plasticity Index (%) ⁴	45	36
Passing # 200 Sieve (%) ⁵	100	86

¹Per AASHTO M145-87 and ASTM D2487

²Per ASTM D1557

³Per ASTM D854

⁴Per ASTM D4318

⁵Per ASTM D1140

CBR tests (ASTM D1188) were performed unsoaked on both materials prepared at a various moisture contents. The results of these tests are shown in Figure 4.3.1. Based on these results, the MSU subgrade was prepared in the test box at a target moisture content of 45 %, yielding an in-place CBR of 1.5 %. The CRREL/GTX subgrade was prepared at a target moisture content of 28 % in the CRREL test sections, yielding an in-place CBR of 1 %. GTX test sections used a target moisture content of 28 % for earlier sections and 27 % for later sections.

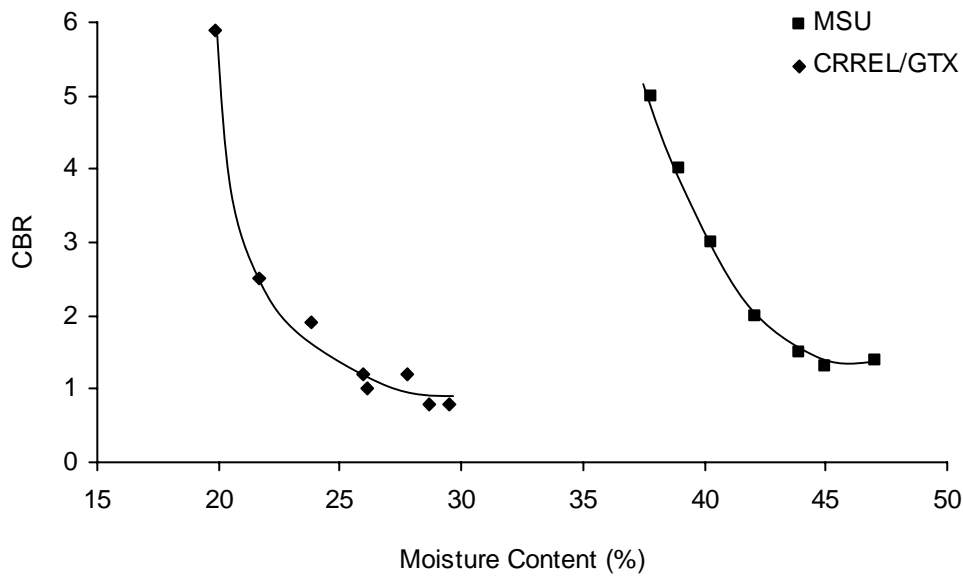


Figure 4.3.1 CBR versus compaction moisture content for the clay subgrade.

Figure 4.3.2 shows a dry-density versus moisture content diagram for the MSU and GTX subgrade showing the zero air voids curve for 100 % degree of saturations for each material and two data points corresponding to average dry density and water content for the constructed subgrade in the test sections for each facility. The results indicate that the GTX subgrade is essentially 100 % saturated while the MSU subgrade is approximately 94 % saturated.

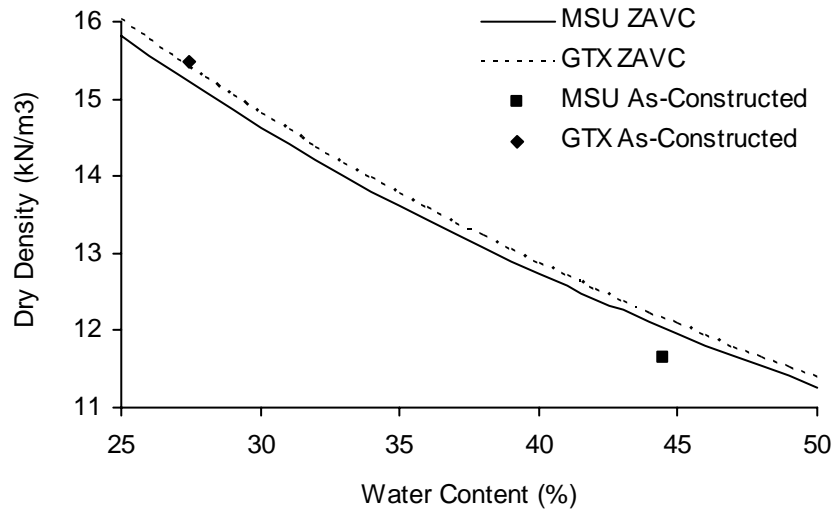


Figure 4.3.2 MSU and GTX subgrade compaction properties.

Consolidated-undrained conventional triaxial compression tests were performed on the two subgrades. Tests were performed at confinement stress levels of 10, 25 and 100 kPa. Specimens were backsaturated until a stable B-value was obtained. Samples of MSU subgrade were taken from Shelby tubes from previous test sections. Effective stress paths are shown on a $p'-q$ diagram in Figure 4.3.2.

Undisturbed samples were obtained from the CRREL test sections after loading and forensic evaluation work was completed. At the time of testing, approximately 15 months had elapsed since subgrade construction in the FERF was completed. Effective stress paths and a strength envelope are shown on a $p'-q$ diagram in Figure 4.3.3. The behavior seen is more indicative of a lightly overconsolidated material.

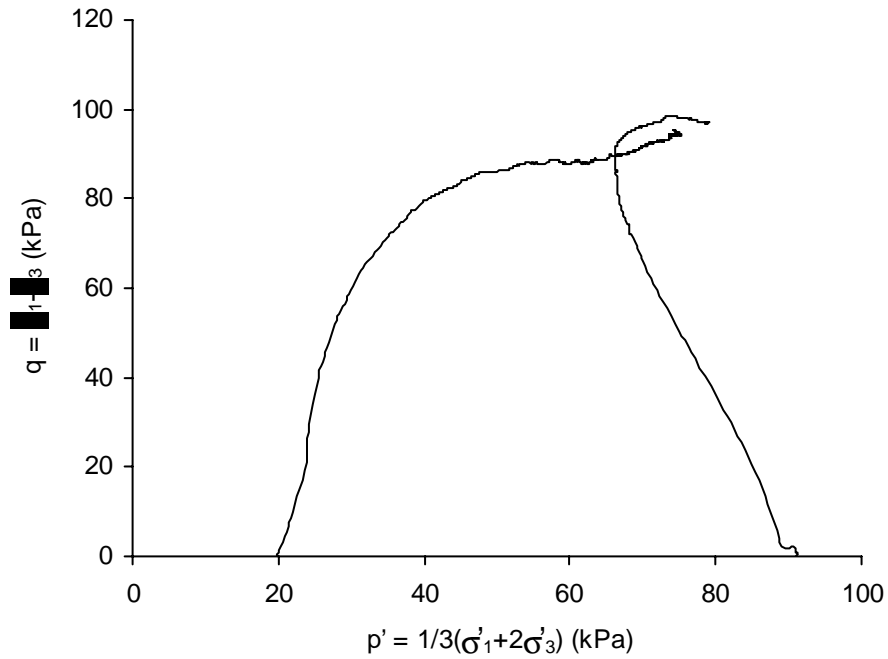


Figure 4.3.3 MSU subgrade strength envelopes from triaxial tests.

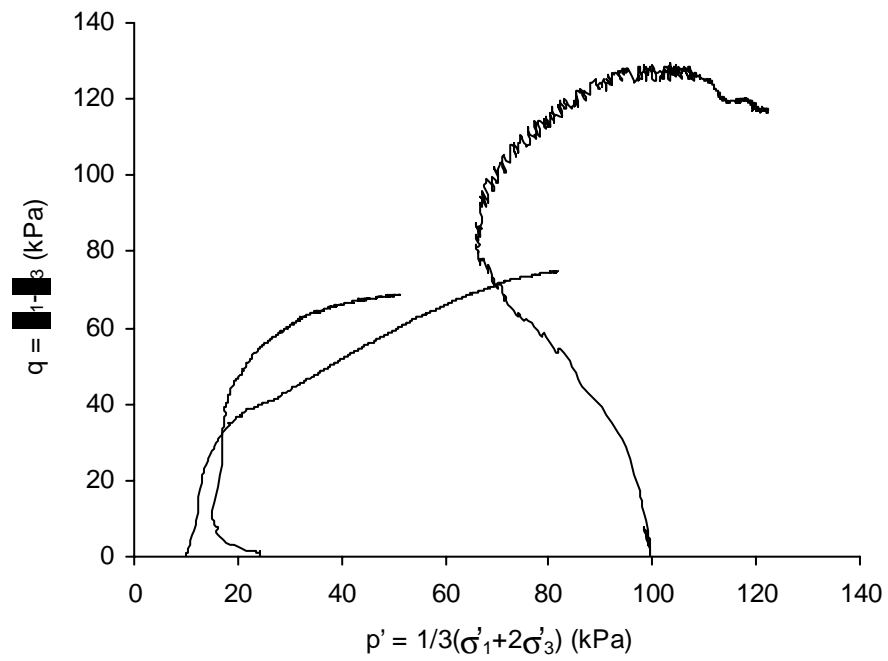


Figure 4.3.4 CRREL subgrade strength envelopes from triaxial tests.

A series of three triaxial compression tests were performed on undisturbed subgrade samples taken from test section GTX 10 during construction. Three tests were performed by applying a confinement of 10, 20 and 30 kPa and allowing the pore water pressure to stabilize. The specimens were not back pressure saturated. Shear loading was then applied with the drainage lines closed. These tests were performed at three different times during the progress of test section GTX 10. The first series of tests were performed at a time corresponding to immediately after the asphalt concrete was placed. The second series of tests were performed when the test section was first loaded by simulated traffic. The final series was performed when the test section was loaded by simulated traffic for the second time. These times corresponded to 4, 11 and 29 days following the end of subgrade construction. These tests were conducted as above and beyond the original scope of work by GTX to evaluate strength/stiffness aging effects seen in the GTX test sections. Table 4.3.2 lists the undrained cohesion of each test. The results indicate no significant trend of strength increase with aging time.

Table 4.3.2 Undrained cohesion of GTX subgrade.

Test Series	Undrained Cohesion (kPa)		
	Confinement (kPa)		
	10	20	30
1	24	47	35
2	35	33	33
3	32	31	35

Unconsolidated-undrained conventional triaxial compression tests were also performed on the subgrade materials. Approximately 15 tests were performed on undisturbed samples from test sections containing the MSU subgrade. Average results from these tests are given in Table 4.3.3. Three tests were performed on undisturbed specimens taken from the CRREL test sections with average results listed in Table 4.3.3. It should be noted that the undrained cohesion for the CRREL Shelby tubes samples is approximately twice that of the results obtained for the GTX subgrade given in Table 4.3.2, even though it is the same source material and was prepared to similar dry density and moisture content levels. The CRREL samples were tested after the last test section was loaded, meaning that the samples were aged considerably more than the GTX specimens, where aging of the CRREL samples took place with the material in-place in the

pavement section. The GTX samples were sampled immediately after subgrade construction and allowed to “age” within the confines of the Shelby tube.

Table 4.3.3 Undrained cohesion of subgrade materials.

Material	Undrained Cohesion, c_u (kPa)
MSU	33
CRREL	73

4.4 Geosynthetic

Table 4.4.1 lists the geosynthetics that have been used in test sections at CRREL and/or using the MSU and GTX test boxes.

Table 4.4.1 Geosynthetics used in test sections.

Generic Name	Manufacturer & Brand Name	Geosynthetic Type	Geosynthetic Polymer Type / Structure
Geosynthetic A	Amoco ProPex 2006	Geotextile	Polypropylene / Woven
Geosynthetic B	Colbond Enkagrid Max 20	Geogrid	Polypropylene / Welded grid
Geosynthetic C	Colbond Enkagrid Max X1	Geogrid	Polypropylene / Welded grid
Geosynthetic D	Synthetic Industries Geotex 3×3	Geotextile	Polypropylene / Woven
Geosynthetic E	Ten Cate Nicolon Geolon HP570	Geotextile	Polypropylene / Woven
Geosynthetic F	Tenax MS220b	Geogrid	Polypropylene / Extruded, multi-layer
Geosynthetic G	Tensar BX1100	Geogrid	Polypropylene / Biaxial, punched, drawn
Geosynthetic H	Tensar BX1200	Geogrid	Polypropylene / Biaxial, punched, drawn

4.4.1 Basic Properties

A range of index and mechanical tests were performed on the geosynthetics. Table 4.4.2 lists the tests performed and the results obtained on the materials.

Table 4.4.2 Geosynthetic properties.

Property	Geosynthetic ¹							
	A	B	C	D	E	F	G	H
Mass/Unit Area ² (g/m ²)		186	165	305	490	220	202	316
Apparent Opening Size ³ (mm)	0.425	NA	NA	0.600	0.600	NA	NA	NA
Percent Open Area ⁴ (%)	0.87/ 0.80	76	79	0.82/ 1.27	0.91/ 2.83	79	79	79
Aperture Size ⁵ (mm)	NA	44/44	59/44	NA	NA	42/50	25/36	25/36
Index Puncture ⁶ (kN)	0.53	NA	NA	0.80	0.87	NA	NA	NA
Tensile Modulus at 2 % Strain ⁷ (kN/m)	213/ 680	300/ 500	205/ 330	570/ 435	700/ 965	220/ 328	248/ 405	321/ 525
Tensile Modulus at 5 % Strain ⁷ (kN/m)	200/ 440	240/ 400	170/ 270	560/ 440	700/ 700	180/ 269	180/ 315	250/ 460
Ultimate Tensile Strength ⁷ (kN/m)	31/31	20/32	14/21	52/52	70/70	14/21	13/21	21/31
Elongation (at ultimate) ⁷ (%)	15/8	10/12	10/12	7/9	10/10	17/13	18/10	26/10
Initial Junction Stiffness ⁸ (kN/m)	NA	300	210	NA	NA	270	345	550
Ultimate Junction Strength ⁸ (kN/m)	NA	12.2/ 9.2	NP	NA	NA	12.2/ 19.2	13.8	21.5
Aperture Stability Modulus ⁹ (kN-m)	NA	202	204	NA	NA	141	135	417
Flexural Rigidity ¹⁰ (mg-cm)	11,858	Off-Scale	Off-Scale	43,114	119,803	Off-Scale	Off-Scale	Off-Scale
Permittivity ¹¹ (sec ⁻¹)	0.05	NA	NA	0.24	0.40	NA	NA	NA

NA=Not Applicable

NP=Not Provided

¹Property values listed as ## are for machine/cross machine directions

²ASTM D 5261

³ASTM D 4751

⁴COE CW-02215: values listed as ## correspond to material held perpendicular to viewing direction/material held at 45° to viewing direction

⁵Direct Measurement

⁶ASTM D 4833

⁷ASTM D 4595 or ASTM D 6637

⁸GRI GG2

⁹Torsional Rigidity Method

¹⁰ASTM D1388

¹¹ASTM D4491

4.4.2 Direct Shear Tests

A direct shear box manufactured by Brainard-Kilman was used to conduct direct shear tests between geosynthetics and base aggregates used in this study. The device consists of a 300 mm by 300 mm upper box and a 300 mm by 400 mm lower box. The height of each of the box halves is 100 mm. The upper box remains stationary relative to the moveable lower box and the geosynthetic is fixed to the upper box. Normal stress is provided by dead weights for low loads and by an air bladder for higher loads. The configuration of the box is as shown in Figure 4.4.1 with a photo showing the two halves of the box in Figure 4.4.2.

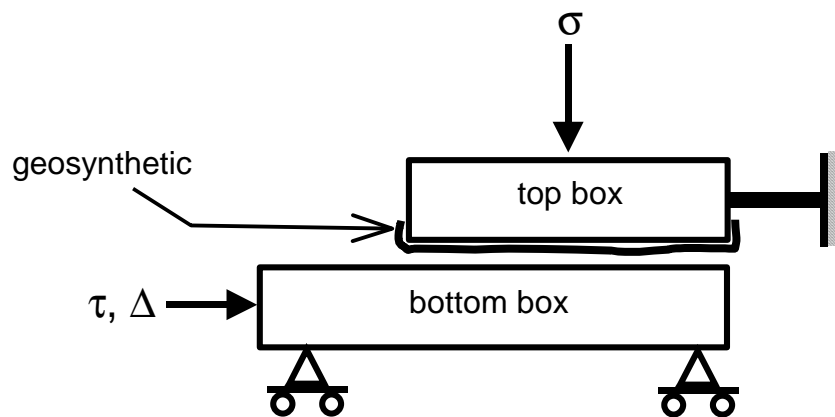


Figure 4.4.1 Schematic of direct shear box.



Figure 4.4.2 Photograph of direct shear box.

Table 4.4.1 lists the combinations of geosynthetics and aggregates that have been used in the tests. For each combination of materials, three repeat tests were conducted each at normal stress confinement levels of 50, 100 and 250 kPa. For each test, a curve of applied shear stress

versus shear displacement was plotted. All 9 curves for the combination of CRREL aggregate and geosynthetic A are shown in Figure 4.4.3. From each curve, the shear stress at a shear displacement of 2 mm was tabulated. The interface shear modulus, G_i , was calculated from Equation 4.4.1 and has units of kPa/mm. Values of shear modulus were then plotted separately against normal stress confinement. Figure 4.4.4 shows a diagram for shear modulus and a best fit line having the form of Equation 4.4.2, where C_1 and C_2 are curve fitting parameters. Values of C_1 and C_2 are then given in Table 4.4.4 for all material combinations. An Efficiency of interaction coefficient was then developed. This factor represents a constant multiplication factor applied to modulus from a particular geosynthetic-aggregate combination at a particular normal stress level to obtain the corresponding modulus value from aggregate to aggregate results. Efficiency coefficients are given in Table 4.4.5. Efficiency coefficients represent the increase or decrease in modulus as compared to that for an aggregate having no geosynthetic.

$$G_i = \frac{\text{Shear Stress at 2mm Shear Displacement}}{2 \text{ mm}} \quad (4.4.1)$$

$$G_i = \frac{\sigma_n}{C_1 + C_2 \sigma_n} \quad (4.4.2)$$

Table 4.4.3 Geosynthetic/aggregate combinations for direct shear tests.

Geosynthetic	Aggregate
None	MSU1
A	MSU1
G	MSU1
H	MSU1
None	MSU2
A	MSU2
G	MSU2
None	GTX
B	GTX
D	GTX
E	GTX
F	GTX
G	GTX
None	CRREL
A	CRREL
G	CRREL
H	CRREL

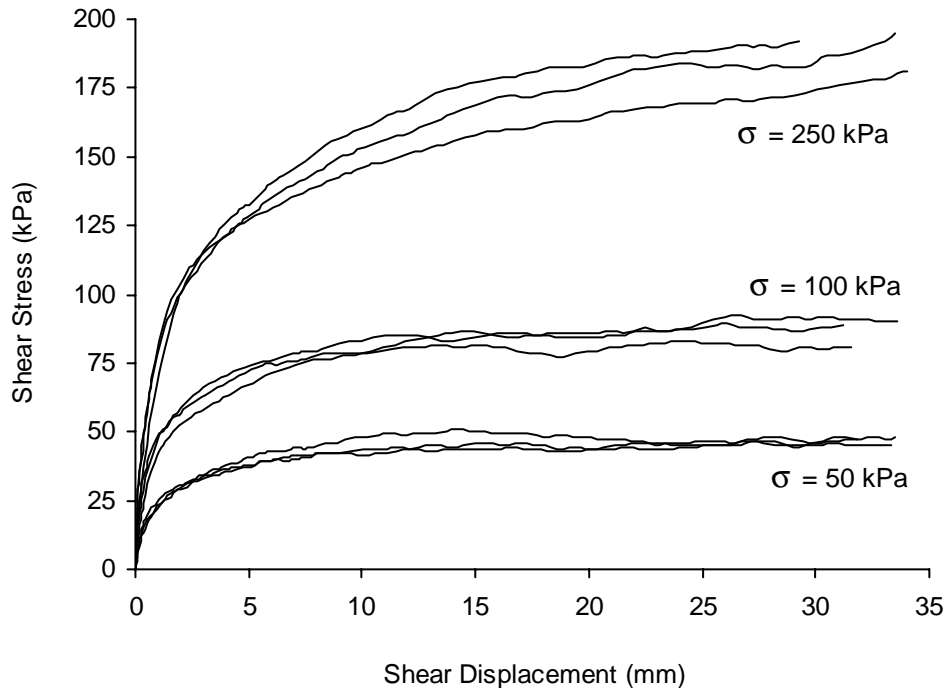


Figure 4.4.3 Shear stress vs. shear displacement from direct shear tests for CRREL aggregate – geosynthetic A.

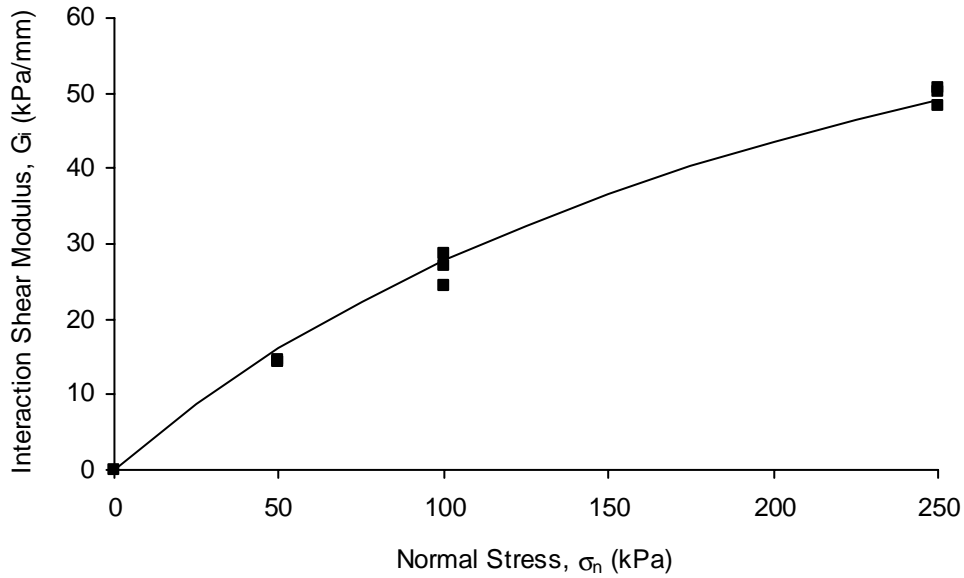


Figure 4.4.4 Interface shear modulus vs. normal stress for CRREL aggregate – geosynthetic A.

Table 4.4.4 Curve fit parameters, for Equations 4.4.2 and 4.4.3 for all geosynthetic/aggregate combinations.

Geosynthetic	Aggregate	C_1	C_2
None	MSU1	1.5	0.005
A	MSU1	2.5	0.010
G	MSU1	1.7	0.006
H	MSU1	1.7	0.007
None	MSU2	1.3	0.008
A	MSU2	1.7	0.009
G	MSU2	1.4	0.008
None	GTX	0.9	0.007
B	GTX	1.8	0.008
D	GTX	1.7	0.009
E	GTX	2.5	0.01
F	GTX	1.7	0.008
G	GTX	1.1	0.008
None	CRREL	1.8	0.0075
A	CRREL	2.6	0.01
G	CRREL	1.6	0.01
H	CRREL	1.75	0.01

Table 4.4.5 Efficiency coefficients from direct shear tests.

Geosynthetic	Aggregate	Efficiency Coefficient
None	MSU1	1
A	MSU1	0.563
G	MSU1	0.866
H	MSU1	0.819
None	MSU2	1
A	MSU2	0.819
G	MSU2	0.961
None	GTX	1
B	GTX	0.650
D	GTX	0.639
E	GTX	0.487
F	GTX	0.672
G	GTX	0.847
None	CRREL	1
A	CRREL	0.713
G	CRREL	0.944
H	CRREL	0.900

The results listed in Table 4.4.5 can be used when evaluating differences in performance of various sections. The results using the MSU1 aggregate correspond to performance from test sections described by Perkins (1999) using geosynthetics A, G and H. The results indicate little differences in efficiency between geosynthetics G and H (which is also confirmed using the CRREL aggregate), which should be expected since the two materials have a nearly identical structure and aperture size. The differences in efficiency between geosynthetics A and G partly explains the differences in test section performance. The design model developed by Perkins (2001) incorporated a reduction factor for interface shear. Values for geosynthetics G and H were assumed to be maximum values of 1. Comparison of predictions from the model to test section results indicated a value of 0.765 for geosynthetic A. From the results given in Table 4.4.5, this reduction factor can be calculated as the ratio of the efficiency for geosynthetic A to the average of efficiency for geosynthetics G and H ($0.563/((0.866+0.819)/2)=0.668$). These results indicate that the evaluation of interface shear modulus from direct shear tests can provide a reasonable approximation of reduction factors for interface shear for use in the design model described in Perkins (2001).

5.0 PAVEMENT TEST SECTIONS AND LAYER PROPERTIES

5.1 Test Sections Constructed

5.1.1 CRREL FERF/HVS

Four test sections were constructed at CRREL. Table 5.1.1 lists the materials used in these test sections and nominal thickness of the pavement layers. The geosynthetics were all placed between the base aggregate and the subgrade.

Table 5.1.1 CRREL test sections constructed.

Section	Layer Thickness (mm)		Layer Types			
	AC	Base	AC	Base	Subgrade	Geosynthetic
CRREL1	75	300	CRREL	CRREL	CRREL/GTX	None
CRREL2	75	300	CRREL	CRREL	CRREL/GTX	G
CRREL3	75	300	CRREL	CRREL	CRREL/GTX	A
CRREL4	75	300	CRREL	CRREL	CRREL/GTX	H

5.1.2 MSU/GTX Test Box

Thirteen sections were constructed in the MSU box and 11 in the GTX box. Table 5.1.2 lists the materials used in these test sections and nominal thickness of the pavement layers. The geosynthetics were all placed between the base aggregate and the subgrade. Specific geosynthetic products are not listed for the GTX sections to avoid unwarranted and arbitrary comparison of products at this time. Section 8 of the report presents the results from the GTX sections that has led to this form of presentation.

Table 5.1.2 MSU/GTX test sections constructed.

Section	Layer Thickness (mm)		Layer Types			
	AC	Base	AC	Base	Subgrade	Geosynthetic
MSU 1	75	300	MSU	MSU1	MSU	None
MSU 2	75	300	MSU	MSU1	MSU	None
MSU T1	75	175	MSU	MSU1	MSU	G
MSU T2	75	140	MSU	MSU1	MSU	H
MSU T3	75	140	MSU	MSU1	MSU	H
MSU T4	75	175	MSU	MSU1	MSU	G
MSU T5	75	200	MSU	MSU1	MSU	A
MSU T6	75	175	MSU	MSU1	MSU	G
MSU T7	75	200	MSU	MSU1	MSU	A
MSU R1	75	300	MSU	MSU2	MSU	None
MSU R2	75	300	MSU	MSU2	MSU	A
MSU R3	75	300	MSU	MSU2	MSU	None
MSU R4	75	300	MSU	MSU2	MSU	G
MSU R5	75	300	MSU	MSU2	MSU	A
GTX1	75	300	GTX	GTX	CRREL/GTX	None
GTX2	75	300	GTX	GTX	CRREL/GTX	None
GTX3	75	300	GTX	GTX	CRREL/GTX	Reinforced
GTX4	75	300	GTX	GTX	CRREL/GTX	None
GTX5	75	300	GTX	GTX	CRREL/GTX	None
GTX6	75	300	GTX	GTX	CRREL/GTX	Reinforced
GTX7	75	300	GTX	GTX	CRREL/GTX	Reinforced
GTX8	75	300	GTX	GTX	CRREL/GTX	Reinforced
GTX9	75	300	GTX	GTX	CRREL/GTX	Reinforced
GTX10	75	300	GTX	GTX	CRREL/GTX	Reinforced
GTX11	75	300	GTX	GTX	CRREL/GTX	Reinforced

5.2 Layer Properties and Quality Control Measures

5.2.1 CRREL FERF/HVS

Table 5.2.1 presents thickness, density and air voids data for the asphalt concrete in the CRREL test sections. Average values of thickness were determined from 8 rod and level measurements within each test section. The coefficient of variation of each parameter is given. Average density and air voids values were determined from 8 cores taken from each section outside the wheel path after loading was completed. The data indicates that the asphalt concrete in the test sections (3 and 4) towards the North end of the test cell were approximately 7 mm thicker. The asphalt concrete in these sections also had a higher density and lower air voids.

Table 5.2.1 As-constructed asphalt concrete properties for CRREL sections.

Section	Thickness (mm)	Density (kN/m ³)	Air Voids (%)	Coefficient of Variation (%)		
				Thickness	Density	Air Voids
CRREL1	78.6	20.9	18.9	9.9	4.4	19.2
CRREL2	77.5	21.0	18.4	8.5	3.8	16.7
CRREL3	85.0	22.3	13.3	5.3	1.7	11.1
CRREL4	86.1	22.2	13.2	4.9	2.9	19.2

Table 5.2.2 presents results of indirect tension resilient modulus tests performed on cores from the CRREL test sections. One test was performed on a core from each of the four sections. For each test, resilient modulus was determined for three loading frequencies (1, 0.5 and 0.33 Hz), two orientations 90 degrees apart and at three temperatures (21.1, 25.0 and 29.4 °C) yielding 18 values of resilient modulus for each specimen. The 6 tests at each temperature were averaged. A linear regression equation was then fit to the resulting three values of resilient modulus versus testing temperature. The average air temperature above the test section during the time of loading was then used to determine the resilient modulus for that section and correspond to the numbers reported in Table 5.2.2.

Table 5.2.2 Temperature during HVS loading and resilient modulus values of asphalt concrete for CRREL sections.

Section	Air Temperature During HVS Loading (°C)	Resilient Modulus (MPa)
CRREL1	20.0	1436
CRREL2	20.5	1577
CRREL3	19.0	1535
CRREL4	20.0	1068

In addition to the properties listed in Table 5.2.1, the properties given below were determined for bulk material taken from the test sections. Figure 5.2.1 shows a grain size distribution for the aggregate contained in the CRREL asphalt concrete.

Marshall Stability: 3853 lb
 Marshall Flow: 12
 Asphalt Content: 5 %
 Rice Specific Gravity: 2.62

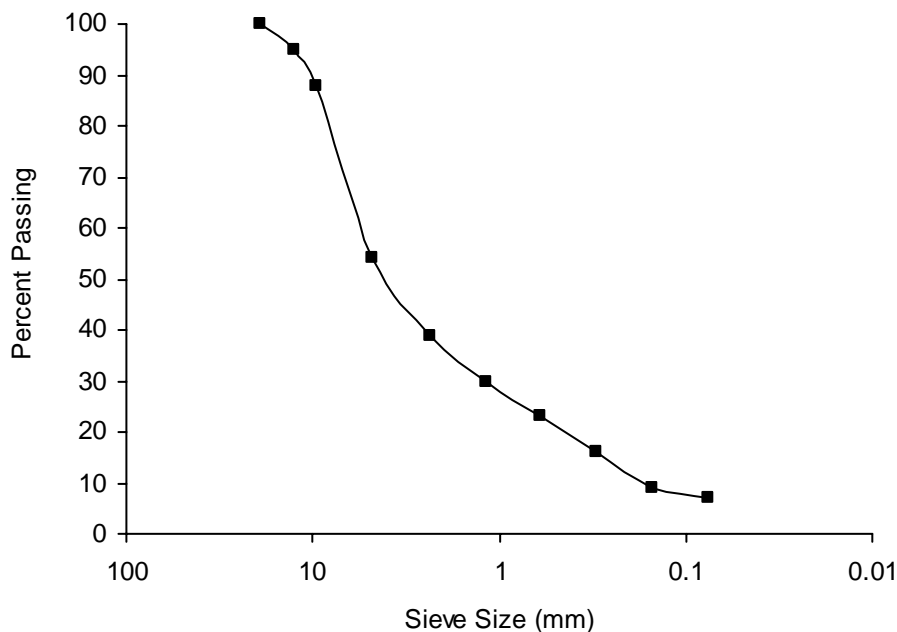


Figure 5.2.1 Grain size distribution of CRREL AC aggregate.

Table 5.2.3 presents as-constructed properties for the base aggregate layer. Thickness was determined from 8 rod and level measurements within each test section. The increased asphalt concrete thickness seen in Sections 3 and 4 was partially offset by a decreased base thickness. Density was based on two sand cone tests conducted within each test section. Coefficient of variation could not be calculated for these measurements. Moisture content was based on 24 measurements from samples taken from trenches excavated after loading was completed.

Table 5.2.3 As-constructed base aggregate properties for CRREL sections.

Section	Thickness (mm)	Density (kN/m ³)	Moisture Content (%)	Coefficient of Variation (%)		
				Thickness	Density	Moisture Content
CRREL1	331	21.7	3.4	3.8	NA	11.5
CRREL2	331	21.3	3.9	3.5	NA	10.3
CRREL3	323	21.5	4.0	2.9	NA	21.1
CRREL4	322	22.0	3.2	2.5	NA	14.5

Two trenches were made across the wheel path of the test sections at approximately the quarter points from the ends of the wheel patch. The asphalt concrete was cut with a dry saw and the layer removed. Samples of base course were obtained from the top of the layer at two locations per trench and at the bottom of the base at these same two locations. One location was

directly under the wheel path while the other was at a distance of 0.6 m from the center of the wheel path. Figures 5.2.2-5.2.5 show results from all trenches at each of the four locations sampled. Each figure contains results from one location for each of the two trenches for all test sections. A key to the data lines is not provided since the results indicate no significant differences between test sections or between sampling locations. If base contamination had occurred, a greater amount of fines in the location at the bottom of the base under the wheel path would be expected, which has not occurred.

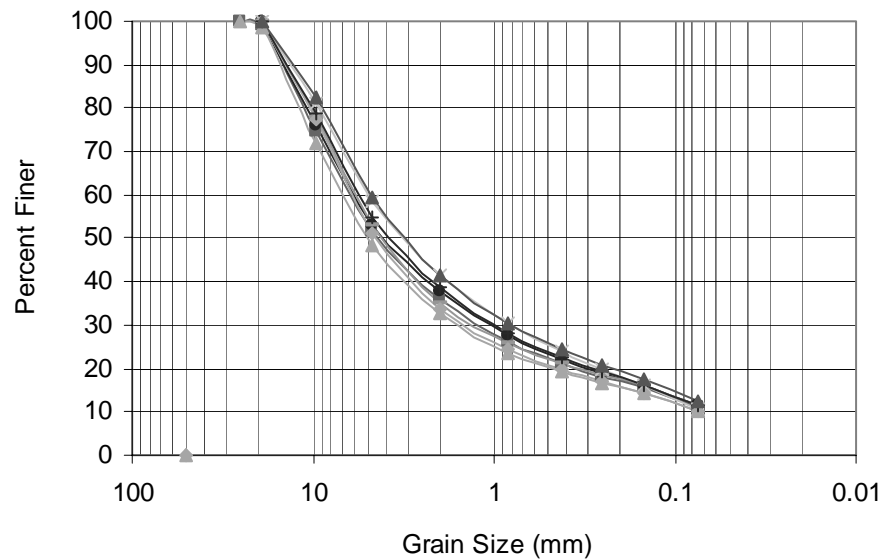


Figure 5.2.2 Grain size distribution of CRREL base aggregate at the top of the base under the wheel load.

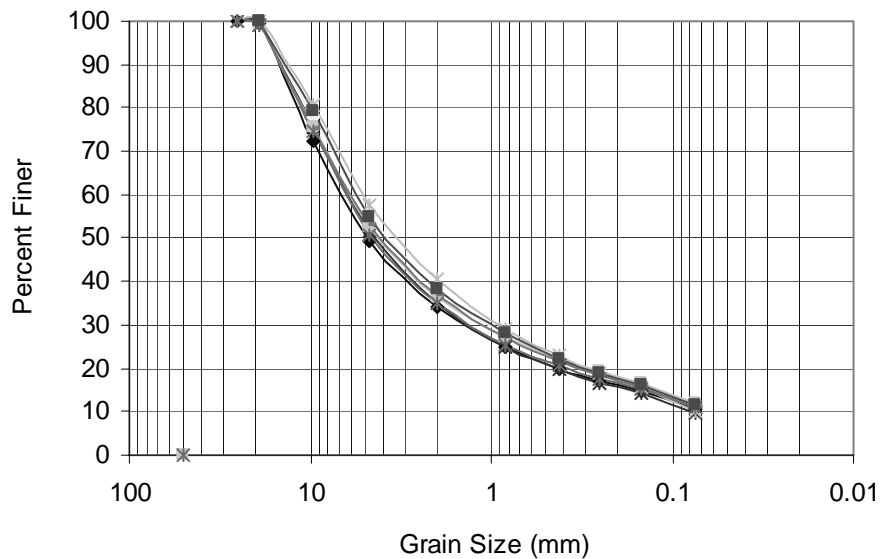


Figure 5.2.3 Grain size distribution of CRREL base aggregate at the top of the base 0.6 m away from the wheel travel path centerline.

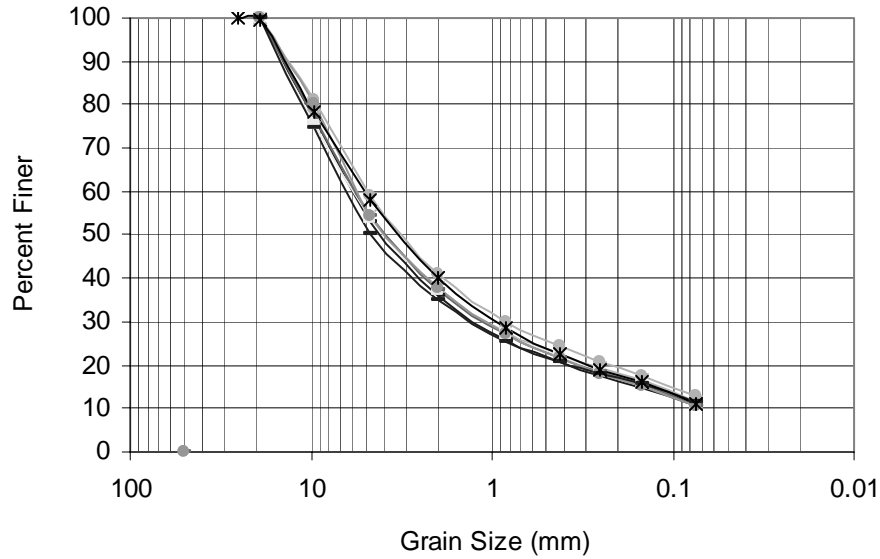


Figure 5.2.4 Grain size distribution of CRREL base aggregate at the bottom of the base under the wheel load.

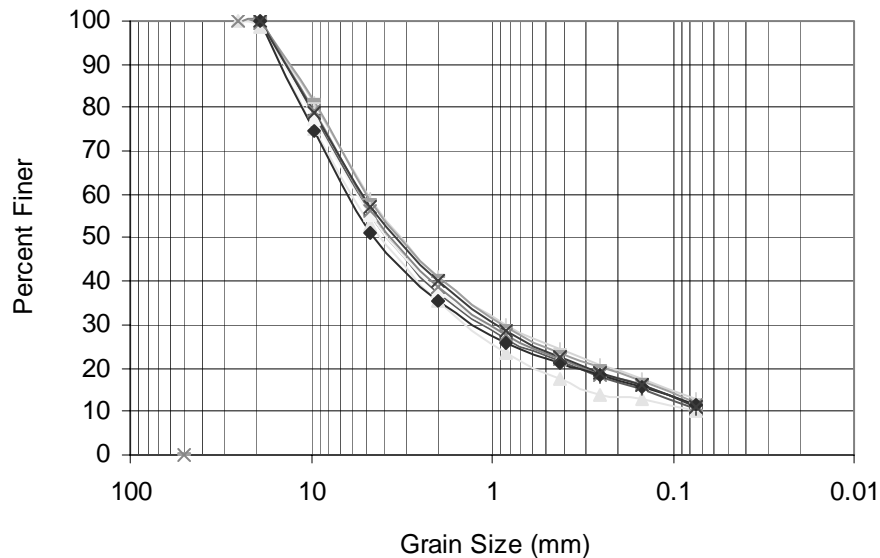


Figure 5.2.5 Grain size distribution of CRREL base aggregate at the bottom of the base 0.6 m away from the wheel travel path centerline.

Dynamic cone penetrometer (DCP) tests were performed in the base through holes drilled through the asphalt concrete. The holes were drilled in the location of where the trench was subsequently excavated. Holes were drilled directly under the wheel path and at a distance of 0.8 m from the centerline of the wheel path. Figures 5.2.6-5.2.13 show results for each test location.

Depth is measured from the top of the base layer. The test location away from the wheel load is indicative of as-constructed conditions as it should be minimally influenced by traffic loading. The location under the wheel load can be compared to the location away from the wheel load to ascertain the effect of traffic on the base layer. In general, the CBR of the base is seen to increase for the location under the wheel load as compared to the location away from the wheel load. This increase appears to be greatest from sections CRREL1, CRREL3, CRREL2 to CRREL4 and appears to follow the order of test section performance. Differences in locations away from the wheel load between test sections do not appear to be significant.

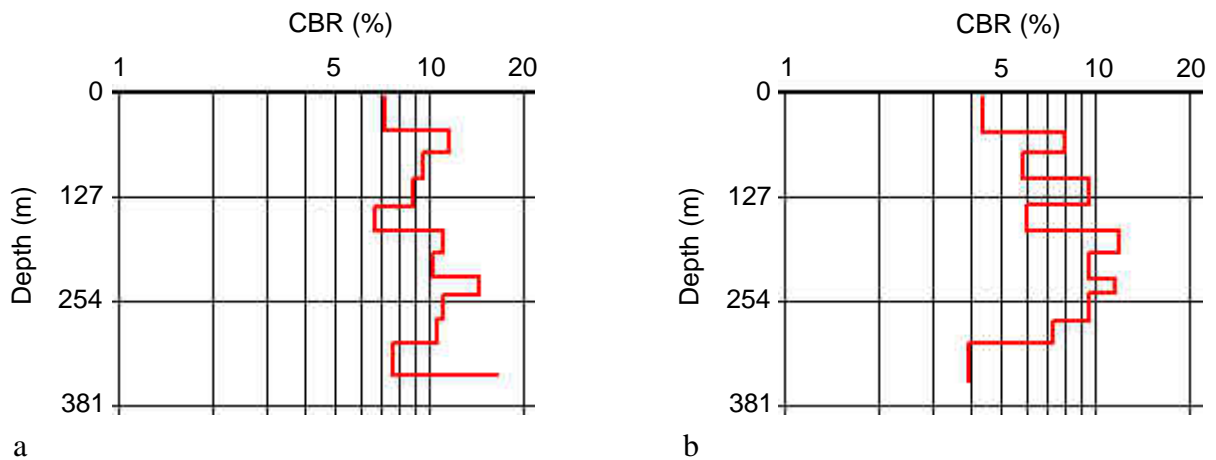


Figure 5.2.6 CBR from DCP tests in north end of section CRREL1 base aggregate a) under wheel load, b) 0.8 m away from centerline of wheel travel path.

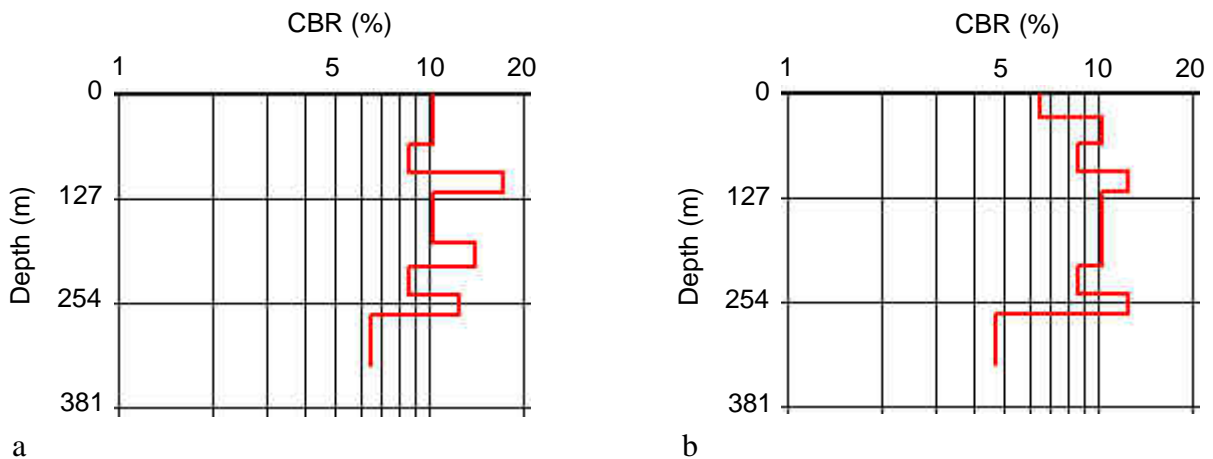


Figure 5.2.7 CBR from DCP tests in south end of section CRREL1 base aggregate a) under wheel load, b) 0.8 m away from centerline of wheel travel path.

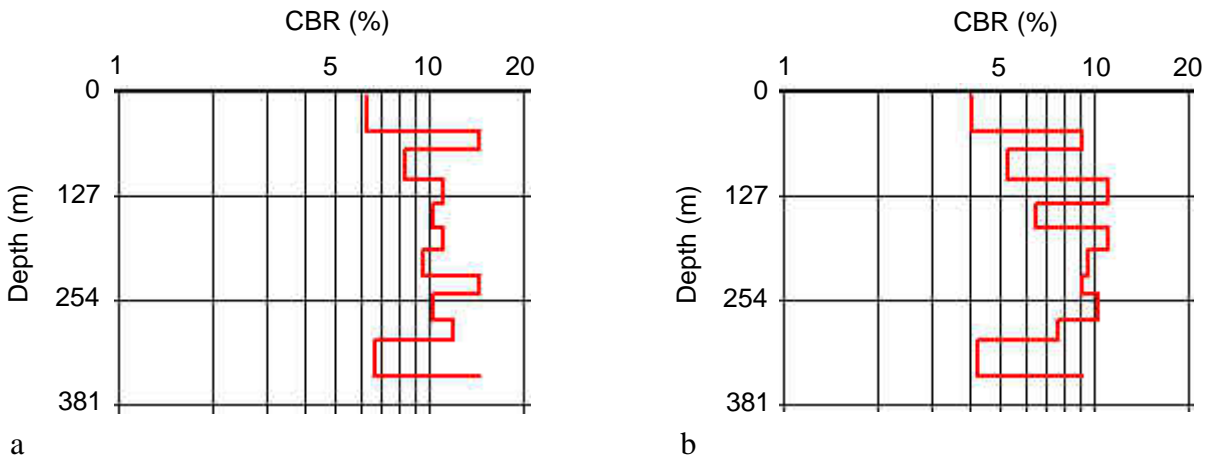


Figure 5.2.8 CBR from DCP tests in north end of section CRREL2 base aggregate a) under wheel load, b) 0.8 m away from centerline of wheel travel path.

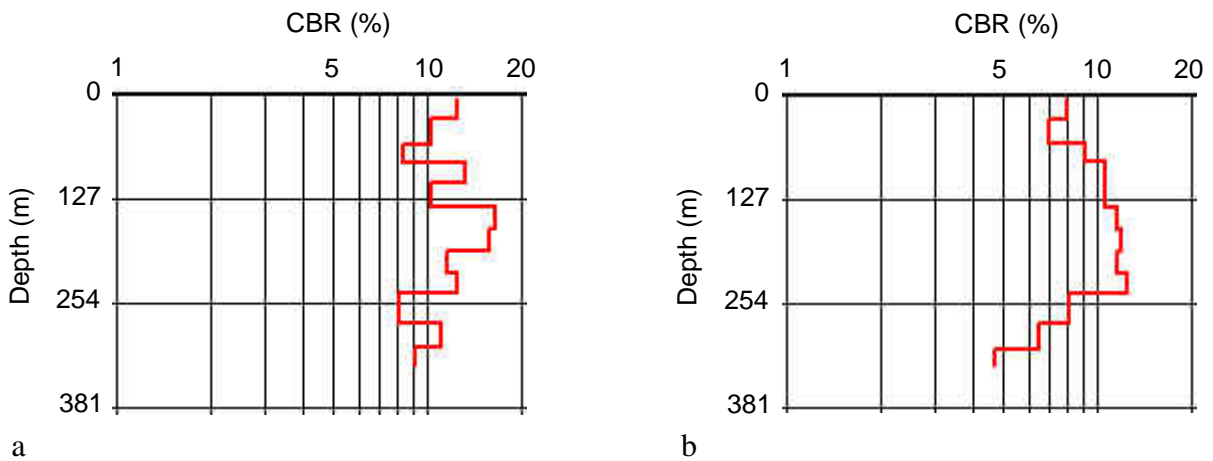


Figure 5.2.9 CBR from DCP tests in south end of section CRREL2 base aggregate a) under wheel load, b) 0.8 m away from centerline of wheel travel path.

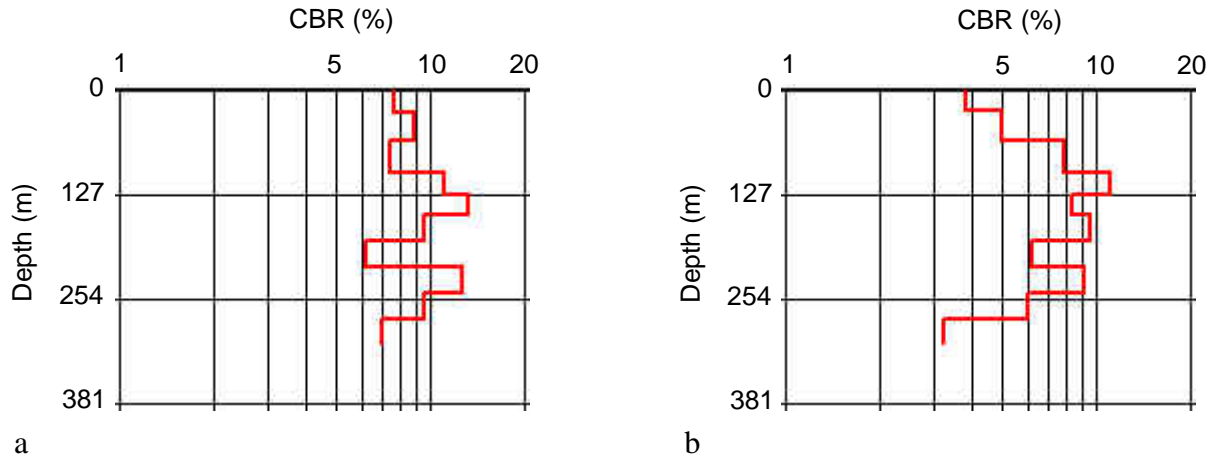


Figure 5.2.10 CBR from DCP tests in north end of section CRREL3 base aggregate a) under wheel load, b) 0.8 m away from centerline of wheel travel path.

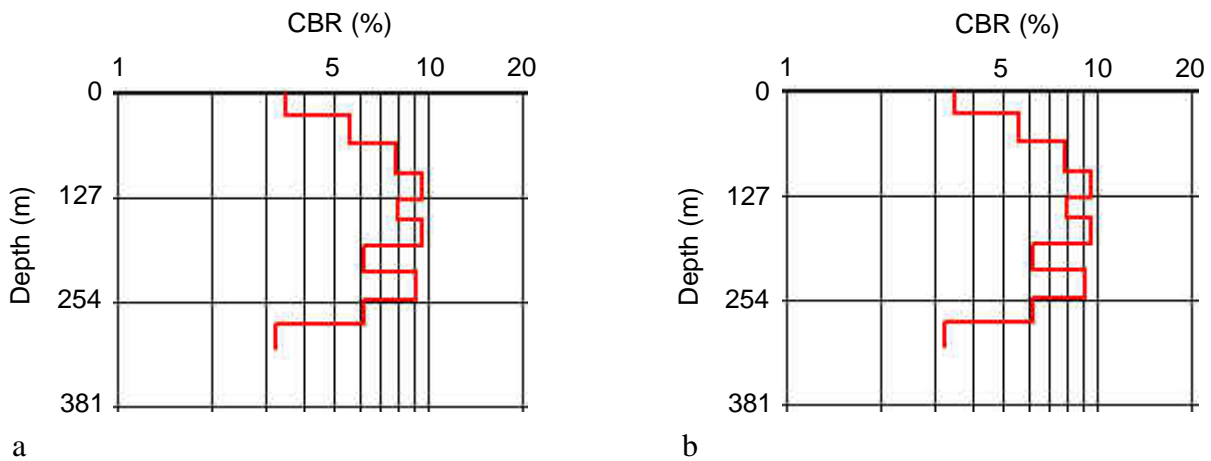


Figure 5.2.11 CBR from DCP tests in south end of section CRREL3 base aggregate a) under wheel load, b) 0.8 m away from centerline of wheel travel path.

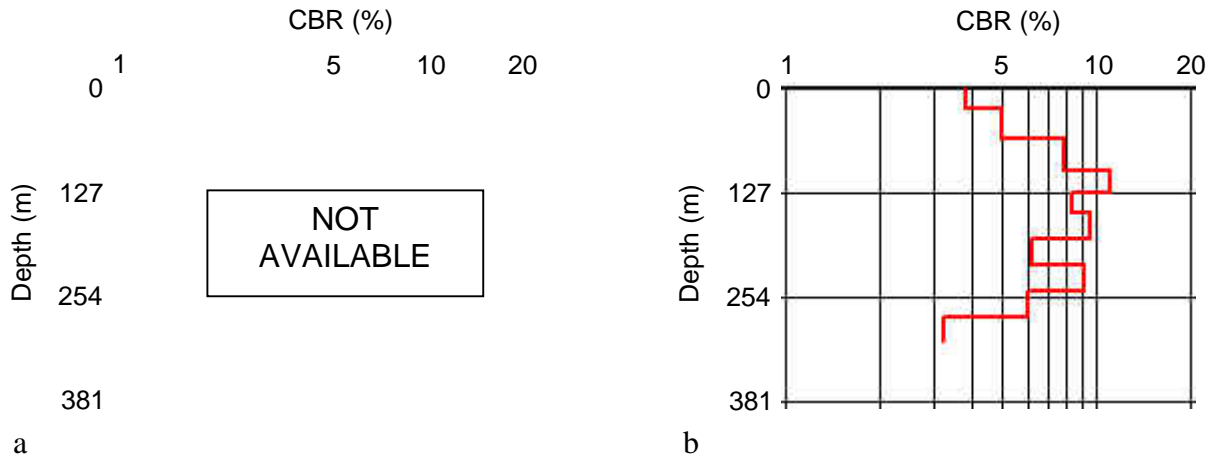


Figure 5.2.12 CBR from DCP tests in north end of section CRREL4 base aggregate a) under wheel load, b) 0.8 m away from centerline of wheel travel path.

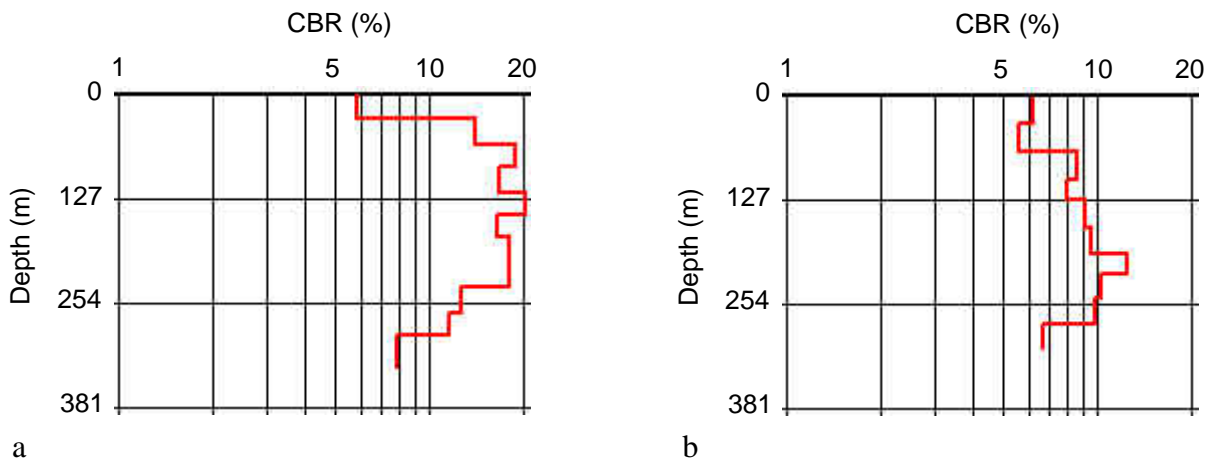


Figure 5.2.13 CBR from DCP tests in south end of section CRREL4 base aggregate a) under wheel load, b) 0.8 m away from centerline of wheel travel path.

Tables 5.2.4 and 5.2.5 provide as-constructed properties for the upper A-7(6) subgrade. Construction moisture content measurements were obtained from oven-dried samples for 5 locations for each of the 7 subgrade lifts. Nuclear density measurements were made at the same locations. Dry density was determined from total density and the oven-dried moisture content. Excavation moisture content was determined from 48 locations in trenches excavated after loading of the sections was completed. Two trenches were cut across the wheel path of each test section at approximately the quarter points from the ends of the wheel path.

Table 5.2.4 As-constructed subgrade properties for CRREL sections.

Section	Density (kN/m ³)	Moisture Content (%)	
		Construction	Excavation
CRREL1	14.7	28.2	23.5
CRREL2	14.7	28.1	23.6
CRREL3	14.8	28.3	24.2
CRREL4	14.8	27.9	22.0

Table 5.2.5 Coefficient of variation of as-constructed subgrade properties for CRREL sections.

Section	Coefficient of Variation (%)		
	Density	Moisture Content	
		Construction	Excavation
CRREL1	4.1	3.8	6.6
CRREL2	4.9	3.7	4.6
CRREL3	4.5	3.4	5.4
CRREL4	5.0	4.0	6.5

Dynamic cone penetrometer (DCP) tests were taken during construction once the subgrade finish grade was established. Two tests were taken for each test section corresponding to the two ends of the wheel travel path. DCP index was correlated to CBR through equations developed by Webster (1992). Figure 5.2.14 shows the variation of CBR with depth for each of the tests and shows a moderate data scatter within the upper 0.5 m. The majority of the results within the upper 0.5 m show CBR values ranging from 1 to 3. One test performed in test section CRREL4 showed uncharacteristically high values in the upper 0.5 m. Below 0.5 m, CBR is seen to increase, which is most likely due to resistance along the shaft of the DCP due to contact with the clay subgrade.

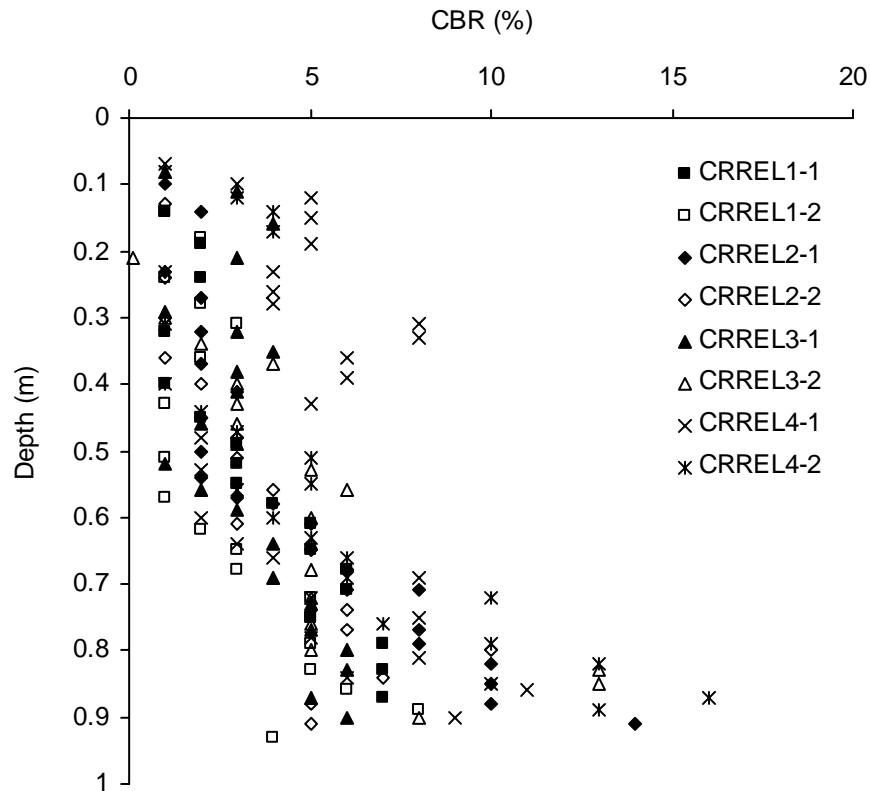


Figure 5.2.14 DCP tests in CRREL subgrade during construction.

DCP tests were also performed in the trenches excavated after loading was completed and correlated to CBR. Within each trench, DCP tests were conducted at four locations at two levels within the subgrade. The two levels from which the DCP tests were conducted correspond to the very top of the subgrade and 0.68 m below the pavement surface. Overlying materials were excavated down to each level prior to conducting the test. The DCP probe was advanced 300 mm for each test location. One set of duplicate tests was performed at a distance of 150 mm from the centerline of the wheel travel path. The second set was taken at a distance of 0.6 m from the wheel travel path centerline. For each test, DCP readings were averaged over the 300 mm drive. Duplicate tests within each set were then averaged, with CBR results shown in Table 5.2.6. Results for the set closest to the wheel travel path centerline are labeled as “under”. Results from the set at a distance of 0.6 m are labeled as “away”.

Table 5.2.6 CBR results from DCP tests taken during excavation in CRREL subgrade.

Test Section	Vertical Position	North Trench		South Trench		Average	
		Away	Under	Away	Under	Away	Under
CRREL1	Top	1.27	1.00	1.13	1.16	1.20	1.08
	Bottom	1.40	1.20	1.34	1.27	1.37	1.24
CRREL2	Top	1.78	1.10	1.49	0.98	1.64	1.04
	Bottom	1.38	1.02	1.31	0.95	1.34	1.19
CRREL3	Top	0.80	1.15	1.40	0.90	1.10	1.02
	Bottom	1.74	1.34	2.15	1.31	1.94	1.32
CRREL4	Top	0.79	1.26	1.06	1.34	0.92	1.30
	Bottom	1.45	1.08	1.10	1.22	1.28	1.15

Field CBR tests were also conducted within the trenches excavated after loading was completed. Two tests were conducted at two levels within the subgrade corresponding to the very top of the subgrade and 0.68 m below the pavement surface. Overlying materials were excavated down to each level prior to conducting the test. At each level, the two tests correspond to a distance of 100 mm (“under”) and 600 mm (“away”) away from the wheel travel path centerline. Results from these tests are given in Table 5.2.7. The values are approximately twice those determined from the DCP tests correlated to CBR.

Table 5.2.7 Field CBR results from tests taken during excavation in CRREL subgrade.

Test Section	Vertical Position	North Trench		South Trench		Average	
		Away	Under	Away	Under	Away	Under
CRREL1	Top	3	3	2	3	2.5	3.0
	Bottom	3	1	2	2	2.0	2.0
CRREL2	Top	2	2	1	2	1.5	2.0
	Bottom	2	4	3	2	3.0	3.0
CRREL3	Top	3	2	2	2	2.5	2.0
	Bottom	2	3	4	2	3.0	2.5
CRREL4	Top	2	3	3	4	2.5	3.5
	Bottom	4	3	3	4	3.5	3.5

A portable FWD was used to measure the stiffness of the subgrade at the same locations where field CBR tests were conducted. Values of resilient modulus in units of MPa are given in Table 5.2.8. As this device was not calibrated for this material, these values should be taken as

index values. The values tend to indicate, however, a corresponding subgrade CBR that is greater than that seen during construction and tends to show an aging effect in the material.

Table 5.2.8 Portable FWD modulus measurements during excavation in CRREL subgrade.

Test Section	Vertical Position	Modulus (MPa)					
		North Trench		South Trench		Average	
		Away	Under	Away	Under	Away	Under
CRREL1	Top	30	35	34	33	32	34
	Bottom	39	30	38	34	38	32
CRREL2	Top	26	25	30	33	28	29
	Bottom	33	34	31	21	32	27
CRREL3	Top	30	34	35	37	32	35
	Bottom	44	47	51	32	47	39
CRREL4	Top	36	38	39	36	37	37
	Bottom	38	37	36	42	37	39

5.2.2 MSU/GTX Test Box

Table 5.2.9 shows the average peak load pressure on the load plate and the standard deviation of this load during each test. Also listed is the temperature in the test facility during loading. The majority of the temperature readings for the MSU sections were based on air temperature above the test section. For the GTX sections, temperature was measured in the mid-height of the AC layer.

Table 5.2.10 presents thickness, density and air voids data for the asphalt concrete in the MSU and GTX test sections. Average values of thickness, density and air voids were determined from approximately 18 100 and 150 mm diameter cores taken from the section after loading was complete. The coefficient of variation of each parameter is given.

Table 5.2.9 Loading conditions for MSU/GTX sections.

Section	Average Peak Load Pressure (kPa)	Standard Deviation of Peak Load Pressure (kPa)	Average Temperature (°C)
MSU 1	548	3.7	16
MSU 2	548	2.9	20
MSU T1	546	4.8	17
MSU T2	544	5.7	16
MSU T3	552	5.3	19
MSU T4	563	6.0	11
MSU T5	551	6.0	8
MSU T6	547	4.0	10
MSU T7	548	3.8	23
MSU R1	547	7.4	18
MSU R2	547	5.7	13
MSU R3	550	5.7	20
MSU R4	550	4.8	21
MSU R5	551	5.5	20
GTX1	546	20.5	24.6
GTX2	544	5.9	25.2
GTX3	549	4.2	25.1
GTX4	550	4.2	23.2
GTX5	548	4.0	22.3
GTX6	548	5.3	20.8
GTX7	551	4.5	21.0
GTX8	547	4.8	21.2
GTX9	545	5.3	20.8
GTX10	549/551	3.8/3.7	18.8/20.4
GTX11	546/549	5.8/3.8	18.9/21.5

Table 5.2.10 As-constructed asphalt concrete properties for MSU/GTX sections.

Section	Thickness (mm)	Density (kN/m ³)	Air Voids (%)	Coefficient of Variation (%)		
				Thickness	Density	Air Voids
MSU 1	78.4	23.1	3.3	2.3	0.4	12.6
MSU 2	76.3	23.1	3.3	2.7	0.7	17.9
MSU T1	75.7	22.8	5.5	5.7	1.0	21.9
MSU T2	80.7	23.1	3.2	3.8	0.8	17.5
MSU T3	78.5	23.0	4.4	9.7	1.4	30.6
MSU T4	78.5	22.8	5.2	9.7	1.8	40.4
MSU T5	81.7	22.0	8.3	4.9	1.8	20.3
MSU T6	67.3	22.9	5.1	5.7	1.3	32.0
MSU T7	80.8	23.4	3.4	1.8	1.4	40.4
MSU R1	78.4	22.8	5.5	2.5	1.5	33.0
MSU R2	81.3	23.2	3.5	4.5	0.9	40.3
MSU R3	79.4	23.9	3.5	2.6	2.8	26.2
MSU R4	79.3	23.1	3.7	3.9	0.9	25.4
MSU R5	77.8	23.1	3.8	4.6	1.3	22.8
GTX1	86.3	22.6	10.0	10.9	1.9	17.2
GTX2	82.2	21.9	9.4	11.5	1.7	16.6
GTX3	87.3	22.4	6.35	2.8	1.9	17.2
GTX4	93.3	22.7	6.0	5.9	1.2	23.6
GTX5	84.9	22.3	7.4	4.6	1.5	19.0
GTX6	70.2	22.2	9.6	9.0	0.6	5.6
GTX7	79.6	21.8	8.4	1.0	2.7	29.0
GTX8	78.9	21.4	11.3	1.9	1.1	9.0
GTX9	79.8	21.9	9.3	1.1	1.4	13.2
GTX10	83.9	21.8	11.9	14.4	1.7	12.6
GTX11	87.0	22.1	8.4	8.9	0.4	3.9

Table 5.2.11 presents results of indirect tension resilient modulus tests performed on cores from the MSU and GTX test sections. Two tests were performed on two cores from each of the sections. For each test, resilient modulus was determined for three loading frequencies (1, 0.5 and 0.33 Hz), two orientations 90 degrees apart and at three temperatures yielding 18 values of resilient modulus for each specimen. The 6 tests at each temperature were averaged. A linear regression equation was then fit to the resulting three values of resilient modulus versus testing temperature. The average temperature during pavement loading for the test section was then used to determine the resilient modulus for that section and corresponds to the numbers reported in Table 5.2.11. Tensile strength was then determined at the intermediate temperature value for

each core. The asphalt used in the MSU sections tends to show a modulus approximately twice as great as that for the GTX sections.

Table 5.2.11 Resilient modulus and tensile strength of asphalt concrete for MSU/GTX sections.

Section	Resilient Modulus (MPa)	Tensile Strength (kPa)
MSU 1	2384	865
MSU 2	2650	567
MSU T1	3713	714
MSU T2	2650	ND
MSU T3	3447	722
MSU T4	3713	ND
MSU T5	2916	1109
MSU T6	5042	ND
MSU T7	5840	ND
MSU R1	5308	ND
MSU R2	1852	ND
MSU R3	3182	562
MSU R4	4511	732
MSU R5	2650	680
GTX1	767	199
GTX2	978	211
GTX3	1215	170
GTX4	2072	409
GTX5	1292	520
GTX6	1686	334
GTX7	1131	375
GTX8	1451	362
GTX9	1202	233
GTX10	1422	155
GTX11	NA	NA

Table 5.2.12 lists other properties including results from Marshall tests, asphalt content, asphalt penetration, asphalt kinematic viscosity and rice specific gravity on asphalt materials from the test sections.

Table 5.2.12 General properties of asphalt concrete for MSU/GTX sections.

Section	Marshalls				Asphalt Content (%)	Asphalt Penetration	Asphalt Kinematic Viscosity	Rice Specific Gravity
	100 mm Cores		Bulk Material					
	Stability (lb)	Flow	Stability (lb)	Flow				
MSU 1	2013	26.0	2140	15.0	6.8	ND	ND	2.437
MSU 2	2527	15.0	2942	13.0	6.1	ND	ND	2.462
MSU T1	2219	30.7	2450	11.7	5.7	ND	ND	2.472
MSU T2	2513	17.3	2616	15.0	6.3	ND	ND	2.445
MSU T3	3094	16.9	3350	11.5	6.1	40	696	2.464
MSU T4	2084	14.0	2738	9.5	6.0	78	387	2.473
MSU T5	1328	13.4	2350	9.0	5.9	71	391	2.455
MSU T6	1137	13.0	2879	10.0	6.6	75	403	2.465
MSU T7	1907	15.0	2838	12.0	6.0	86	330	2.462
MSU R1	2306	17.5	2375	11.0	6.2	ND	ND	2.459
MSU R2	2563	16.6	2750	12.2	6.3	ND	ND	2.444
MSU R3	2816	15.9	2825	10.6	6.1	ND	ND	2.458
MSU R4	2447	16.3	2633	11.0	6.2	ND	ND	2.455
MSU R5	2334	18.0	2913	13.0	6.2	75	372	2.466
GTX1	1617	13.5	5703	11.5	5.3	ND	ND	2.562
GTX2	1623	13.0	4413	10.0	5.4	ND	ND	2.447
GTX3	2391	12.5	4701	13.0	5.3	ND	ND	2.440
GTX4	1946	13.5	4029	12.5	6.6	ND	ND	2.446
GTX5	7252	19.5	3446	14.3	6.1	76	239	2.458
GTX6	6968	8.5	2571	12.5	5.5	75	241	2.499
GTX7	5336	14.5	2234	13.0	6.6	77	252	2.424
GTX8	3988	11.0	1591	15.5	6.7	73	242	2.457
GTX9	3590	11.0	1900	13.0	6.0	74	234	2.458
GTX10	1924	11.0	4096	11.5	4.7	78	229	2.514
GTX11	NA	NA	3495	10.5	5.4	74	241	2.462

Table 5.2.13 presents as-constructed properties for the base aggregate layer in the MSU/GTX test sections. Thickness was determined from 5 rod and level measurements within each test section. Density and moisture content were determined from 15 measurements within each test section.

Table 5.2.13 As-constructed base aggregate properties for MSU/GTX sections.

Section	Thickness (mm)	Density (kN/m ³)	Moisture Content (%)	Coefficient of Variation (%)	
				Density	Moisture Content
MSU 1	300	20.6	6.3	1.2	9.0
MSU 2	300	20.7	6.9	1.8	3.2
MSU T1	175	20.9	6.0	3.3	2.5
MSU T2	140	20.6	5.7	4.9	5.1
MSU T3	140	21.5	6.6	2.0	5.3
MSU T4	175	19.3	6.3	4.8	19.2
MSU T5	200	19.6	6.0	3.1	2.9
MSU T6	175	21.0	6.5	6.1	2.8
MSU T7	200	21.9	5.8	13.9	1.9
MSU R1	300	21.3	6.7	2.0	11.0
MSU R2	300	20.7	5.7	2.4	3.5
MSU R3	300	21.1	6.3	3.7	13.6
MSU R4	300	21.4	6.6	2.4	17.1
MSU R5	300	20.6	6.9	2.6	5.1
GTX1	302	22.2	7.2	3.4	13.0
GTX2	299	22.3	7.8	3.3	7.6
GTX3	296	22.2	5.8	2.6	7.2
GTX4	299	21.3	6.9	1.7	11.7
GTX5	296	21.0	6.2	1.4	7.4
GTX6	299	21.3	5.5	3.0	9.4
GTX7	299	20.9	6.4	2.5	8.6
GTX8	299	20.9	6.7	2.5	12.9
GTX9	299	20.8	6.6	1.4	0.9
GTX10	299	20.1	6.6	1.2	2.1
GTX11	299	20.7	6.4	2.2	9.6

As-constructed properties of the subgrade are listed in Table 5.2.14. Average values of moisture content and dry density measured during construction and during excavation are reported from approximately 40 and 50 samples, respectively. The coefficient of variation for moisture content and dry density within a given test section are shown in Table 5.2.15. The increase in vane shear readings from construction to excavation in the GTX sections tends to show that strength aging effects were occurring in this material.

Table 5.2.14 As-constructed subgrade properties in MSU/GTX sections.

Section	Thickness (mm)	Construction			Excavation		
		Moisture Content (%)	Dry Density (kN/m ³)	Vane Shear (kPa)	Moisture Content (%)	Dry Density (kN/m ³)	Vane Shear (kPa)
MSU 1	1045	44.8	11.4	NP	43.9	11.6	NP
MSU 2	1045	44.8	11.5	NP	44.5	11.5	NP
MSU T1	1170	44.3	11.4	NP	42.5	11.8	NP
MSU T2	1205	44.4	11.6	NP	45.6	11.8	NP
MSU T3	1205	45.1	11.8	NP	45.5	11.7	NP
MSU T4	1170	44.7	11.8	NP	42.6	11.8	NP
MSU T5	1145	43.5	11.9	NP	43.0	11.7	NP
MSU T6	1170	44.4	11.4	NP	44.6	11.5	43.3
MSU T7	1146	44.5	11.7	NP	44.7	11.6	41.7
MSU R1	1045	43.5	11.8	NP	45.9	11.6	NP
MSU R2	1045	44.2	11.7	NP	44.3	11.8	NP
MSU R3	1045	45.1	11.6	NP	42.4	12.5	NP
MSU R4	1045	44.8	11.8	NP	42.5	12.3	NP
MSU R5	1045	44.2	11.8	NP	43.0	12.1	NP
GTX1	1045	28.3	14.9	28.0	27.7	15.1	37.1
GTX2	1045	28.9	15.2	32.3	28.1	15.2	36.9
GTX3	1045	28.9	15.2	33.4	28.5	15.3	36.2
GTX4	1045	28.7	15.3	35.6	28.3	15.3	43.7
GTX5	1049	26.7	15.5	47.3	26.1	15.3	64.5
GTX6	1045	27.0	15.6	48.7	26.6	15.6	59.5
GTX7	1045	26.6	15.8	58.7	25.8	15.4	66.7
GTX8	1045	26.4	15.6	52.4	25.8	15.4	56.8
GTX9	1045	26.9	15.7	49.2	24.1	15.8	61.3
GTX10	1045	26.6	15.8	56.3	24.0	15.9	69.6
GTX11	1045	27.1	15.7	48.6	25.4	15.8	68.3

Table 5.2.15 Coefficient of variation of as-constructed subgrade properties for MSU/GTX sections.

Section	Coefficient of Variation (%)			
	Construction		Excavation	
	Moisture Content	Density	Moisture Content	Density
MSU 1	0.6	1.9	2.5	2.2
MSU 2	2.6	1.3	1.3	2.9
MSU T1	5.8	4.3	3.7	2.6
MSU T2	2.4	2.5	3.5	2.6
MSU T3	1.6	2.2	3.5	2.6
MSU T4	2.4	2.4	3.6	3.0
MSU T5	1.6	2.4	3.7	3.8
MSU T6	2.7	2.6	4.3	3.1
MSU T7	2.1	2.4	2.5	2.5
MSU R1	2.6	1.8	2.0	3.2
MSU R2	3.2	1.8	2.2	4.9
MSU R3	2.4	2.2	2.1	2.5
MSU R4	1.6	2.2	1.7	1.8
MSU R5	3.8	3.1	4.4	2.6
GTX1	2.9	2.8	9.0	5.4
GTX2	2.2	2.5	6.1	2.1
GTX3	2.8	1.6	4.2	1.4
GTX4	1.6	1.8	5.7	2.1
GTX5	2.2	1.9	6.4	1.8
GTX6	2.2	1.8	5.7	1.6
GTX7	2.2	2.0	7.0	2.3
GTX8	1.5	1.4	8.9	2.0
GTX9	1.8	1.7	5.1	1.1
GTX10	2.1	1.5	7.6	1.4
GTX11	1.5	1.4	4.9	1.4

6.0 RESULTS: CRREL/HVS/FERF

6.1 Rutting Behavior

The development of permanent deformation on the pavement surface (rutting) due to permanent vertical strain in the underlying materials (asphalt concrete, base aggregate and subgrade) was the predominant failure mode of the test sections. Other failure modes included asphalt concrete cracking, delamination and vertical shear. Rutting behavior is discussed in this section while the remaining failure modes are discussed in Section 6.2.

Cross-sectional surface profiles were taken at 20 locations along the wheel track at 0.30 m intervals for each pass level (0, 50, 100, 250, 500, 1000, 2500, 5000, 10000, 25000, 50000, 100000, 250000 wheel passes or until failure occurred). Each cross-section consisted of 256 depth measurements at 9 mm intervals. The surface profile for each cross-section was determined by first taking profile measurements before pavement loading (pass level 0), where the zero reference was the top of the concrete wall adjacent to the section. Raw measurements at subsequent pass levels were taken in the same manner. Each data set was then recomputed as a moving average of 5 data points surrounding the measurement point. This was done to average out fluctuations due to irregularities in the pavement surface. Each data set was then zeroed by subtracting the first data point from the remaining 255 data points such that a starting value of zero was obtained for the reading corresponding to the top of the concrete wall. For a given cross-section, the data reduced to this point showed the unevenness of the pavement surface. To compare results between sections and to examine only the deformations due to pavement loading, values at each of the 256 measurement points at pass level zero were treated as initial values and were subtracted from corresponding measurement points for all subsequent pass levels. A surface profile example following this data reduction is shown in Figure 6.1.1 for test section CRREL1 at the first cross section measurement location at pass level 10,000.

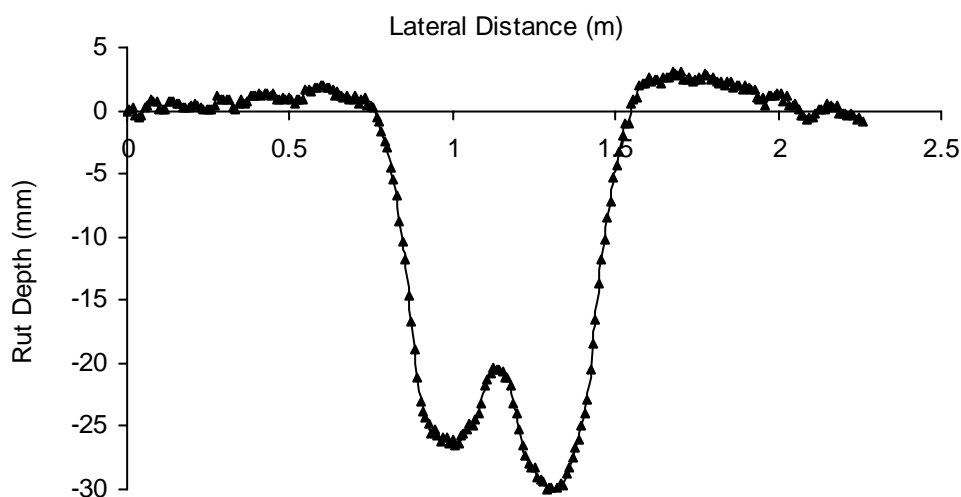


Figure 6.1.1 Averaged and zeroed rut profile for test section CRREL1 (control), location 1, pass level 10,000.

The minimum value (maximum rut depth) for each cross section at each pass level was then tabulated. Plots of rut depth versus position along the wheel path for all pass levels for test sections CRREL1-CRREL4 are shown in Figures 6.1.2 – 6.1.5 (materials used in the test sections are given in Table 5.1.1; a key to the geosynthetics used is given in Table 4.4.1). For all sections, loading took place from North to South.

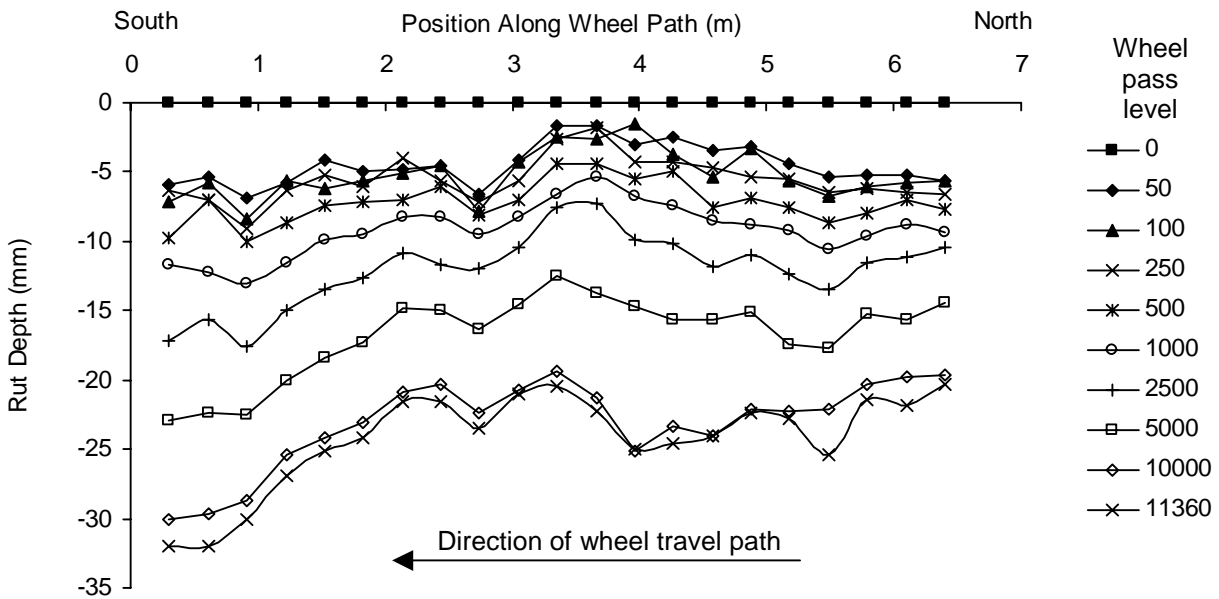


Figure 6.1.2 Rut depth vs. position along the wheel path for test section CRREL1 (control).

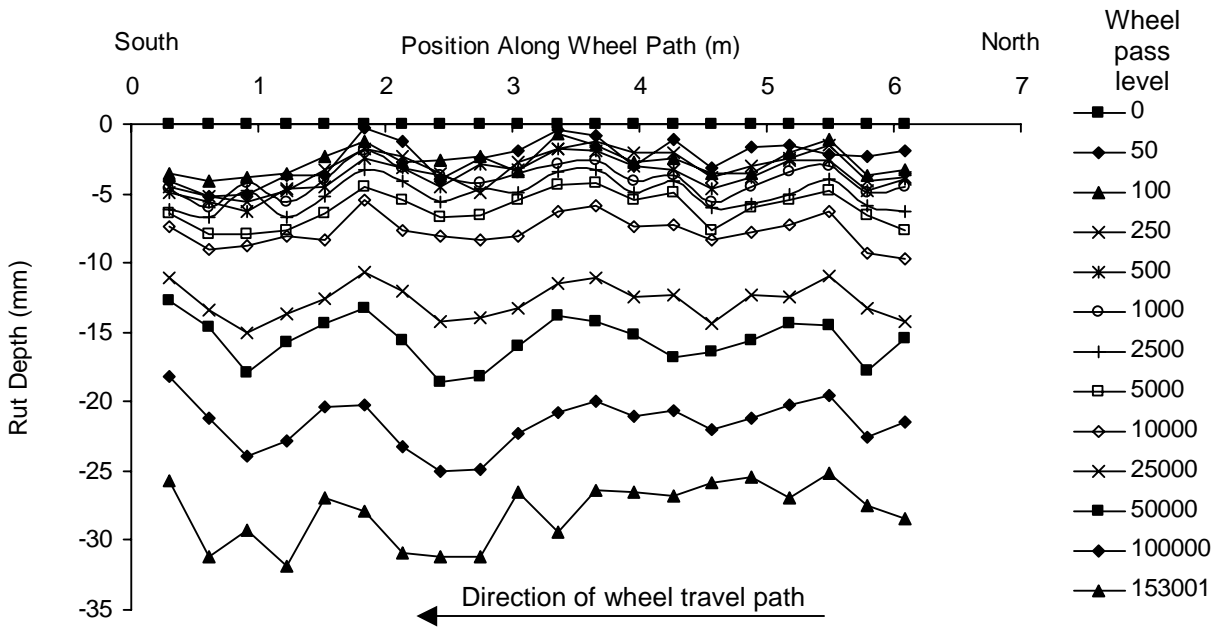


Figure 6.1.3 Rut depth vs. position along the wheel path for test section CRREL2 (geosynthetic G).

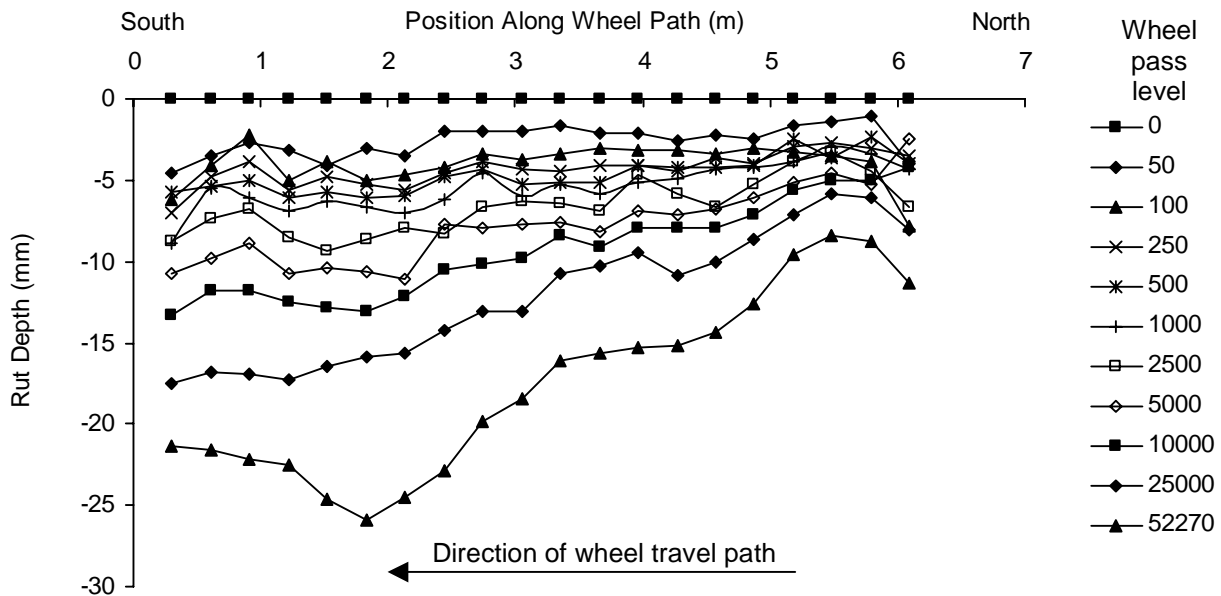


Figure 6.1.4 Rut depth vs. position along the wheel path for test section CRREL3 (geosynthetic A).

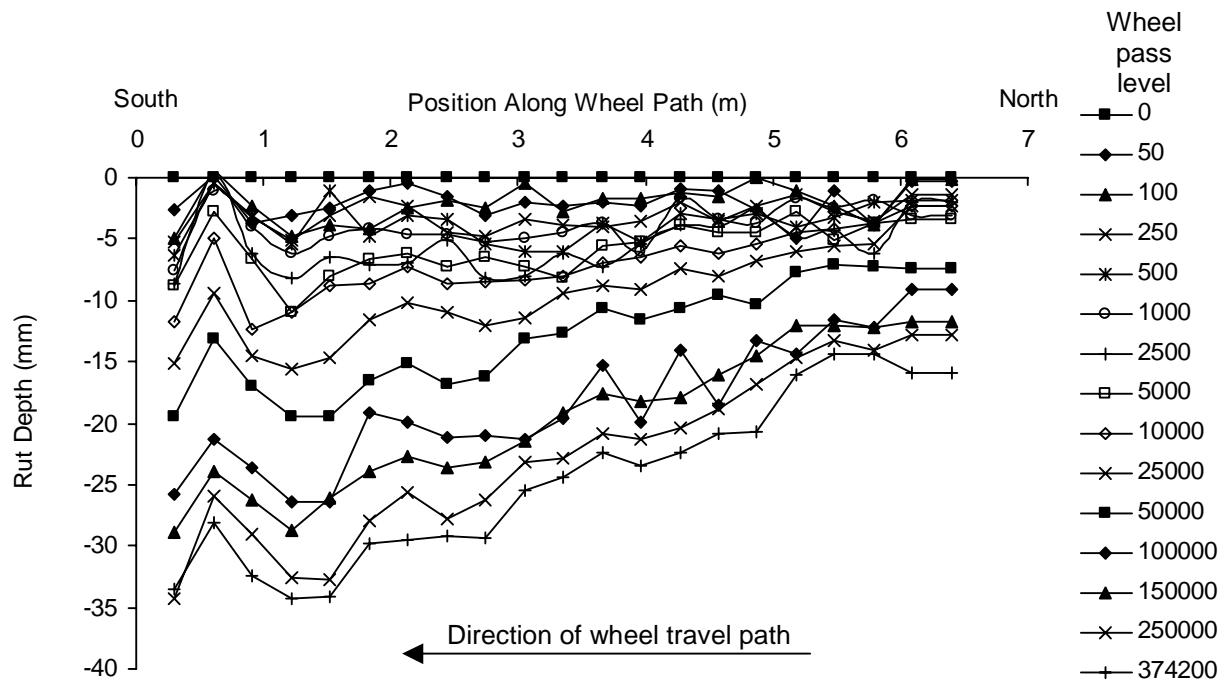


Figure 6.1.5 Rut depth vs. position along the wheel path for test section CRREL4 (geosynthetic H).

Rut depth was relatively uniform for the first 70 % of the wheel path for test section CRREL1. Towards the end of the wheel travel path (south end of the section) the rut depth was seen to increase by approximately 30 % as compared to the average over the 4.5 m towards the north end of the section. Asphalt cracking and delamination was noted in the north end of section CRREL1, however no significant asphalt fatigue problems were noted in the south end where the surface deformation was seen to increase. Section CRREL2 was immediately adjacent to section CRREL1, as shown in Figure 3.1.1. Rut depth was relatively uniform in this section.

Sections CRREL3 and CRREL4 were adjoined to the north end of sections CRREL1 and CRREL2 as shown in Figure 3.1.1. Loading of CRREL3 was terminated when an asphalt concrete delamination occurred at the 1.8 m point and prevented safe operation of the HVS over the section. In sections CRREL3 and CRREL4, rutting was seen to increase in the direction of the wheel travel path from north to south. The increase between the average of the first and last two measurement points going from north to south indicated an approximate 48 and 58 % increase in rut depth for sections CRREL3 and CRREL4, respectively. An examination of the quality control measures taken during construction and the forensic testing parameters collected

during excavation within test section CRREL4 did not indicate any significant trends that could help explain an increase in rutting in the direction of the wheel path. Parameters examined were asphalt concrete density and thickness, base aggregate density, water content, thickness, gradation and DCP resistance, and subgrade density, water content, DCP resistance, field CBR, vane shear, portable FWD. Parameters determined during excavation were made from two trenches excavated across the wheel path and may not be completely representative of changes in material from north to south ends of the section. A similar lack of correspondence between these parameters and increased rutting from north to south was seen in section CRREL1 and CRREL3.

It has been speculated that the direction of the wheel travel path induces a pore water pressure front that causes increased pore water pressure buildup towards the south end of the section. Furthermore, the woven geotextile may have prevented this pore water pressure from quickly dissipating into the base aggregate layer. Evidence of this behavior has been seen with this same subgrade and a different geotextile in the sections constructed in the GTX test box. Increased pore pressure would then lead to increased rutting. The behavior of section CRREL4 does not support this explanation. Section CRREL4 contained a geogrid, which would not prevent pore pressure from dissipating into the base layer. In addition, the fines content of the base aggregate used was relatively high, meaning that pore pressure drainage from the subgrade into the base was most likely slow in all test sections.

A comparison of rut depth between the sections has been made in two ways. First, the rut depth along the wheel path was averaged for each pass level and plotted against the number of wheel passes in Figure 6.1.6. The maximum and minimum rut depth along the wheel path for each pass level is plotted in Figure 6.1.7. The results show an order of performance defined in terms of rutting of sections CRREL1 (control), CRREL3 (geosynthetic A), CRREL2 (geosynthetic G) and CRREL4 (geosynthetic H). Based on average rut measurements, values of Traffic Benefit Ratio corresponding to 25 mm of 10.0 and 31.5 were obtained for sections CRREL2 and CRREL4, respectively. For a rut level of 17 mm, a TBR value for section CRREL3 of 9.0 was obtained. Direct comparison between sections should be performed keeping in mind the minor differences in average thicknesses and material properties of the test section layers and the significant variation of rut depth along the length of the section. Values of TBR for the test sections performed previously in the MSU test box and reported by Perkins (1999) for the same geosynthetics used in section CRREL2, CRREL3 and CRREL4 and using similar

layer materials and thickness were 17.0, 8.5 and 56, respectively. The values obtained in the CRREL sections appear to be comparable for the geotextile (CRREL3) and approximately 40 % lower for the geogrid sections.

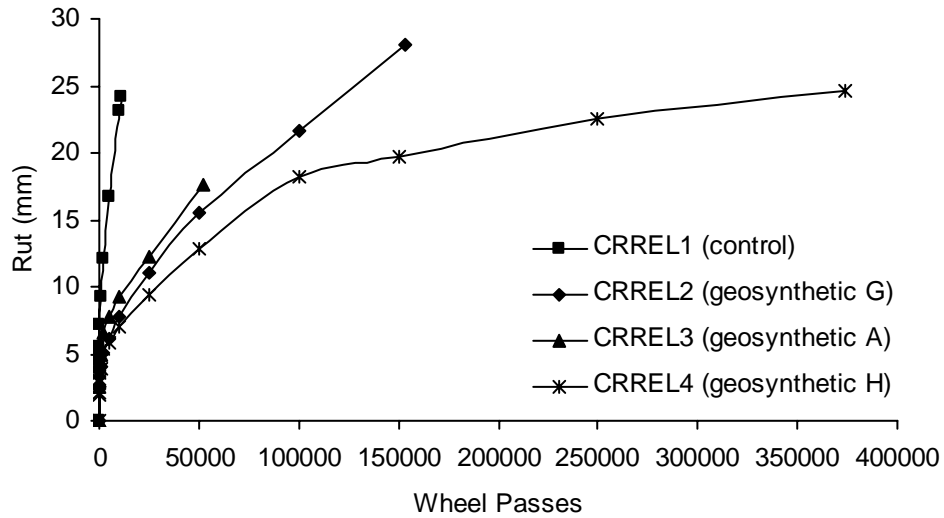


Figure 6.1.6 Average rut depth vs. wheel pass for all CRREL test sections.

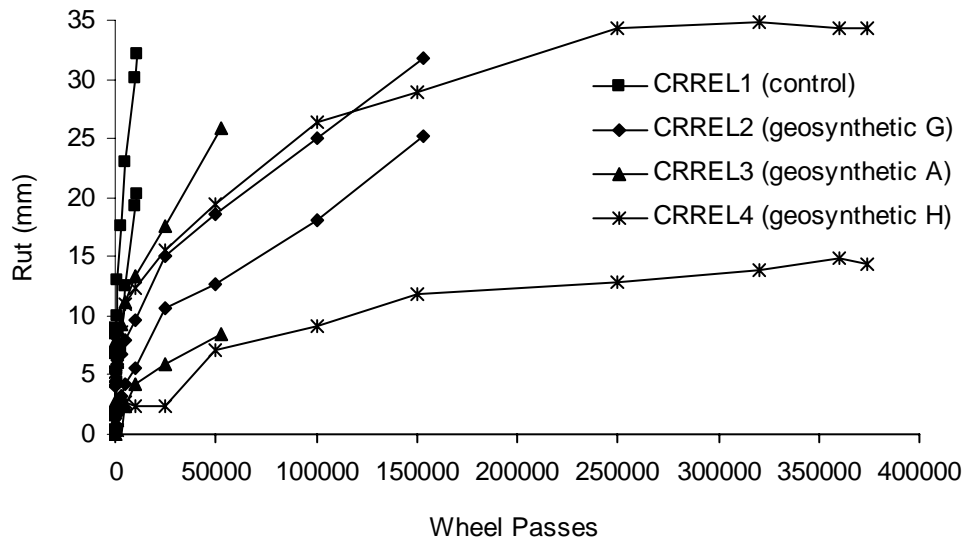


Figure 6.1.7 Maximum and minimum rut depth vs. wheel pass for all CRREL test sections.

The spreadsheet design program (Perkins 2001b) was used to predict TBR for the conditions present in the test sections. Values of 4.9, 2.4 and 6.4 were obtained for sections CRREL2, CRREL3 and CRREL4, respectively. In spite of the lower values of TBR determined directly from the test sections, the predictions from the design program are still considerably conservative. Table 6.1.1 lists TBR values from the CRREL sections, from the study of Perkins (1999) and from predictions using the spreadsheet design program of Perkins (2001b). Also listed in Table 6.1.1 are TBR values for the CRREL sections as determined from corresponding sets of maximum and minimum rut depths as given in Figure 6.1.7. For maximum rut depth measurements, TBR values were determined at a rut depth of 25 mm. For minimum rut depth measurements, TBR values were taken at the last data point available for a particular control-reinforced section combination. This corresponds to rut levels of 20, 8.2 and 14.2 mm for sections CRREL2, 3 and 4, respectively.

Table 6.1.1 Traffic Benefit Ratios (TBR) for CRREL sections and from previous studies.

Geosynthetic	TBR				
	CRREL Sections			Perkins (1999)	Perkins (2001b)
	Average Rut	Maximum Rut	Minimum Rut		
A	9.0	7.7	19.5	8.5	2.4
G	10.0	17.7	10.2	17.0	4.9
H	31.5	13.8	56.6	56.0	6.4

6.2 Performance Behavior

Digital photographs were taken of the test sections after the completion of loading to document the condition of the pavement. Figures 6.2.1-6.2.4 show photo mosaics of the test sections and close-up photos of distinct failure features. Figure 6.2.5 shows a photo of all test sections.

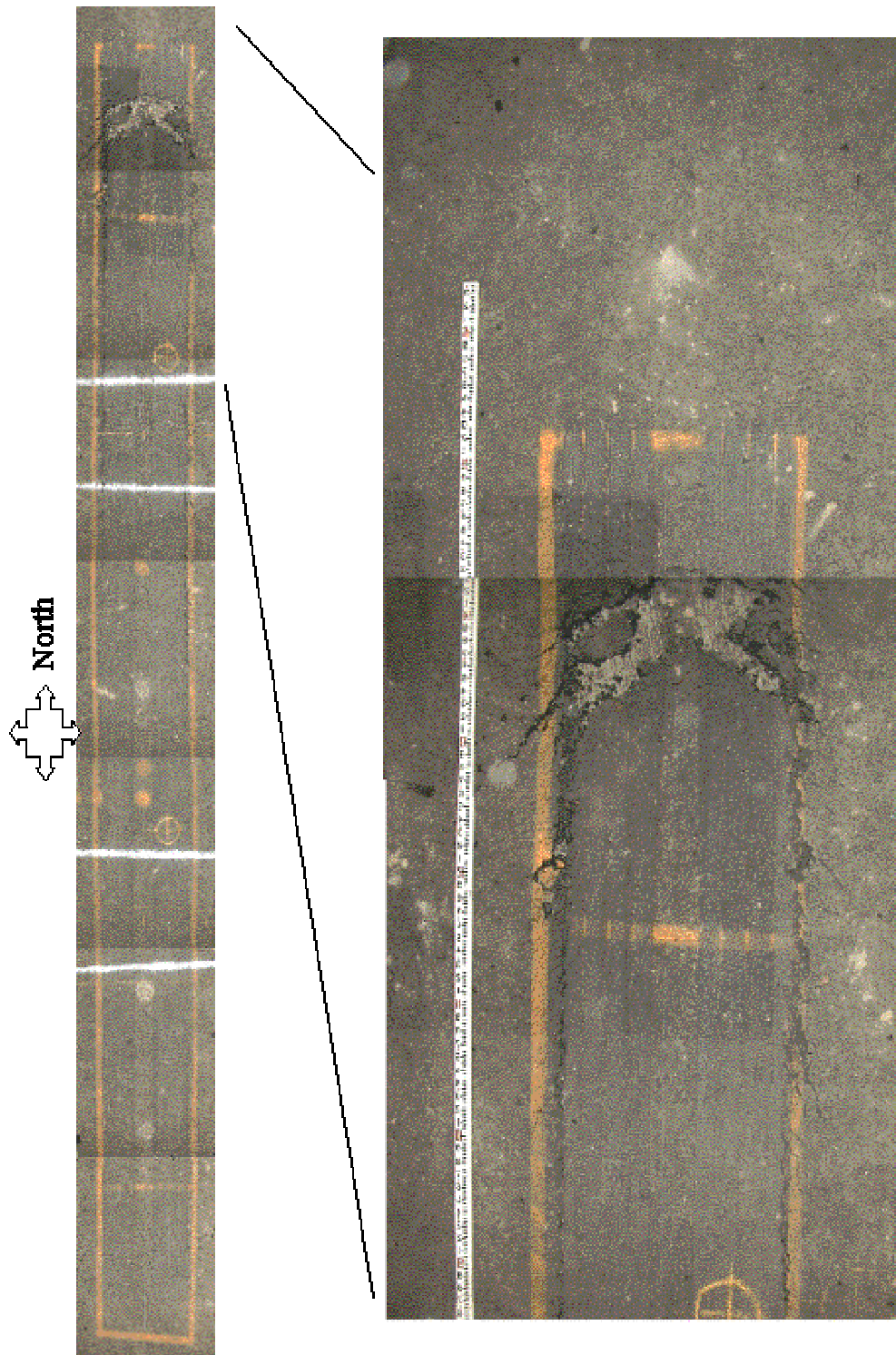


Figure 6.2.1 Photo mosaic of section CRREL1 (control).

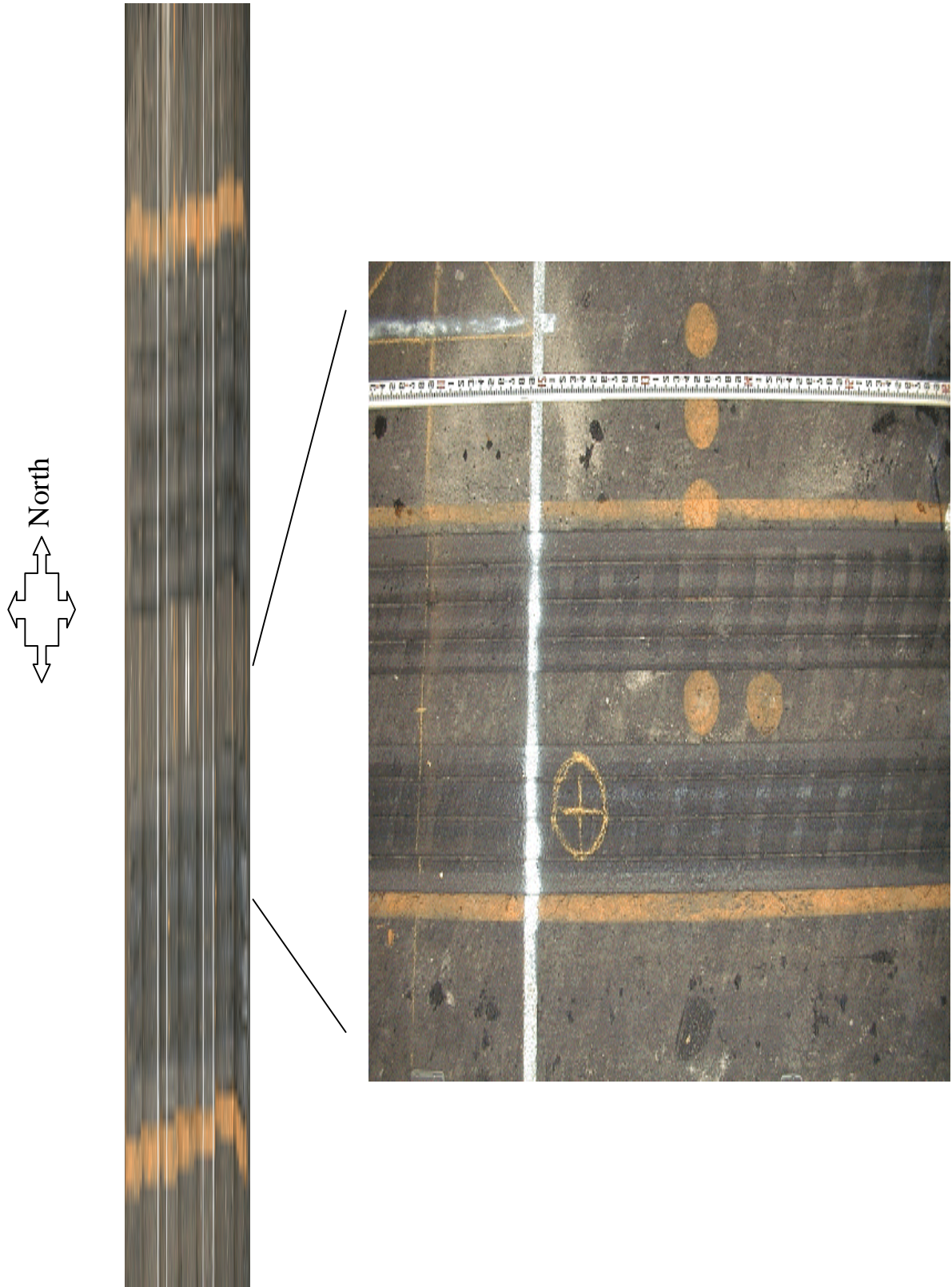


Figure 6.2.2 Photo mosaic of section CRREL2 (geosynthetic G).

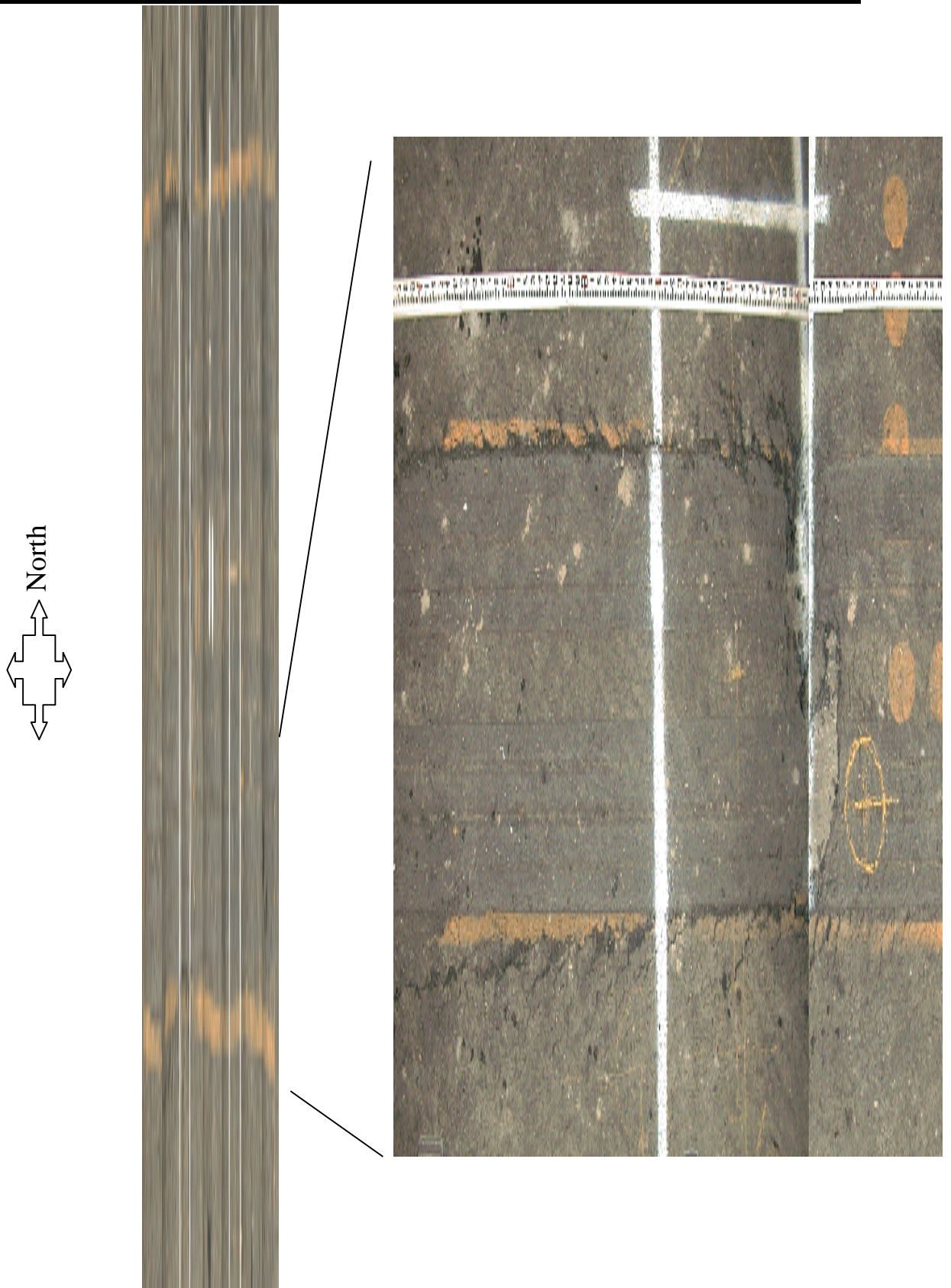


Figure 6.2.3 Photo mosaic of section CRREL3 (geosynthetic A).

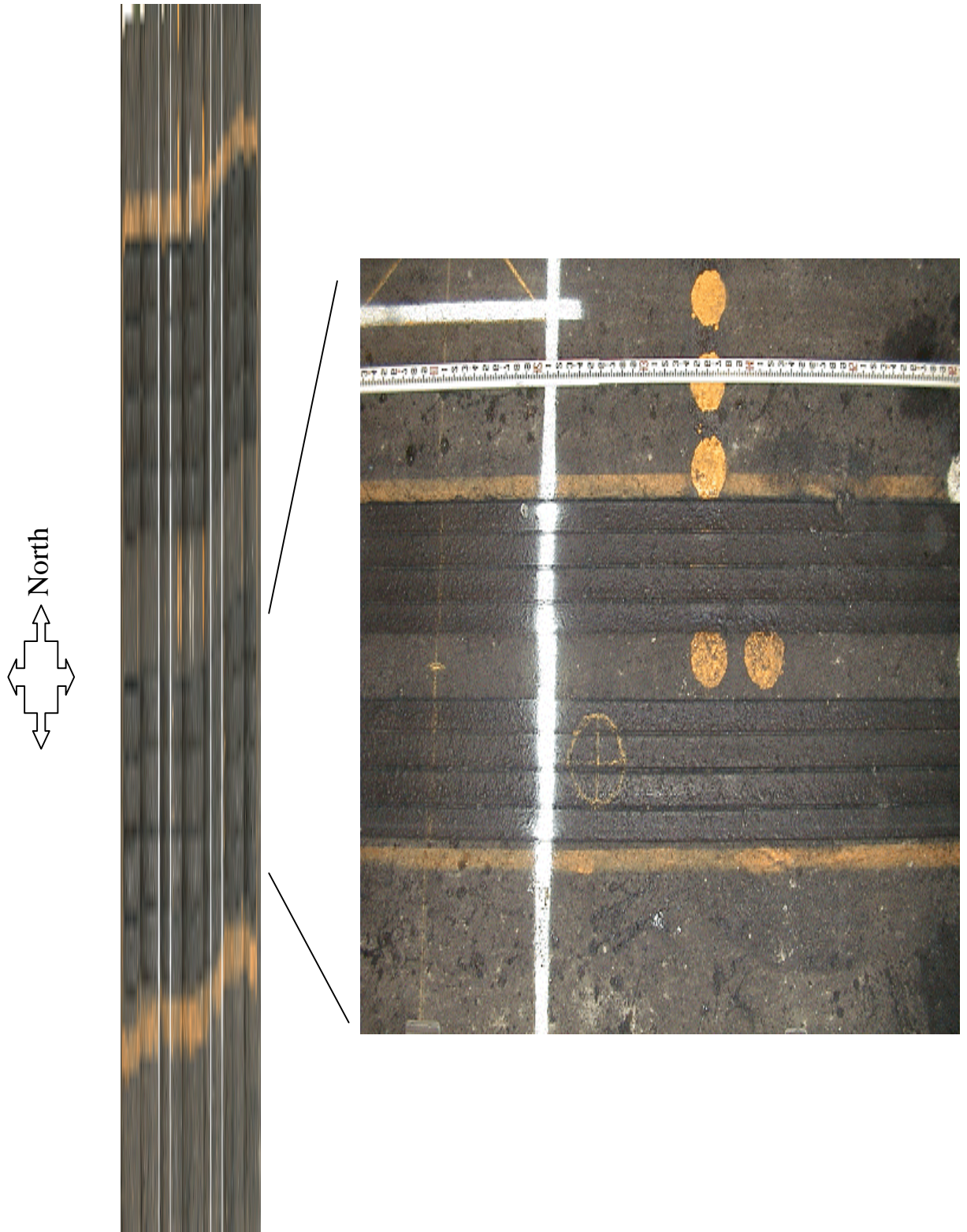


Figure 6.2.4 Photo mosaic of section CRREL4 (geosynthetic H).

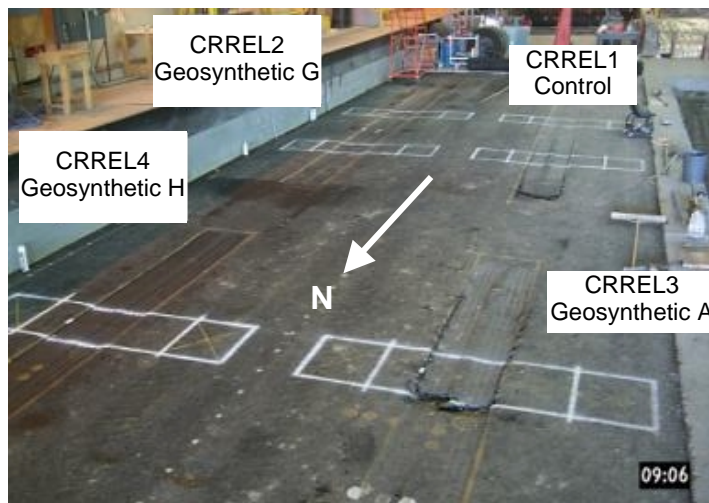


Figure 6.2.5 Photo of all CRREL sections.

Section CRREL1 developed a transverse tension crack and longitudinal shear cracks along the edges of the wheel track associated with a delamination that occurred between the binder and surface courses at the North (acceleration end) of the section. The crack was first noticed at 10,000 wheel passes and occurred towards the end of the loading. The rutting of the section did not appear to be influenced by the development of this crack prior to 10,000 wheel passes. Figure 6.2.6 shows a closer view of the delaminated area where a clear slip surface is observable between the two pavement courses. The remainder of the section was free of other cracking or fatigue related distress features.

Test section CRREL2 developed a very uniform rut shape and was also uniform along the wheel travel path. No visible cracking or other fatigue related distress features were noted along the section.



Figure 6.2.6 Photo of delamination in section CRREL1 (control).

Test section CRREL3 developed a transverse tension crack and associated vertical shear cracks within the last quarter of the section and was first noticed at 44,000 wheel passes. Figure 6.2.7 shows the transverse tension crack and a portion of the vertical shear cracks. Figure 6.2.8 shows two close-up views of the transverse crack. Figure 6.2.9 shows another view of the vertical shear cracks along the sides of the wheel path. From these photos, it is clear that the transverse crack developed because of delamination between the surface and binder courses. The vertical shear cracks were then a result of the delaminated zone being shoved forward in the direction of the wheel path. Examination of the rut depth versus position along the wheel path (Figure 6.1.4) suggests that the cracking seen in this section did not effect the rutting behavior until sometime after 25,000 load passes, which corresponds to the first observation of the crack at 44,000 wheel passes. For wheel pass 52,270, a noticeable increase in rut depth around a position of 2 m is seen, which corresponds to the position of the crack.



Figure 6.2.7 Transverse cracking in test section CRREL3 (geosynthetic A).

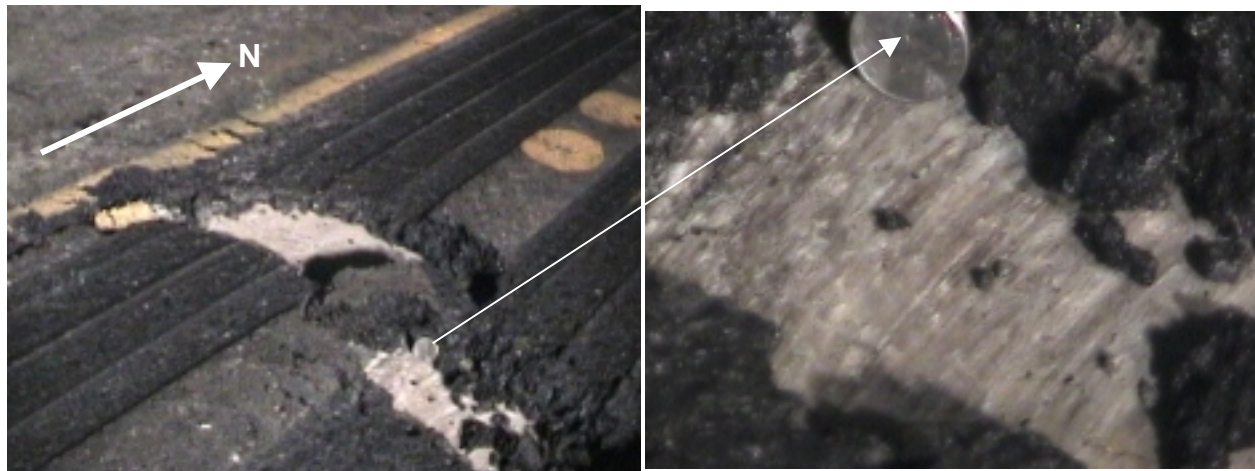


Figure 6.2.8 Close-up photos of transverse cracking in test section CRREL3 (geosynthetic A).

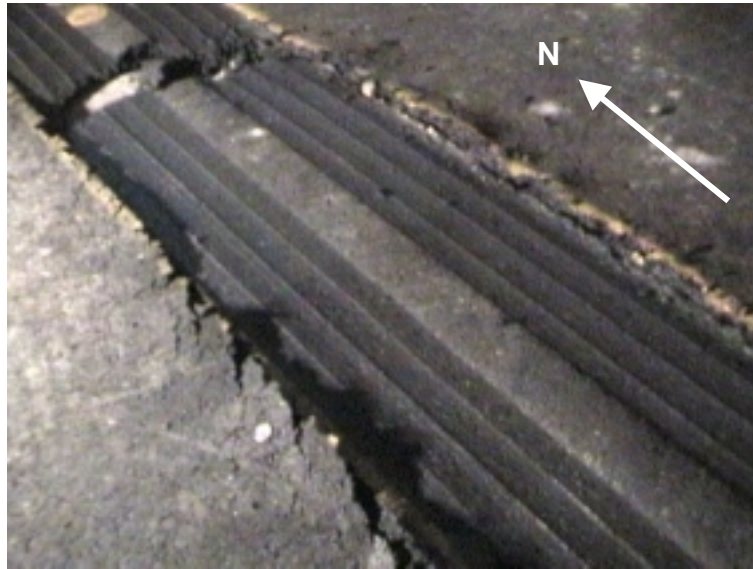


Figure 6.2.9 Vertical shear cracking in test section CRREL3 (geosynthetic A).

No visible cracking was observed in test section CRREL4. The predominant failure mode in these sections was one of rutting where rutting was seen to increase from North to South in the direction of the wheel path. Figure 6.2.10 shows a photo of the rut developed in this test section.

Grain size distribution tests on the aggregate after loading was completed and reported in Figures 5.2.2-5.2.5 showed little differences from top to bottom of the aggregate layer and between sections, indicating that separation and filtration problems were not encountered in any of the sections. Figure 6.2.11 shows a typical loaded cross section after excavation in an uncracked area where a distinct change from the subgrade to the aggregate is seen.

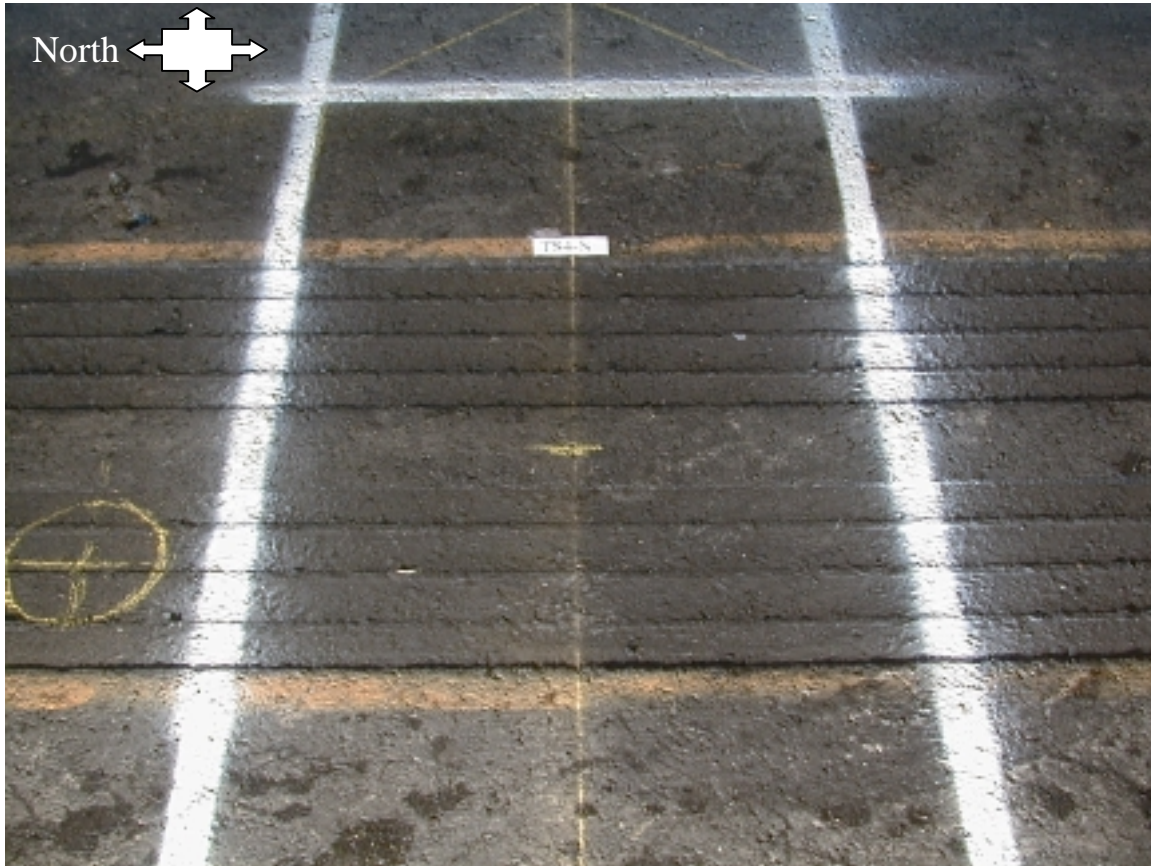


Figure 6.2.10 Rutting in section CRREL4 (geosynthetic H).



Figure 6.2.11 Deformed cross section in section CRREL1 (control).

In summary, rutting appeared to be the controlling failure mode over the majority of the loading history for all the sections. Two sections (CRREL1, control, and CRREL3, geosynthetic A) developed asphalt concrete cracking failures towards the end of the pavement loading and were initiated by delamination between the surface and binder courses. Extensive forensic testing in these two distress areas did not reveal any abnormalities in the underlying materials that would explain the distress observed. Paving occurred in November when the outside temperature was 10°C. The temperature inside the test facility during paving was 13°C. Rapid cooling of the in-place binder course and cooling of asphalt batches towards the end of the paving hopper is the most likely reason for the problems with delamination seen in these two sections. Figure 6.2.12 shows a close-up photo of a cross sectional cut through the asphalt concrete where the lamination between the surface and binder courses is apparent.



Figure 6.2.12 Cross section through CRREL asphalt concrete.

Forensic testing work conducted through trenches in the north and south ends of the sections did not reveal any significant trends in material properties that would help explain the increase in rutting from north to south in sections CRREL3 and CRREL4 and to a minor extent in CRREL1. This work occurred several months after loading was completed, by which time

pore pressures may have equilibrated between sections. Work with this same subgrade in the GTX test sections has shown that pore pressure generation can be significant and has a dramatic influence of pavement response. Since test section CRREL 3 was loaded 4 days following the completion of loading of CRREL1, it is possible that loading at the north end of section CRREL1 induced pore pressures under the south end of CRREL3 and that these induced pore pressures gradually diminished as the north end of CRREL3 was approached. Since section CRREL4 was loaded 9 days following the completion of CRREL2, the same argument would apply to explain the increased rutting from north to south in CRREL4. This argument would also imply that since sections CRREL1 and CRREL3 were loaded before CRREL2 and CRREL4, pore pressures induced under CRREL 2 and 4 by the loading of CRREL1 and 3 would have negatively influenced pavement response in CRREL2 and 4. Time between completion of CRREL1 and start of loading of CRREL2 was 39 days, while 52 days was needed between CRREL3 and CRREL4. Since pore pressure sensors were not included in the testing program, direct evidence to support the above arguments is lacking.

6.3 Dynamic Response Behavior

6.3.1 Dynamic Stress Response

Stress and strain instrumentation allows for the single wheel pass dynamic response of the test sections to be examined. Instrumentation from the stress cells contained in the base aggregate and subgrade layers is first examined. Stress cells were placed in the base aggregate of only the first test section (CRREL1, control). Three stress cells were placed directly beneath the wheel travel path to measure stress in the vertical, transverse and longitudinal directions. The dynamic response of the cells for one wheel pass at the 2500 pass level are shown in Figures 6.3.1-6.3.3. The transverse and longitudinal measures show a relatively complex response where the stress changes from when the wheel is approaching to when the wheel is directly on top of the sensor and then as the wheel departs from the sensor location.

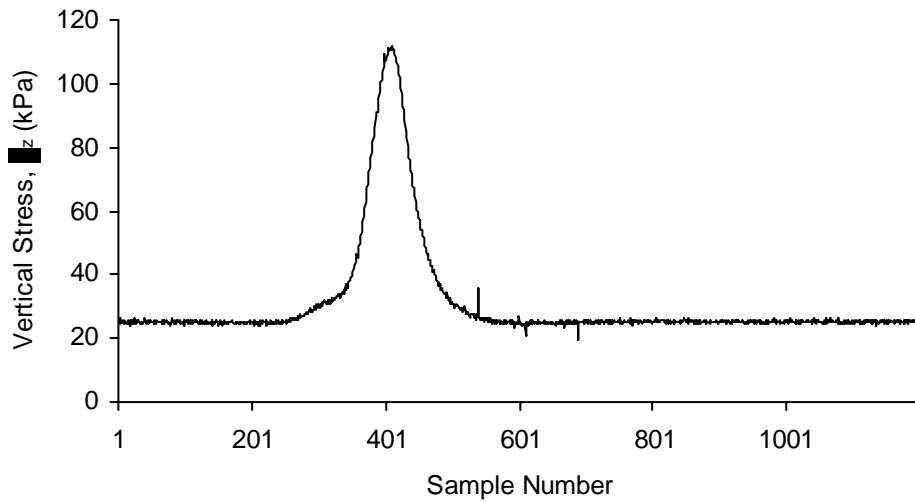


Figure 6.3.1 Vertical stress dynamic response of aggregate at $x=8\text{m}$, $y=4.77\text{m}$, $z=0.293\text{m}$.

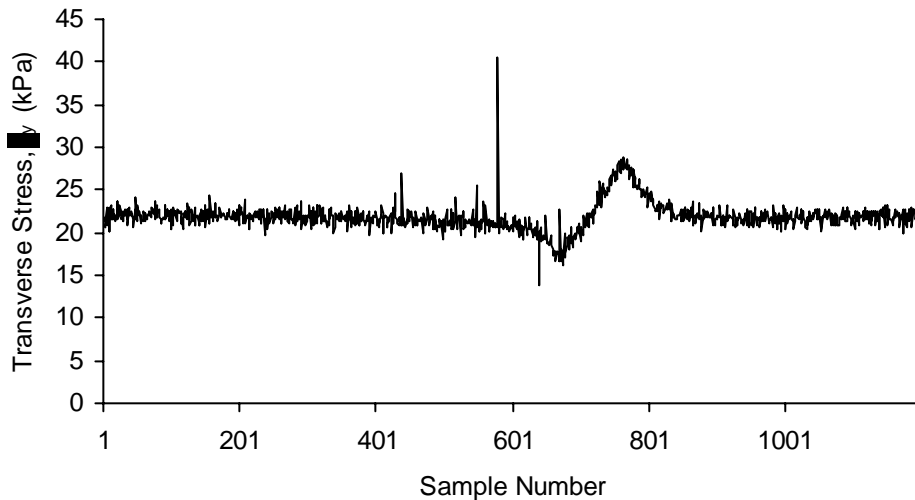


Figure 6.3.2 Transverse stress dynamic response of aggregate at $x=5.25\text{m}$, $y=4.77\text{m}$, $z=0.18\text{m}$.

For each pass level, 25 dynamic stress responses were measured for each stress sensor for 25 different wheel passes. Dynamic response for each wheel pass was computed as the maximum stress response minus the stress value at the end of the sampling period when the wheel was well away from the sensor. Values were then averaged for all 25 measurements for each pass level. Figure 6.3.4 shows the measures of dynamic stress for each of the three sensors. Values are seen to increase modestly with increasing wheel pass level.

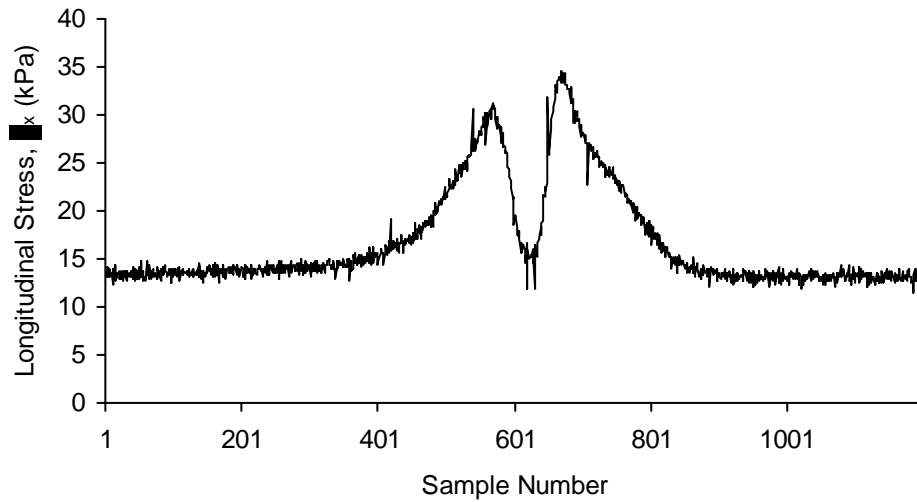


Figure 6.3.3 Longitudinal stress dynamic response of aggregate at $x=6.1\text{m}$, $y=4.77\text{m}$, $z=0.146\text{m}$.

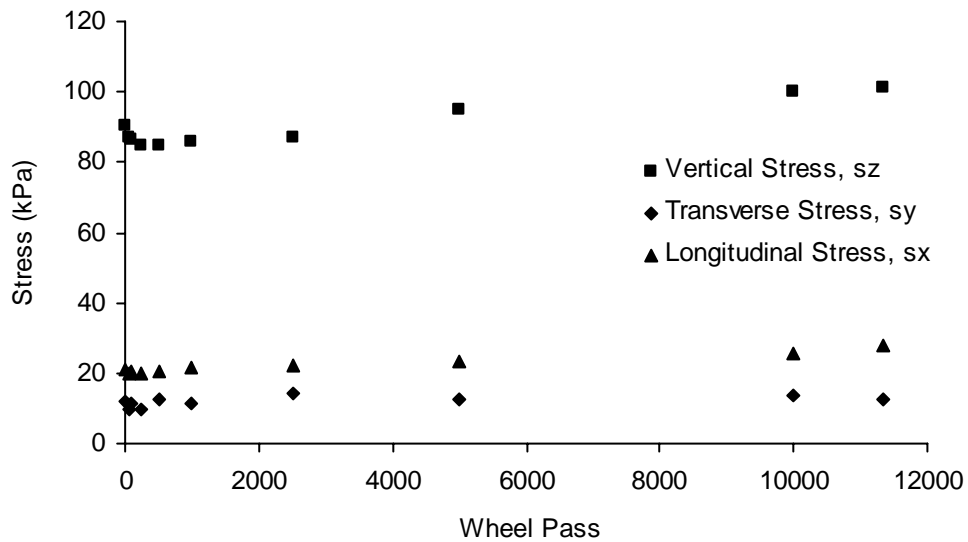


Figure 6.3.4 Dynamic stress response of CRREL aggregate.

Five stress cells were placed in the subgrade layer of each test section to measure vertical stress. The locations of the sensors were common between the sections with respect to depth and distance from the wheel travel path. Table 6.3.1 gives the general locations of each sensor. Sensors 1 and 2 served as duplicate readings and were offset by 0.15 m along the length of the wheel path. Figures 6.3.5-6.3.7 show dynamic stress values as a function of wheel pass for

sensors 1, 2 and 3. The data from the first sensor indicates higher vertical stress at the top of the subgrade in sections CRREL2 and 4. This trend does not correspond to the rutting performance observed in the sections. The majority of the sensors show an initial value of 40 kPa increasing to 55 kPa towards the end of the test. For the deeper sensor (#3), section CRREL4 shows the highest stress, which also does not correspond to observed rutting behavior. Sensor 3 for section CRREL2 was inoperable.

Figures 6.3.8 and 6.3.9 show dynamic vertical stress versus wheel pass for sensors 4 and 5 located at the top of the subgrade but at increasing lateral distance from the wheel travel path. Figure 6.3.10 shows a plot of vertical stress versus lateral distance for the four sensors located in the top of the subgrade. The data shows that greater load distribution is achieved in the reinforced sections as compared to section CRREL1, however significant differences between the control sections do not exist. Similar trends are seen for other wheel pass levels.

Table 6.3.1 Locations of stress sensors in CRREL subgrade.

Sensor	Lateral offset from wheel travel path (m)	Vertical distance from pavement surface (m)
1	0.0	0.46
2	0.0	0.46
3	0.0	0.61
4	0.15	0.46
5	0.35	0.46

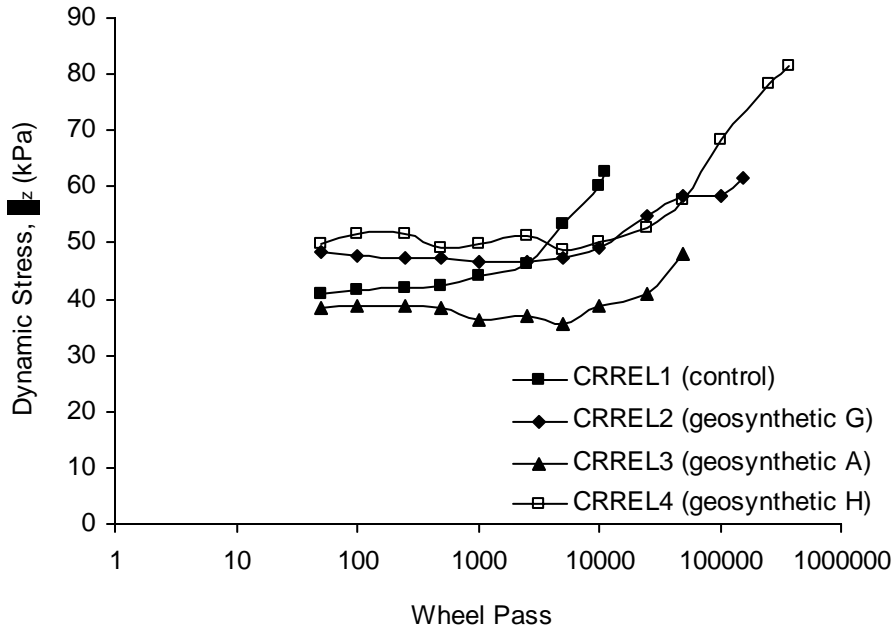


Figure 6.3.5 Dynamic stress response vs. wheel pass for stress sensor 1.

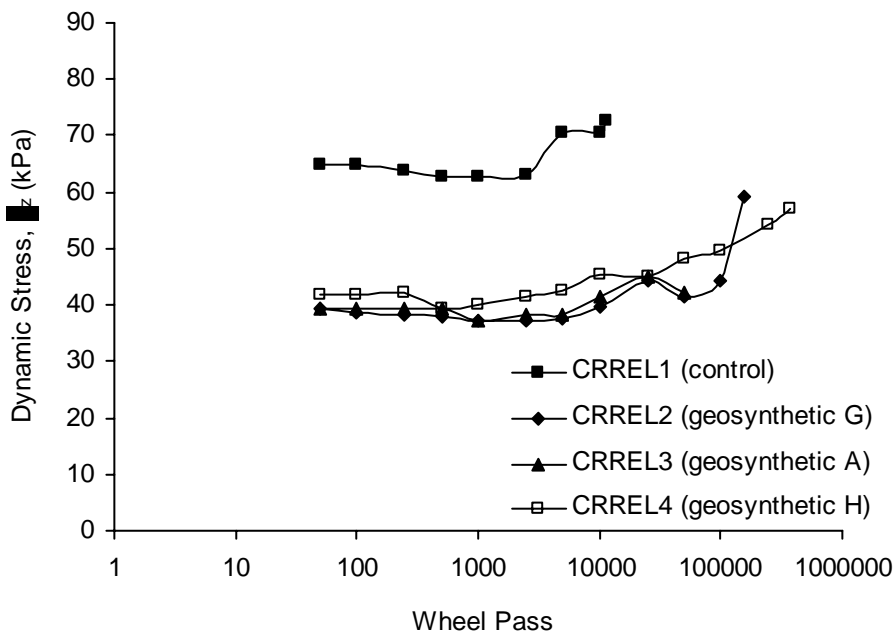


Figure 6.3.6 Dynamic stress response vs. wheel pass for stress sensor 2.

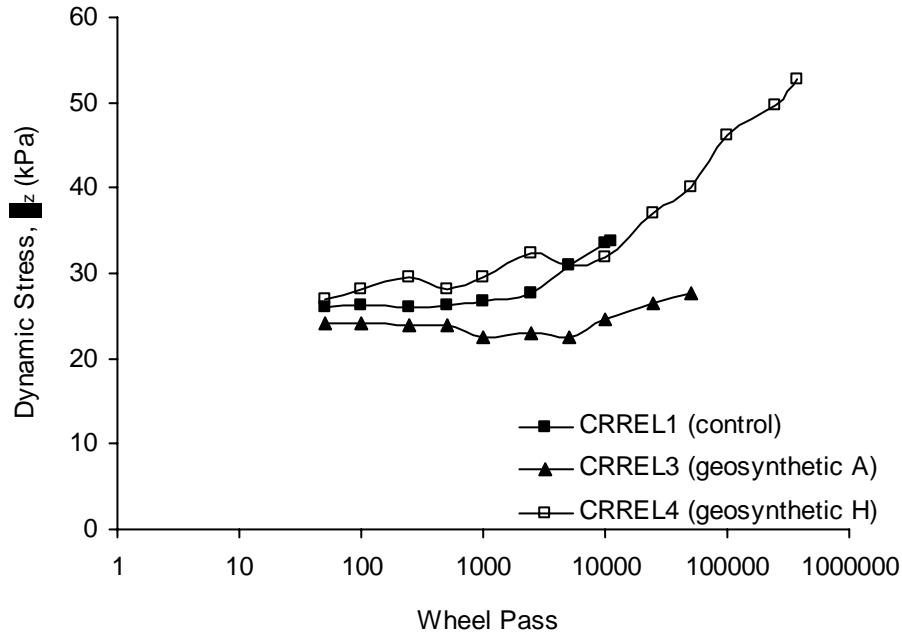


Figure 6.3.7 Dynamic stress response vs. wheel pass for stress sensor 3.

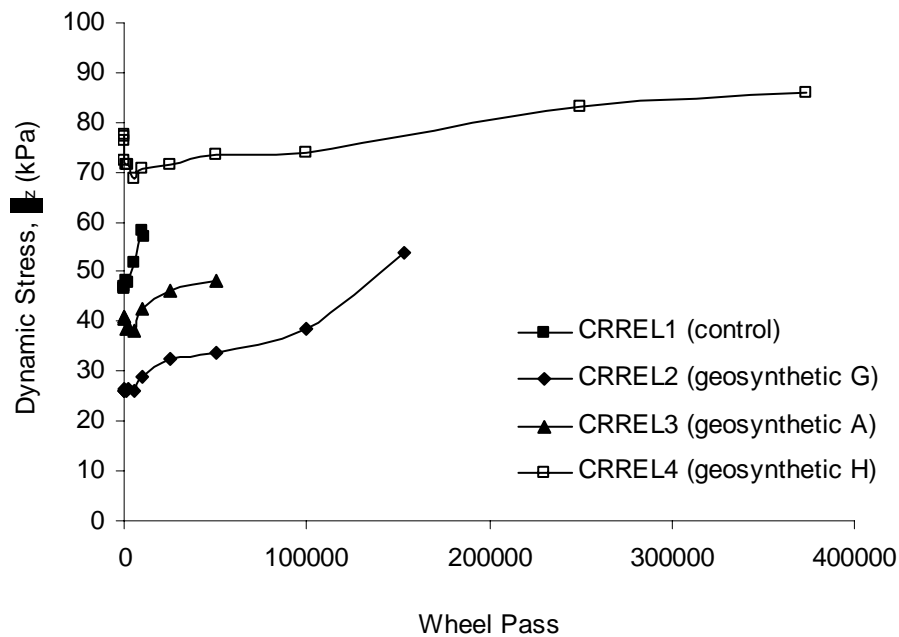


Figure 6.3.8 Dynamic stress response vs. wheel pass for stress sensor 4.

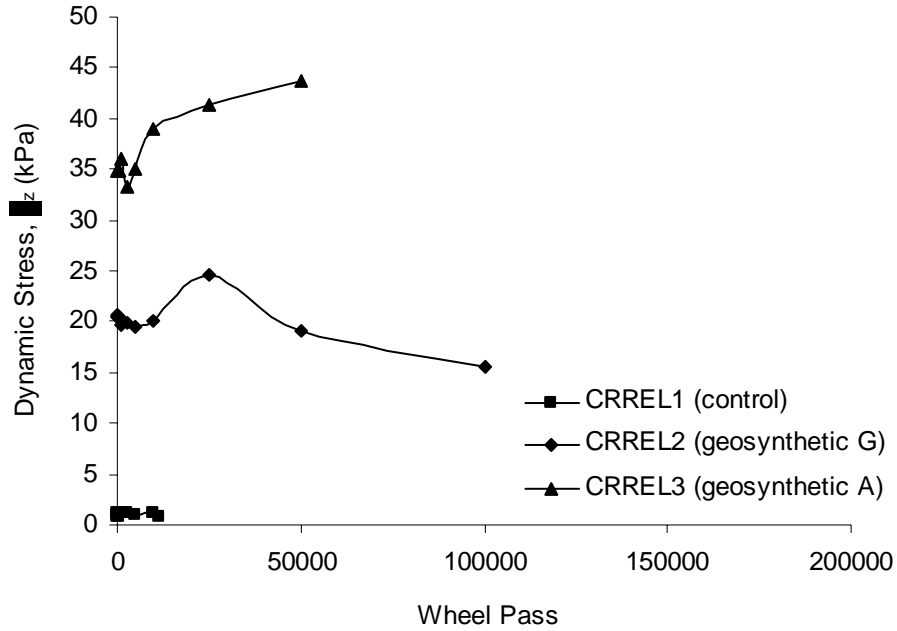


Figure 6.3.9 Dynamic stress response vs. wheel pass for stress sensor 5.

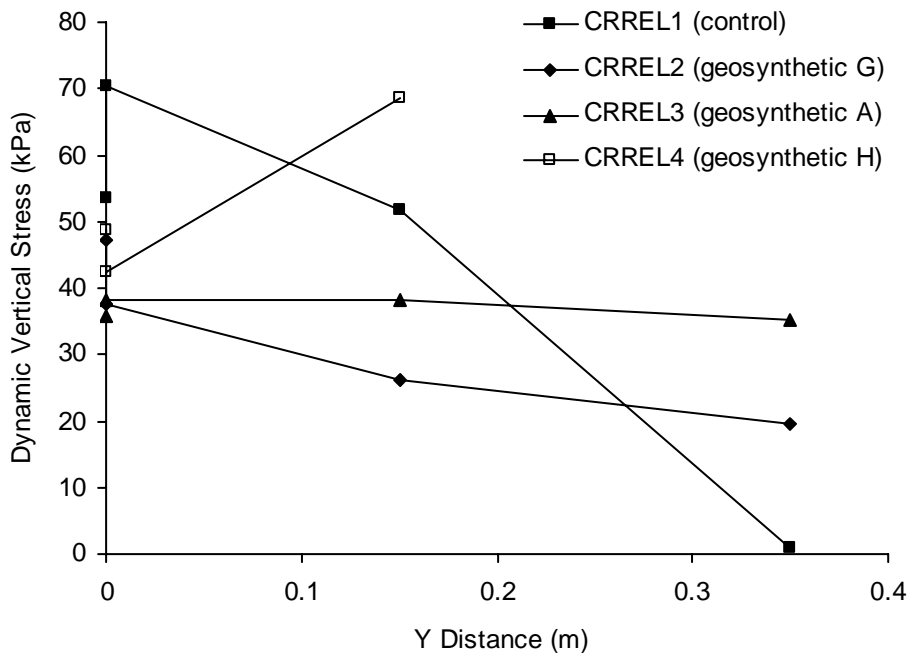


Figure 6.3.10 Dynamic stress response vs. lateral distance.

6.3.2 Dynamic Strain Response

Dynamic strain response of the test sections is examined by use of data from the strain coils. Figure 6.3.11 shows the full vertical strain response from a passing wheel load for test sections CRREL1 and CRREL4 for a strain measurement directly under the wheel path and at a depth of 0.505 m and for wheel pass number 2500, which is the vertical strain measurement location closest to the top of the subgrade. Positive strain is taken as compression. The subgrade is seen to compress with the response being essentially recoverable. A 40 % reduction in vertical strain at the top of the subgrade is seen between sections CRREL1 and CRREL4. Figure 6.3.12 shows the full transverse strain response for wheel pass number 2500 for a location at a depth of 0.33 m (bottom of base) and offset from the wheel travel path by 0.075 m. The response is one of extensional (tensile) strain as the wheel passes with the response being essentially recoverable. The maximum tensile strain is reduced by 60 % in section CRREL4 as compared to CRREL1. This pattern of response is similar to the radial response behavior seen at the bottom of the base from test sections cyclically loaded with a stationary circular plate (Perkins, 1999). Strain in the longitudinal direction, as shown in Figure 6.3.13, shows a more complicated response where extensional strains are seen as the wheel approaches but larger compressive strains then develop as the wheel is over top of the measurement point and then turning back to extension as the wheel passes from the measurement point. A similar response was seen in test sections described by Janoo et al. (1999). The peak values of extension and compression are significantly lower in test section CRREL4 as compared to CRREL1.

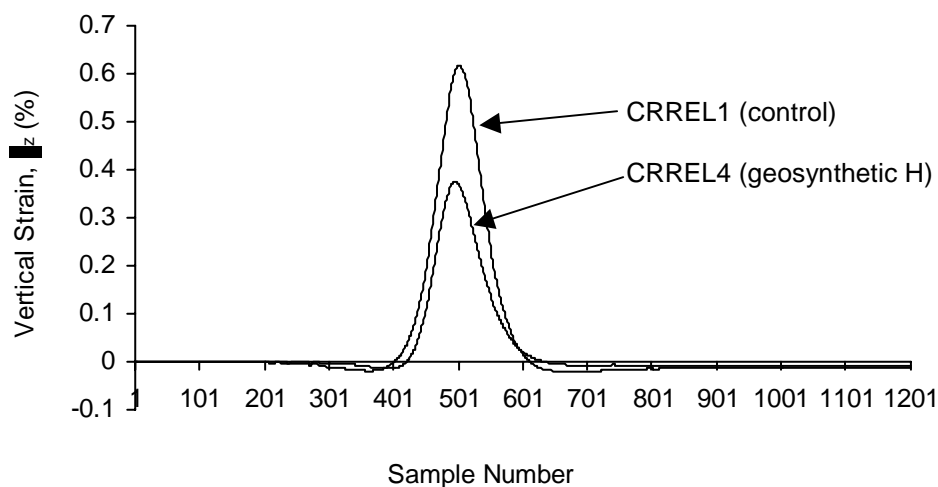


Figure 6.3.11 Dynamic vertical strain response vs. sample number for top of subgrade.

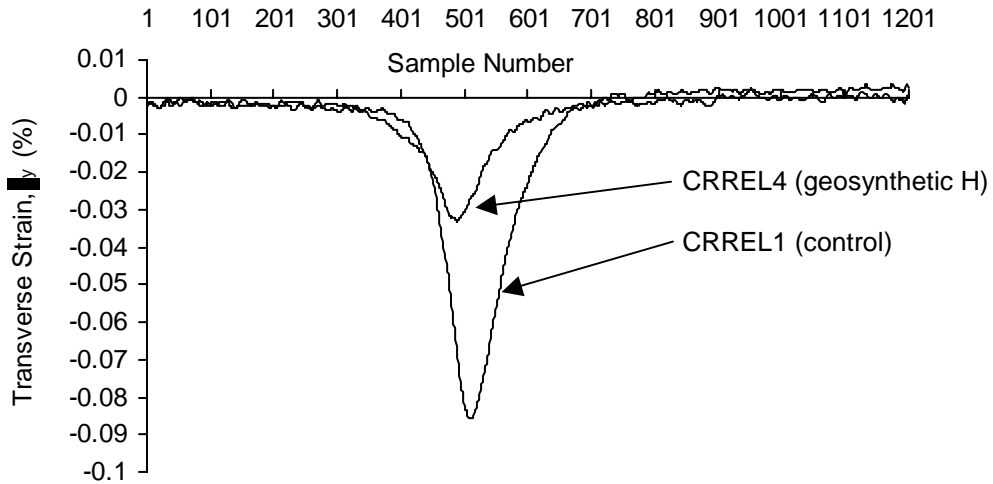


Figure 6.3.12 Dynamic transverse strain response vs. sample number for bottom of base.

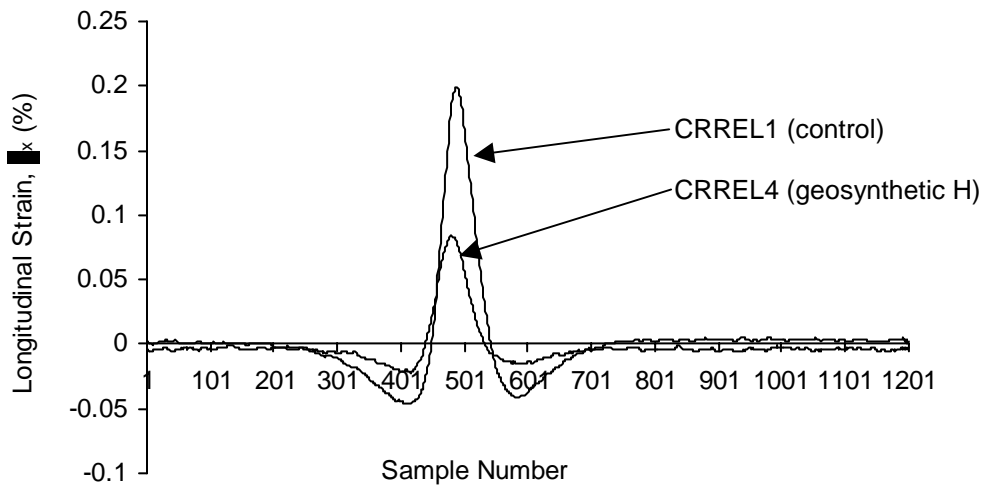


Figure 6.3.13 Dynamic longitudinal strain response vs. sample number for bottom of base.

The dynamic (recoverable) strain was defined for each wheel pass as the peak response value minus the value once the wheel was well past the measurement point. Since 25 wheel passes were necessary to measure the response of all strain coil pairs, not all dynamic strain measures correspond to exactly the same wheel pass level. The maximum difference between the actual wheel pass number for any two measurements is 25 wheel passes. While the dynamic strain response, as illustrated below, changes with wheel pass number, the differences appear to be minor over 25 wheel passes.

Figure 6.3.14 shows the dynamic vertical strain directly beneath the wheel path at a depth of 0.38 m. At this location, the strain coil pair sandwiched 0.045 m of base aggregate and 0.055 m of subgrade. The response of the sections generally follows the order of performance of the sections. Figure 6.3.15 shows the dynamic vertical strain beneath the wheel path at a depth of 0.505 m, which is the next location below the measurement point shown in Figure 6.3.14 and encompasses only subgrade. The reinforced sections are clearly set off from the unreinforced section, however differences between the reinforced section are indistinguishable up to 5000 wheel passes. Figure 6.3.16 shows the dynamic transverse strain at a depth of 0.38 m (bottom of base) and offset from the wheel travel path by 0.075 m. The reduction of extensional strains at the bottom of the base from the unreinforced section to the reinforced sections corresponds to test section performance.

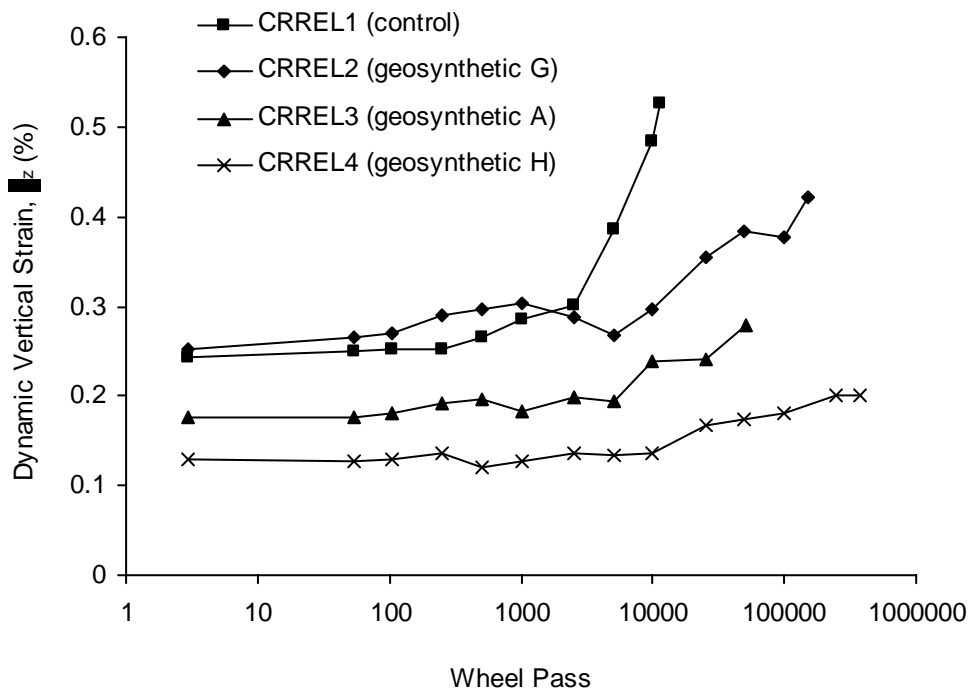


Figure 6.3.14 Dynamic vertical strain vs. wheel pass for base/subgrade interlayer.

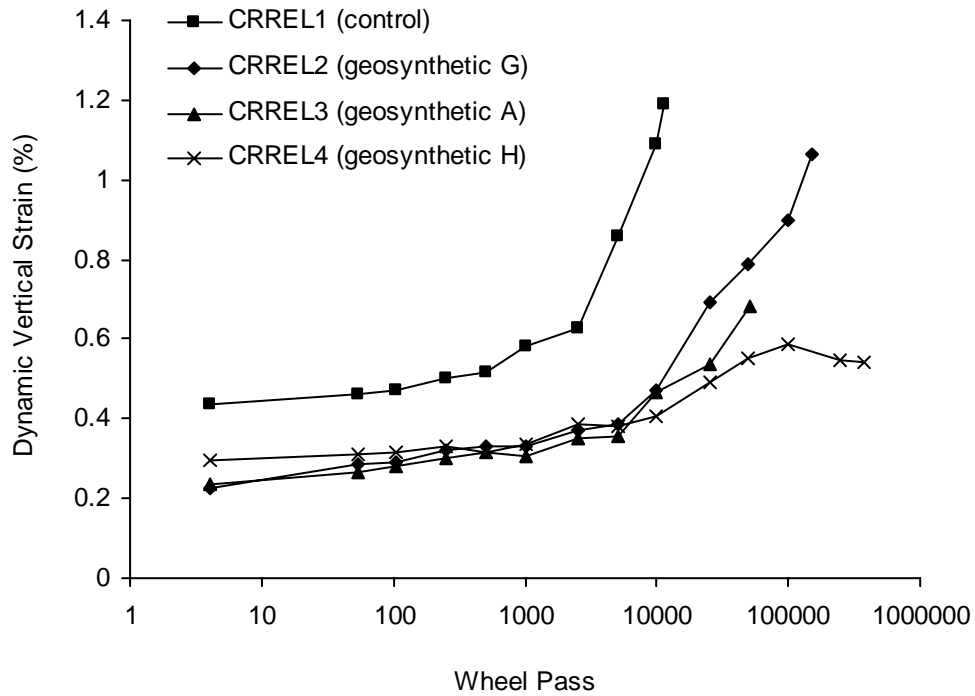


Figure 6.3.15 Dynamic vertical strain vs. wheel pass for top of subgrade.

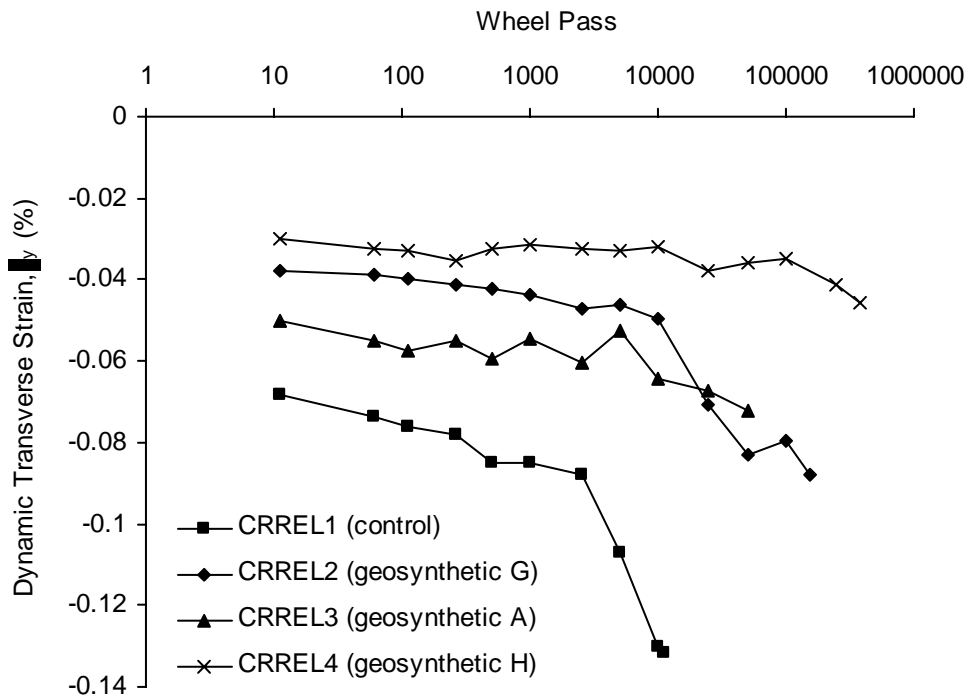


Figure 6.3.16 Dynamic transverse strain vs. wheel pass for bottom of base.

Figure 6.3.17 shows dynamic vertical strain directly under the wheel path plotted against depth for wheel pass level 2500. The response shows a decrease in strain with depth through the base with a sudden increase at the top of the subgrade which rapidly decreases with depth. The unreinforced section shows a greater strain at all depths, however the differences between the reinforced sections is apparent but not significant. Figure 6.3.18 shows dynamic transverse strain at a depth of 0.33 m (bottom of base) plotted against transverse distance from the wheel path centerline for wheel pass level 2500. As with the results shown in Figure 6.3.16, a correspondence between strain behavior and test section performance is seen in these results. Figure 6.3.19 shows dynamic transverse strain versus depth at wheel pass 2500 for a point 0.075 m from the wheel path centerline. The effect of the reinforcement is seen to influence transverse strain values throughout the cross-section of the pavement.

In summary, dynamic stress and strain response measures tend to show a marked difference between reinforced and unreinforced sections. The mechanisms of reinforcement are similar to those seen in smaller scale test sections cyclically loaded with a stationary plate (Perkins 1999). Differences between the reinforced sections are notable and tend to correspond to overall rutting behavior, but are not significant.

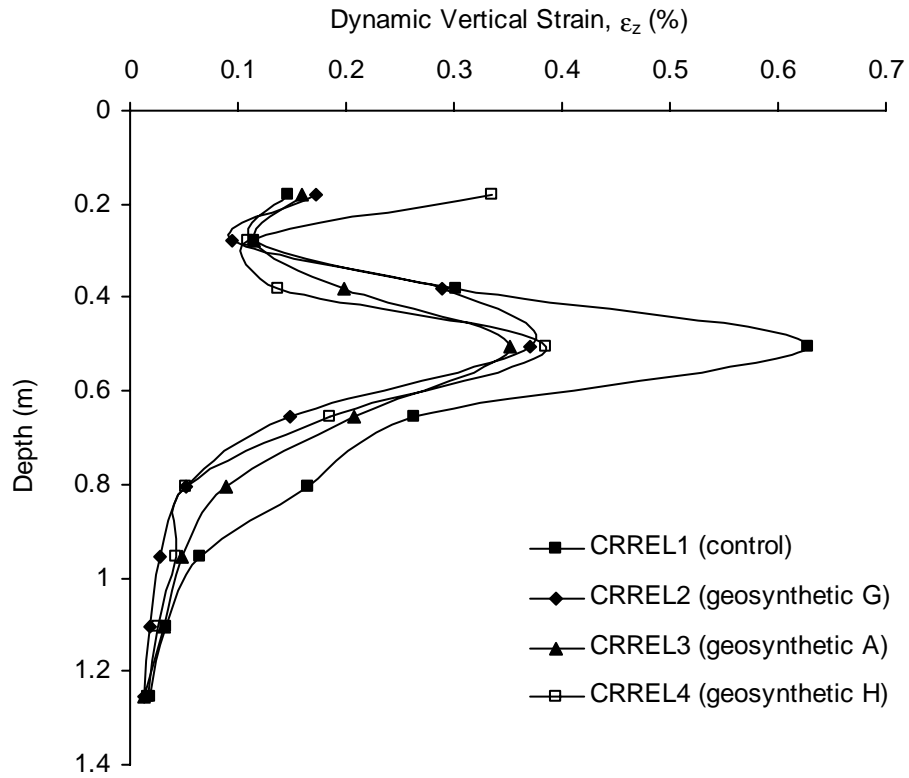


Figure 6.3.17 Dynamic vertical strain vs. depth at wheel pass 2500.

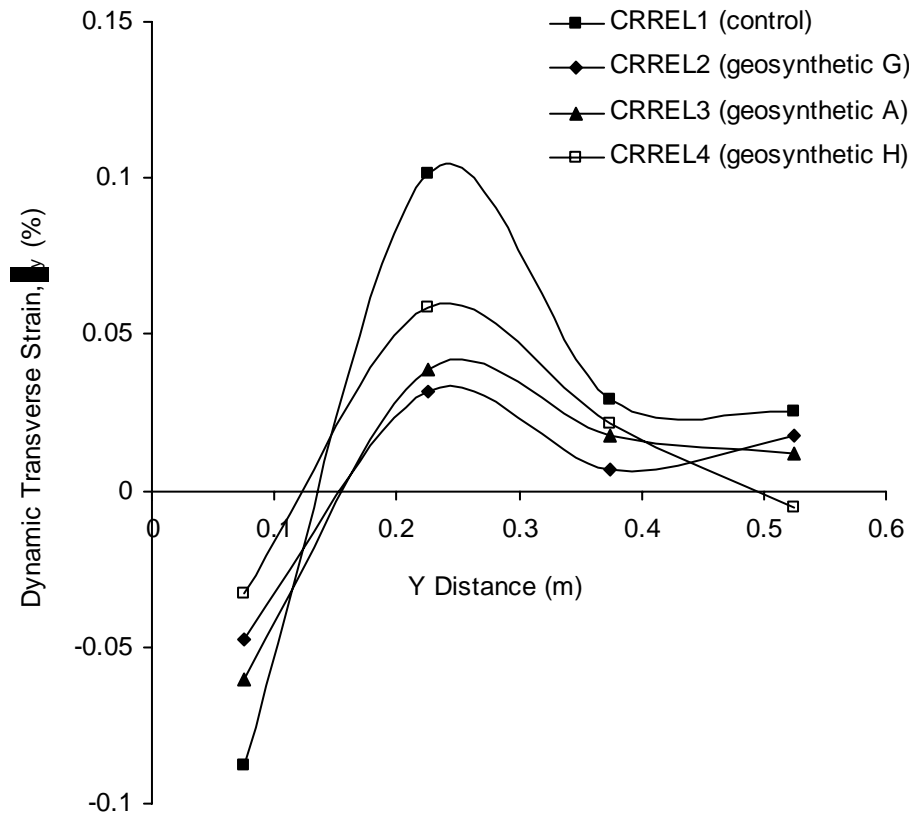


Figure 6.3.18 Dynamic transverse strain vs. transverse distance at the bottom of the base at wheel pass 2500.

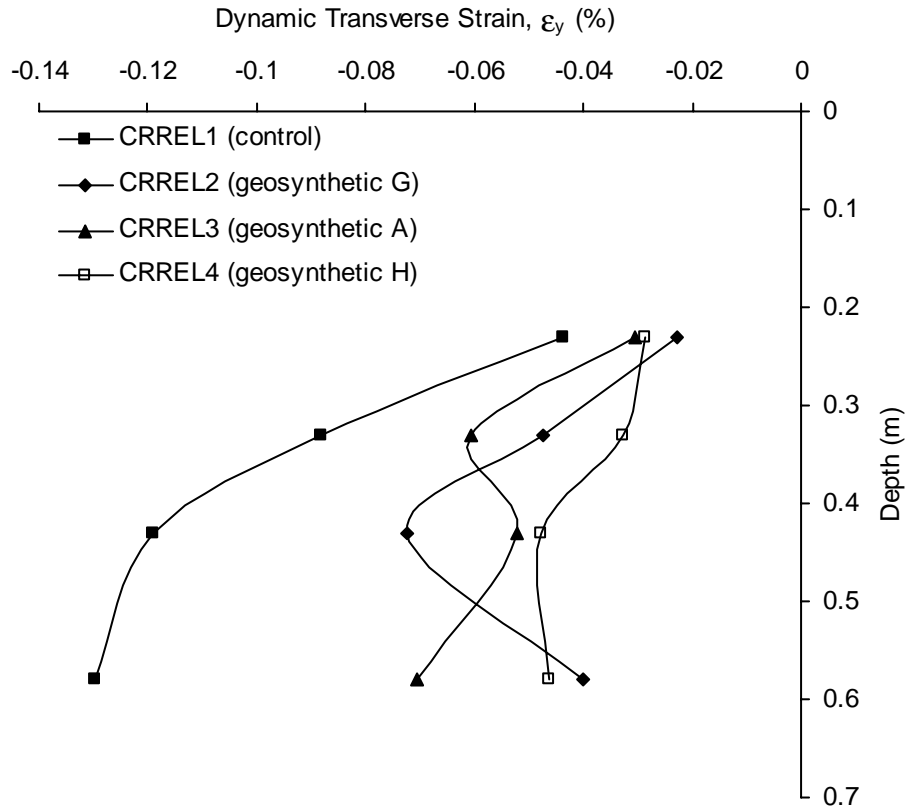


Figure 6.3.19 Dynamic transverse strain vs. depth at wheel pass 2500.

6.4 Permanent Deformation/Strain Behavior

Figures 6.4.1-6.4.3 show the development of permanent vertical strain with wheel pass directly under the wheel travel path for depths of 0.23, 0.38 and 0.505 m. All three positions show a relatively rapid strain development in the unreinforced section along with a slower rate of development in the reinforced sections. Figures 6.4.4 and 6.4.5 show permanent vertical strain plotted against depth below the wheel path centerline for wheel pass numbers 2500 and 10,000. Figures 6.4.6 and 6.4.7 show the same responses for a duplicate set of sensors.

Like dynamic response, permanent strain behavior shows a marked difference between reinforced and unreinforced sections. The differences between reinforced sections tends to be more pronounced than that seen for the dynamic stress/strain response.

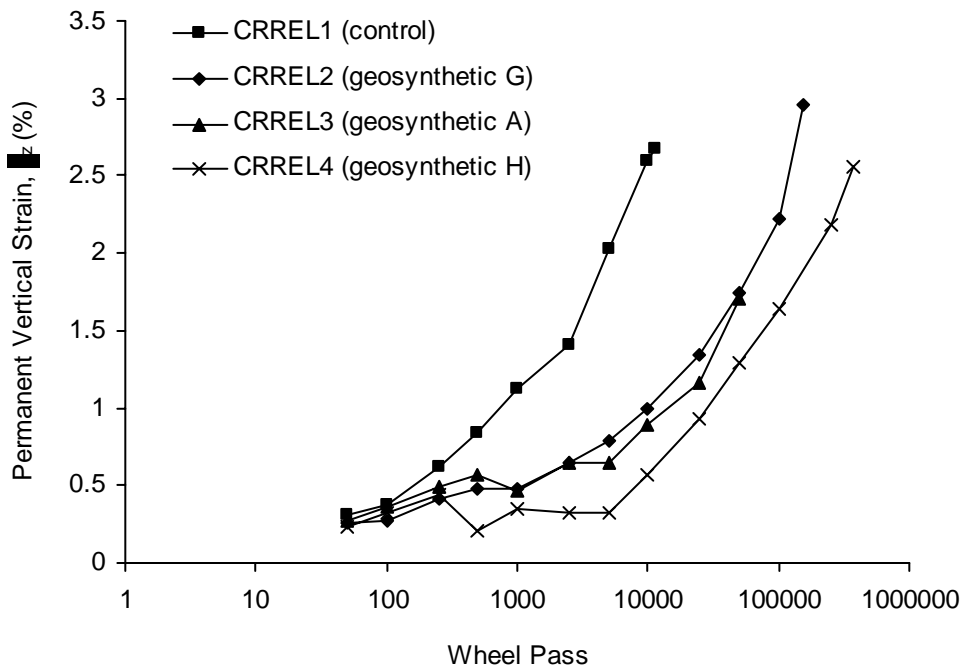


Figure 6.4.1 Permanent vertical strain vs. wheel pass for middle of base.

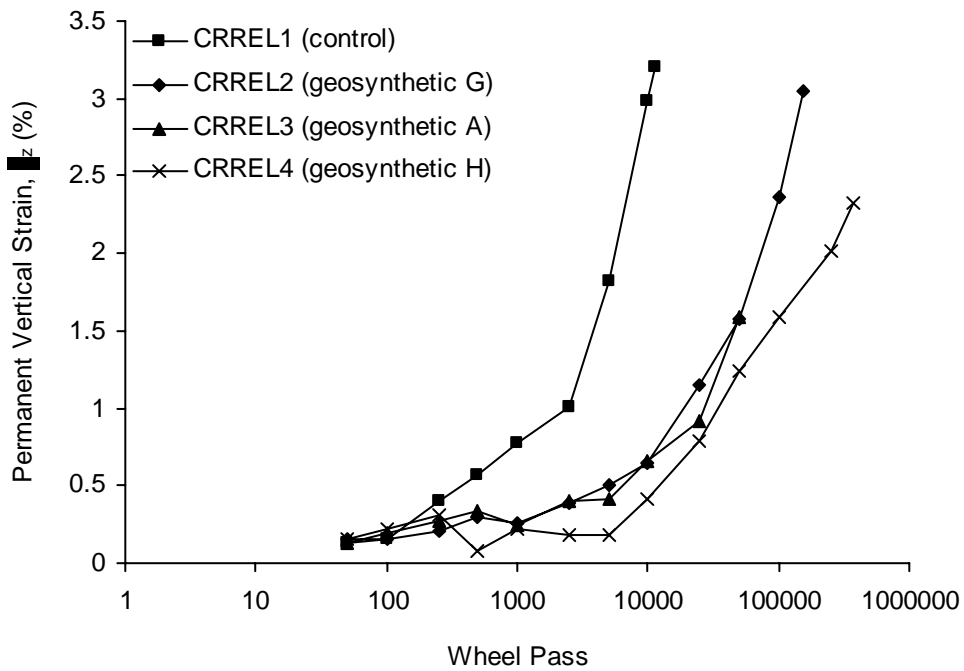


Figure 6.4.2 Permanent vertical strain vs. wheel pass for base/subgrade interlayer.

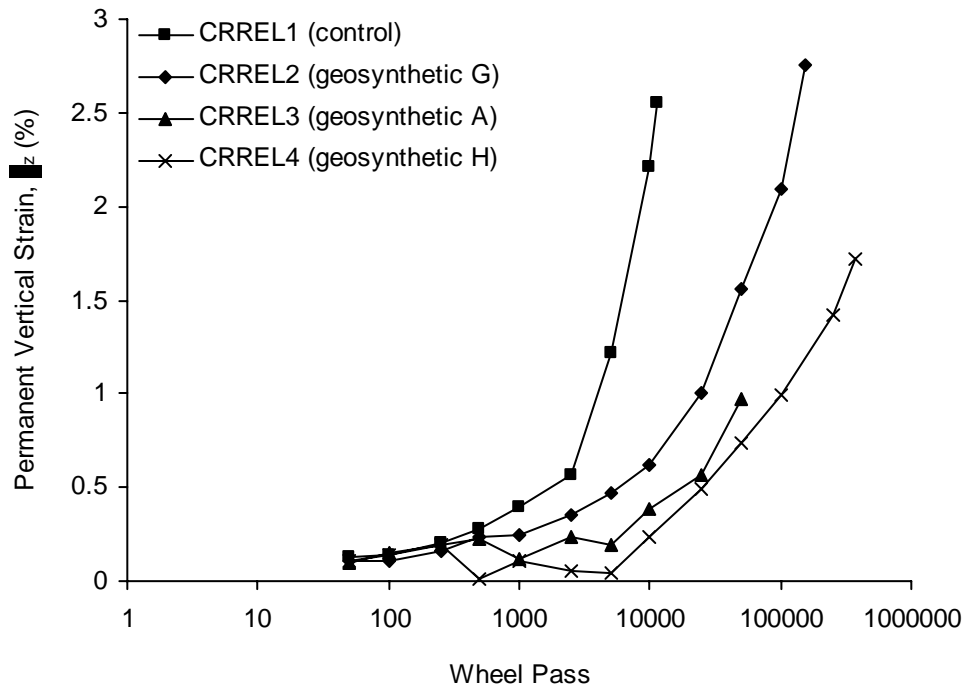


Figure 6.4.3 Permanent vertical strain vs. wheel pass for top of subgrade.

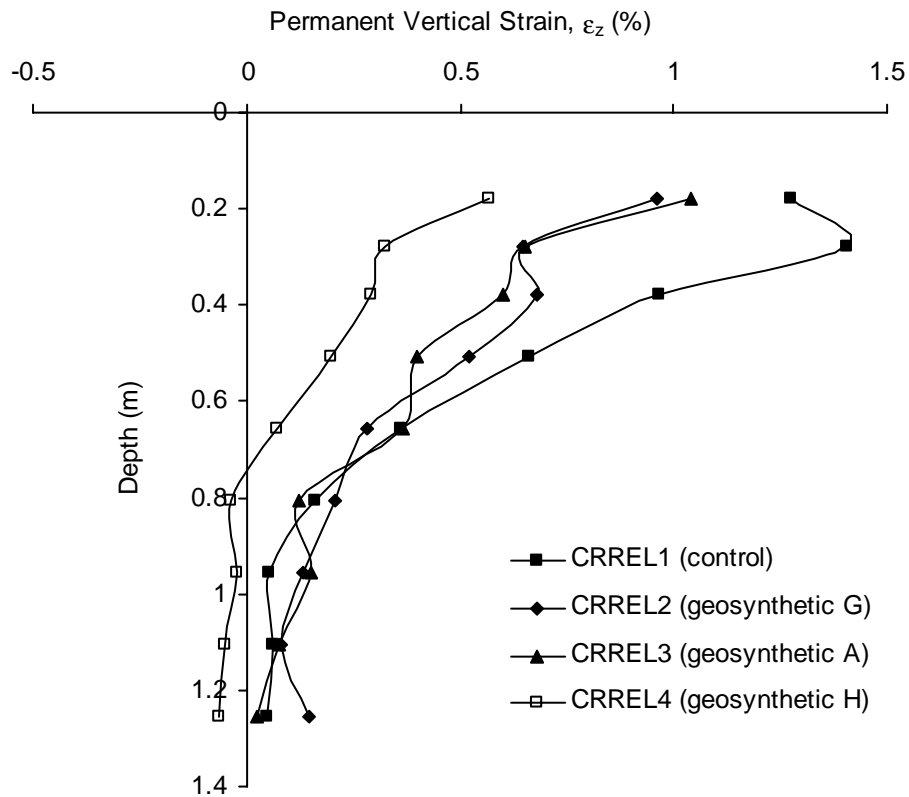


Figure 6.4.4 Permanent vertical strain vs. depth at wheel pass 2500.

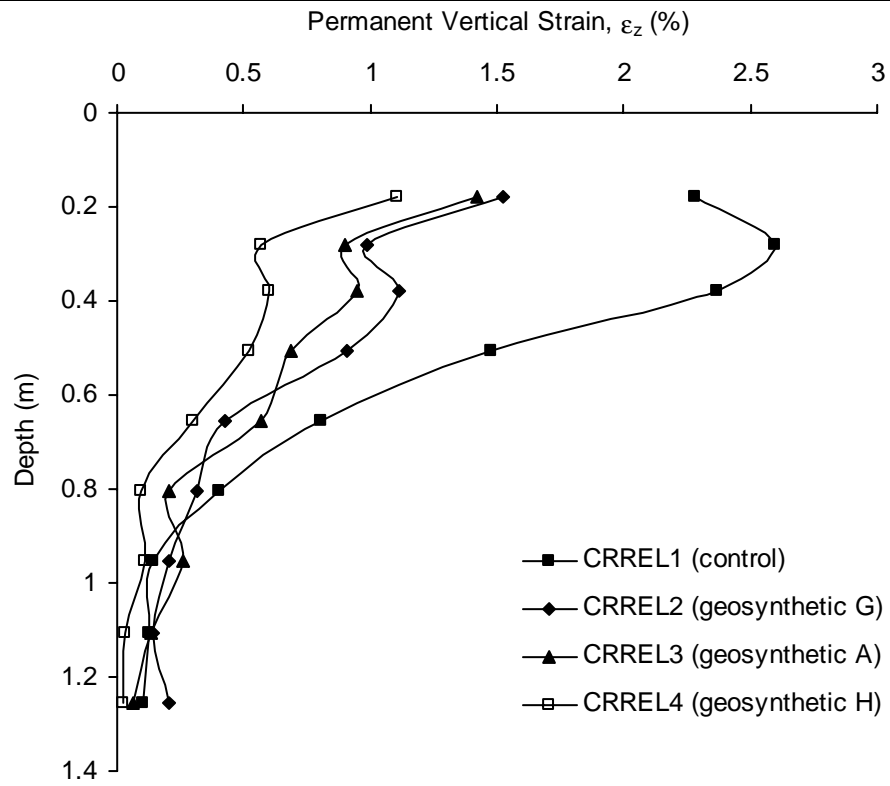


Figure 6.4.5 Permanent vertical strain vs. depth at wheel pass 10,000.

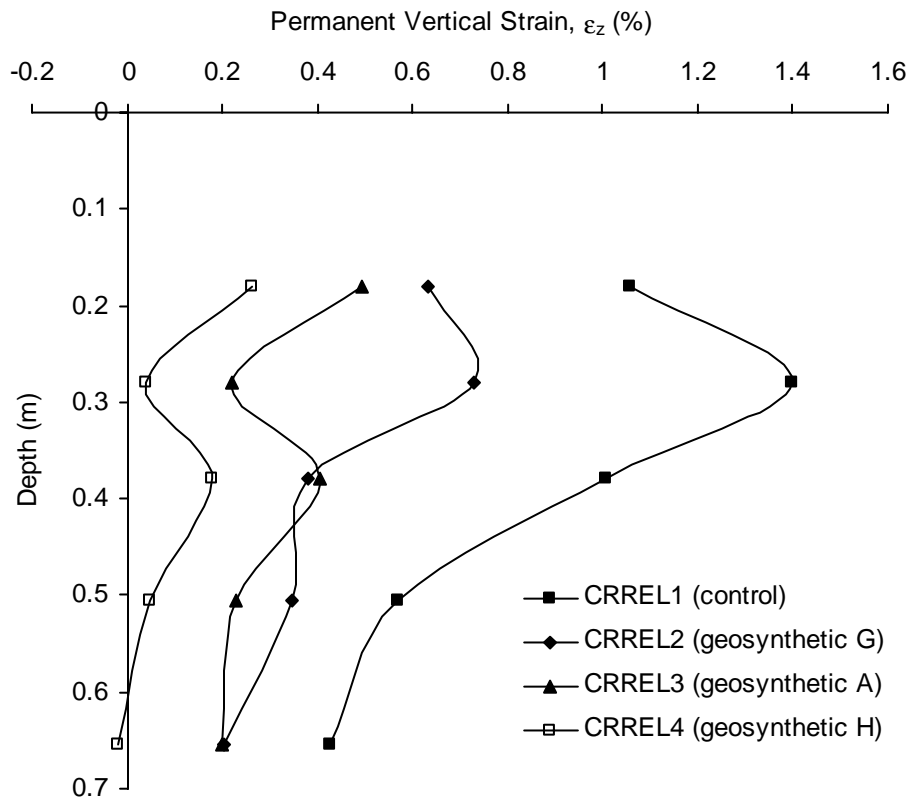


Figure 6.4.6 Permanent vertical strain vs. depth at wheel pass 2500, duplicate sensor set.

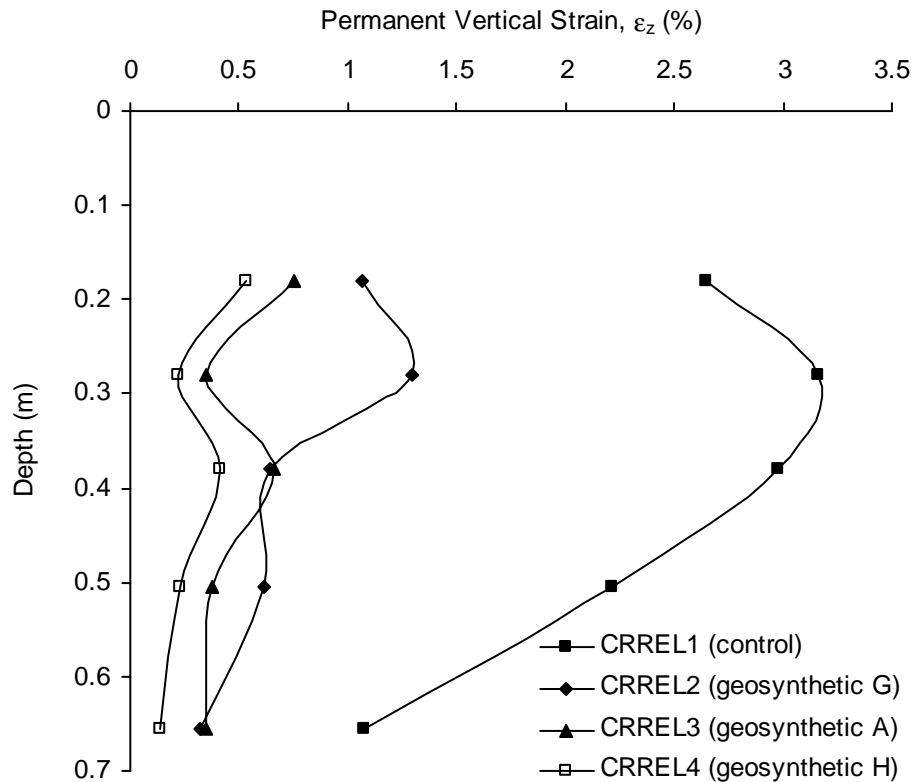


Figure 6.4.7 Permanent vertical strain vs. depth at wheel pass 10,000, duplicate sensor set.

7.0 RESULTS: MSU TEST BOX

7.1 Thin (T) Sections

The test sections labeled MSU T1 – MSU T7 were constructed to evaluate reinforcement benefit in terms of base course thickness reduction. Previous test sections constructed with the same materials used in the “T” sections (Perkins 1999) used the same base course thickness of 300 mm for both reinforced and unreinforced sections such that the extension of life or Traffic Benefit Ratio was the benefit experimentally defined from the results.

The thicknesses chosen for the three geosynthetic types (A, G and H) were based on the use of TBR values obtained from earlier test sections (Perkins 1999) and the use of the 1993 AASHTO Pavement Design Guide. The TBR values of 8, 17 and 45 for geosynthetics A, G and H for test sections having a nominal thickness of asphalt and base of 75 mm and 300 mm were used directly to define the increase in ESAL’s that the reinforced sections could carry. The 1993 AASHTO Guide was used to define the increase in the base layer structural coefficient needed to see the corresponding increase in ESAL’s for the reinforced sections. This new layer coefficient

was then used to determine the thickness of the reinforced aggregate such that equal life to the unreinforced section was obtained. This corresponded to 200, 175 and 140 mm for sections reinforced with geosynthetics A, G and H, corresponding to a base course reduction (BCR) ratio of 33, 42 and 53 %. Sections constructed with these thicknesses were expected to yield similar rutting behavior to previously constructed unreinforced sections with a base layer thickness of 300 mm (sections MSU1 and MSU2).

Figure 7.1.1 shows the results of rutting behavior for all the T sections. Sections T5 and T7 were repeats using geosynthetic A. Sections T1, T4 and T6 were repeats using geosynthetic G. Sections T2 and T3 were repeats using geosynthetic H. Sections MSU1 and MSU2 were repeats of an unreinforced section. Sections T2 and T3, and MSU1 and MSU2 show excellent repeatability. Sections T5 and T7 show moderate repeatability with the initial deformation response appearing to be the most different. Sections T1, T4 and T6 show the worse repeatability. A data collection problem with section T6 resulted in zero permanent deformation values being recorded for the first 50 load cycles where deformations in these sections ranged from 1 to 6 mm. Shifting the T6 curve upwards by as much as 6 mm would result in a response that was considerably stronger than T1 or T4. The temperature in the test facility during the loading of T6 was relatively low (10°C) whereas the majority of the other sections were between 16 and 20°C. This most likely accounts for the stiffer response seen in section T6 as compared to T1 and T4. The temperature in T5 was also relatively low (8°C), whereas the temperature in the repeat section T7 was more normal.

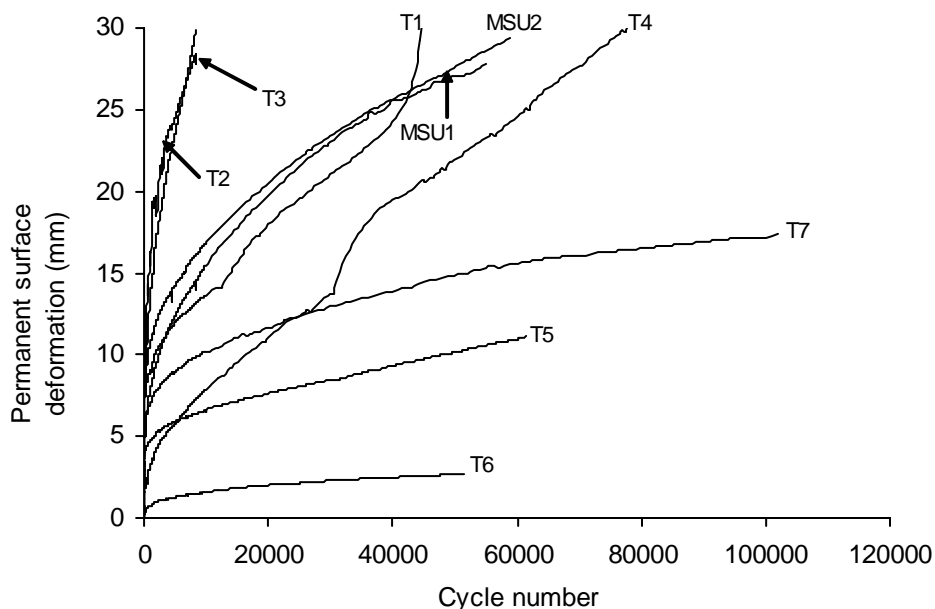


Figure 7.1.1 Permanent surface deformation vs. load cycle for MSU “thin” sections.

While the lack of repeatability of certain T sections makes it difficult to define exact rutting behavior, the trend of the results indicates that the use of the 1993 AASTHO design equations to predict a BCR from a known TBR is conservative with the exception of the BCR used in the T2/T3 sections (i.e. 53 %). The higher rutting behavior of sections T2/T3 as compared to the unreinforced sections may also be an indication of the danger associated with the use of high BCR values that result in a section thinner than 150 mm, which is generally considered the minimum amount of aggregate needed for a flexible pavement.

The design program (Perkins, 2001b) predicts BCR values of 18, 31, and 35 % for the conditions present in T sections with geosynthetics A, G and H. From the results given above, it can be concluded that the predictions of BCR from this design program are conservative for these conditions and products.

Rutting behavior was due to the development of permanent vertical strain within both the base and the subgrade. Figures 7.1.2 and 7.1.3 show permanent vertical strain along the load plate centerline at the bottom of the base and the top of the subgrade. Strain behavior corresponds well to rutting behavior seen in Figure 7.1.1.

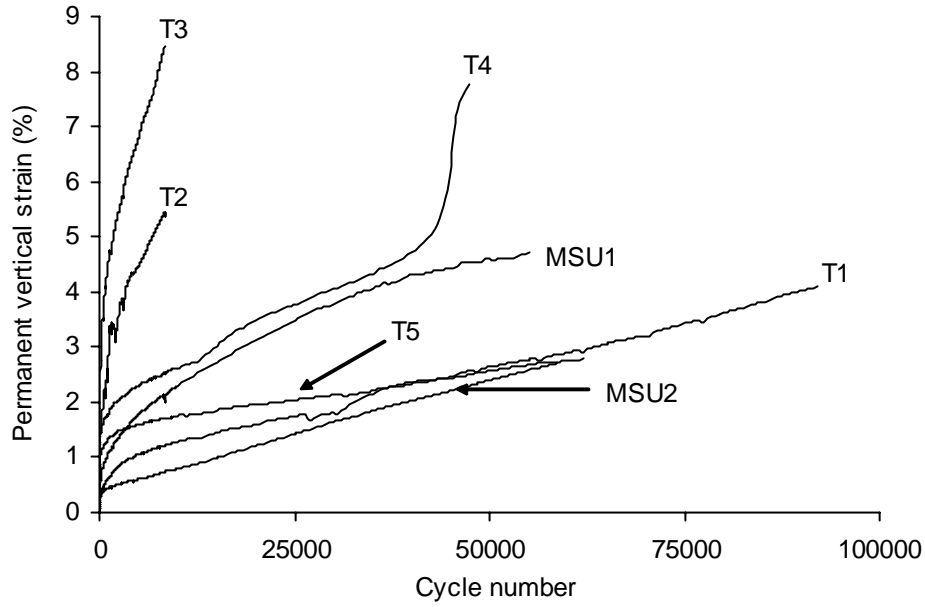


Figure 7.1.2 Permanent vertical strain in the bottom of the base for T sections.

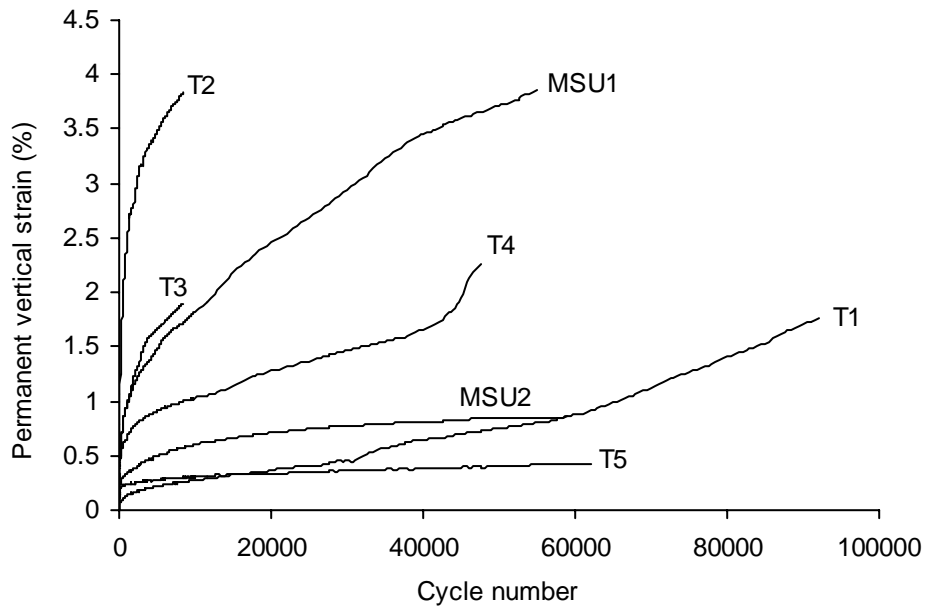


Figure 7.1.3 Permanent vertical strain in the top of the subgrade for T sections.

Figure 7.1.4 shows a plot of dynamic radial strain on the geosynthetic in the machine direction at a radius of 15 mm from the load plate centerline for the test sections having operable strain gauges. Previous test sections reported by Perkins (1999) with 300 mm of base aggregate showed a maximum dynamic strain of 0.4 %. The values of strain seen in the thin sections are 50 % greater than those seen in previously reported sections.

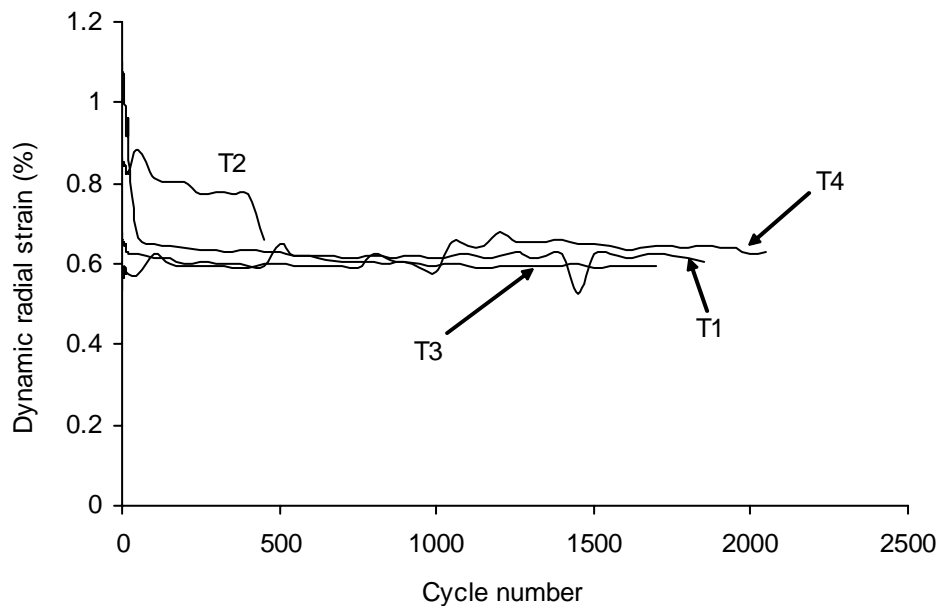


Figure 7.1.4 Dynamic radial strain on the geosynthetics for T sections.

7.2 Rounded (R) Sections

Test sections labeled MSU R1 – MSU R5 were constructed to evaluate the role of geosynthetic-aggregate interaction on reinforcement performance. The aggregate used in these sections was an uncrushed aggregate consisting of pit-run material from a gravel pit located outside of Belgrade, MT. The material in the pit consists of rounded alluvial deposits. The pit-run material was passed over a 38 mm screen.

Figure 7.2.1 shows results of rutting versus load cycle with the results compared back to test sections MSU1 and MSU2. Sections R1 and R3 were repeat unreinforced sections and showed reasonable repeatability. These sections showed an unexpected response of less permanent deformation as compared to sections MSU1 and MSU2 which contained a crushed aggregate. The reinforced sections showed lower permanent deformation with geosynthetic A giving less deformation than geosynthetic G. This is in contrast to earlier findings using a

crushed aggregate for the base. A possible explanation for this result could be a reduction in interface shear modulus and friction coefficient for the geosynthetic G – rounded aggregate combination. The results from the direct shear tests do not, however, support this argument. TBR values at 20 mm of permanent deformation are 11 and 4 for geosynthetic A and G. These numbers are higher for geosynthetic A and lower for geosynthetic G as compared to test sections using a crushed aggregate. A repeat of section R4 was not performed to confirm the results obtained.

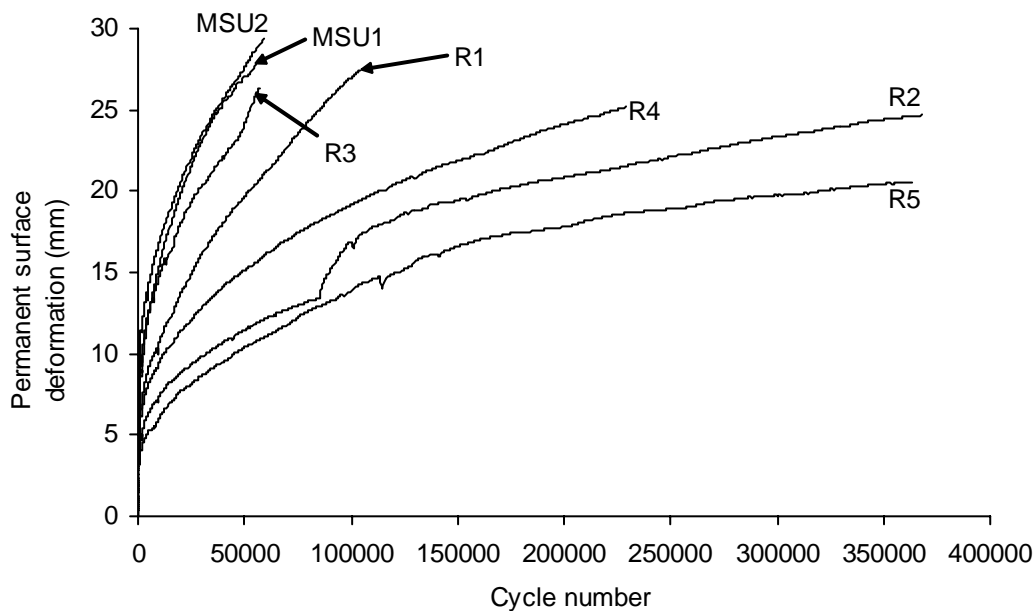


Figure 7.2.1 Permanent surface deformation vs. load cycle for R sections.

8.0 RESULTS: GTX TEST BOX

8.1 Response of Unreinforced Sections

Four unreinforced sections were constructed in the test box located at GTX. As illustrated in Section 5, quality control of constructed test section properties was good and to a level comparable to other test sections described in this report and reported earlier by Perkins (1999). As illustrated in Figure 8.1.1, significant differences in pavement response were observed between the four control sections. Test sections GTX1, GTX 2 and GTX4 were constructed with a subgrade target moisture content of 28 % and yielded average construction water contents of 28.3, 28.9 and 28.7 %, respectively. Test section GTX5 was constructed at a slightly lower target water content of 27 % and yielded an in-place average value during construction of 26.7 %. This

test section was constructed at a lower water content in an attempt to avoid some of the pore water pressure problems seen in GTX1, 2 and 4 as illustrated below.

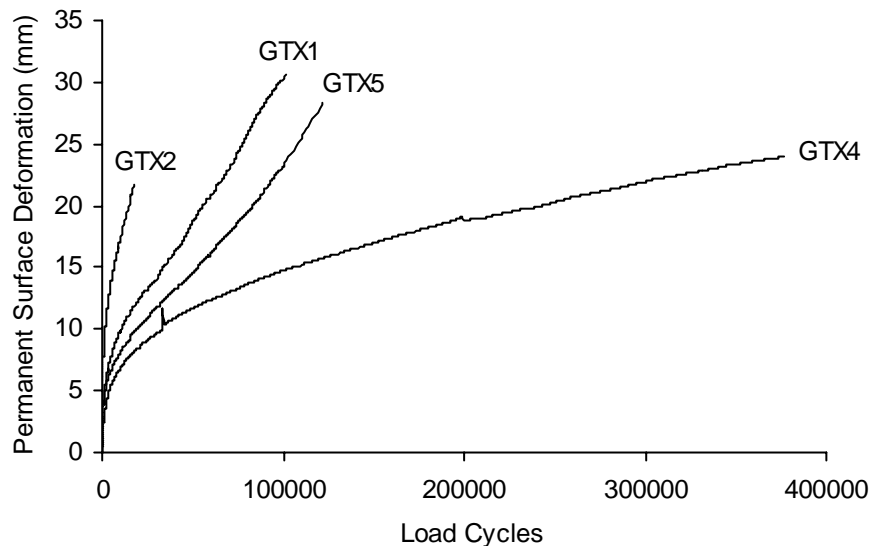


Figure 8.1.1 Permanent surface deformation vs. load cycle for GTX unreinforced sections.

Figures 8.1.2-8.1.4 illustrate pore water pressure data from the control sections at three different locations in the subgrade. Pore pressure sensors were not included in test section GTX1. This data illustrates several issues that impact the interpretation of results from this phase of the testing program. First, the sections start at a positive pore water pressure reading for the three locations examined. Since free water is not available in the subgrade, the positive pore water pressures observed at the start of loading are a result of pressures generated during the construction process. Figure 8.1.5 shows pore water pressure response during construction for test section GTX5 at the location of the sensor at $x=y=0$ and $z=675$ mm. Elapsed time begins at the time the sensor was placed. Figure 8.1.5 shows that pore pressure immediately after placement is slightly negative but then increases significantly during compaction of the subgrade, with subsequent increases seen after compaction of the base and the asphalt concrete. Between the compaction operations and after construction it is seen that pore water pressure gradually decreases. These results indicate that starting values of pore water pressure are dictated by the amount of compaction energy that takes place in each section, the time required for the construction process, and the time allowed at the end of construction before loading begins.

Compaction effort was relatively constant for the subgrade and base layer constructions, however the asphalt concrete was compacted until the target density was reached, which could vary between sections. Construction time and wait time between end of construction and start of loading was maintained as constant as possible, however, equipment breakdown, pavement material availability and work schedules created differences in these times for the sections constructed.

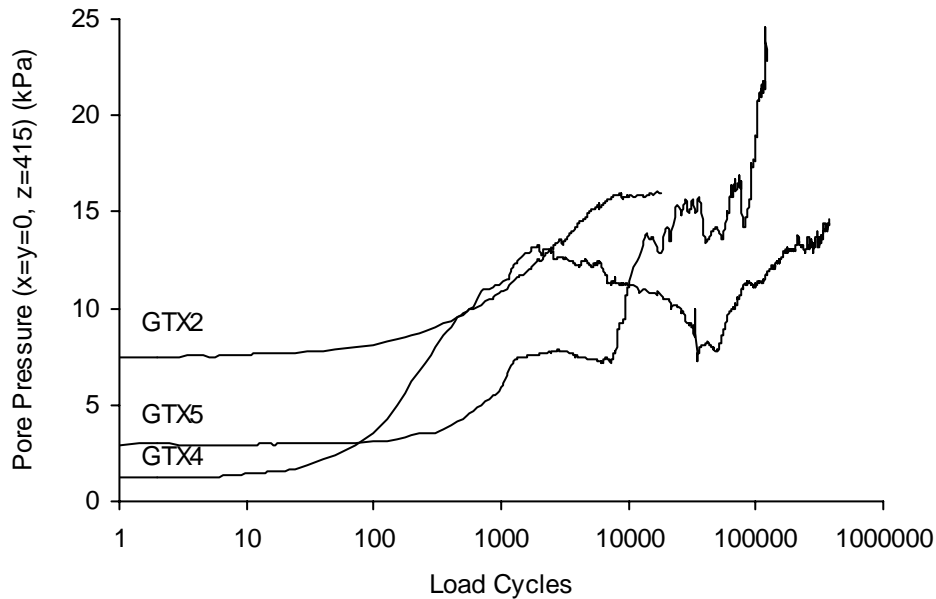


Figure 8.1.2 Pore water pressure vs. load cycle for GTX unreinforced sections at location $x=0$, $y=0$, $z=415$ mm.

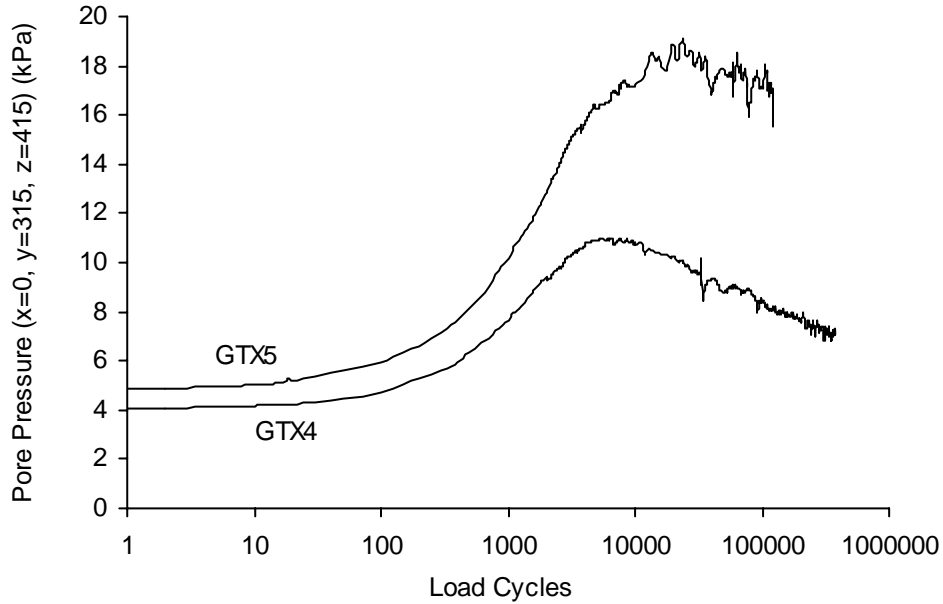


Figure 8.1.3 Pore water pressure vs. load cycle for GTX unreinforced sections at location $x=0$, $y=350$ mm, $z=415$ mm.

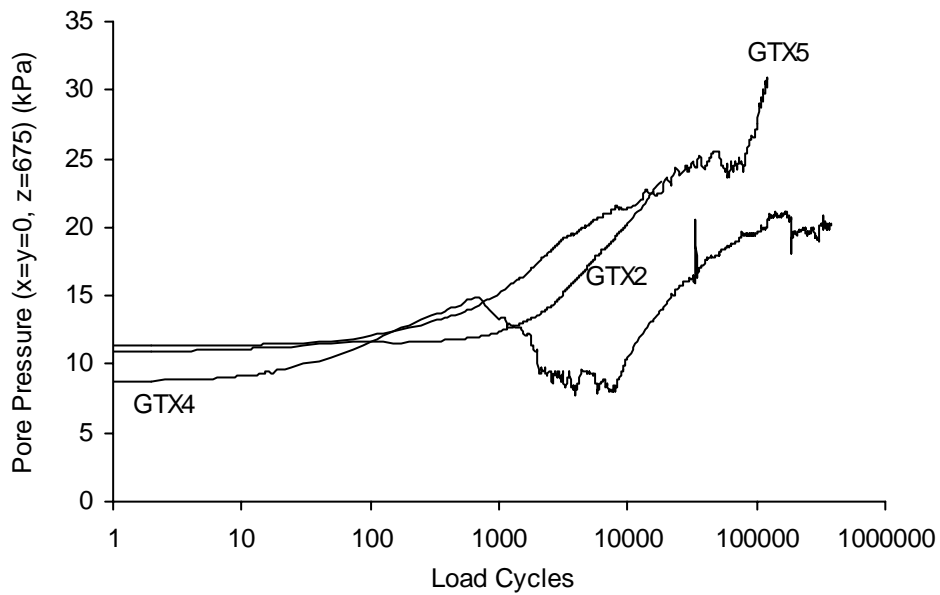


Figure 8.1.4 Pore water pressure vs. load cycle for GTX unreinforced sections at location $x=0$, $y=0$, $z=675$ mm.

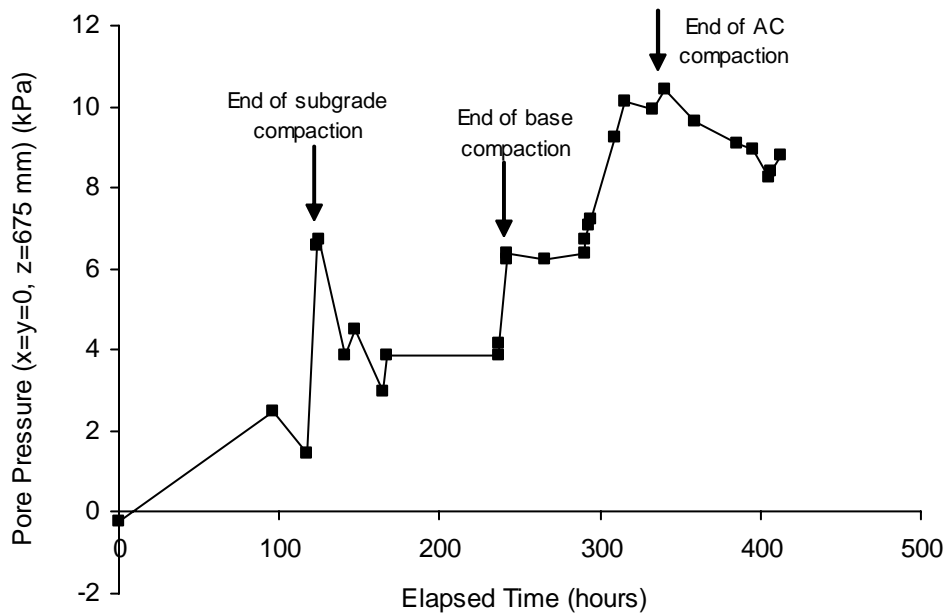


Figure 8.1.5 Pore water pressure vs. time during construction for GTX5 at location $x=0, y=0, z=675$ mm.

The next point to observe from Figures 8.1.2-8.1.4 is that the starting value of pore water pressure strongly influences the magnitude of pore water pressure during the test. Comparison of pore water pressure results to rutting behavior seen in Figure 8.1.1 indicates that the magnitude of pore water pressure generation and rutting are directly linked.

The time between the end of construction and the start of loading dictates the amount of pore water pressure dissipation. Figure 8.1.6 shows the relationship between the starting value of pore water pressure and the number of days from the end of subgrade construction to the start of loading for the sensor located at $x=y=0, z=415$ mm. Performance of the test section defined in terms of the number of load cycles necessary to reach 25, 20 or 12.5 mm of permanent surface deformation is also strongly related to the time between finish of construction and loading as illustrated in Figure 8.1.7.

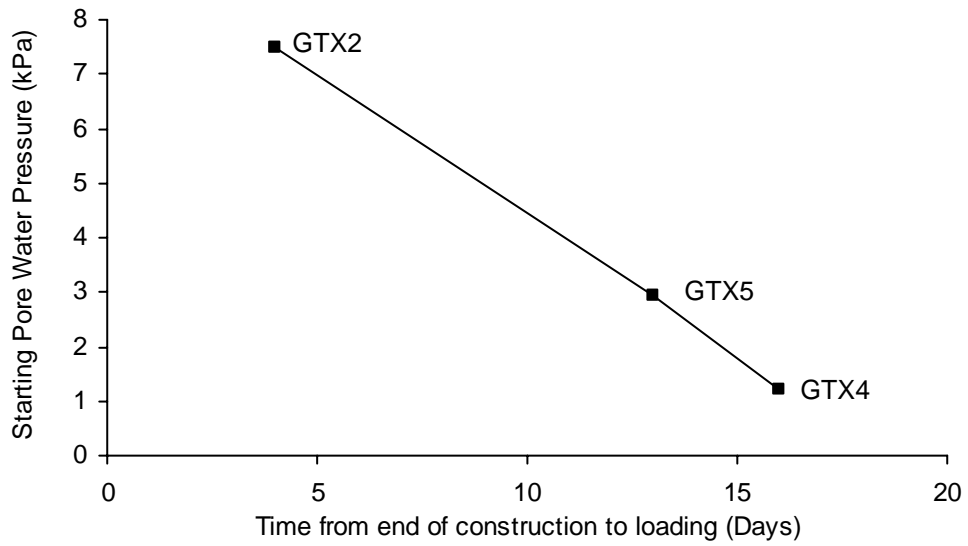


Figure 8.1.6 Starting value of pore water pressure vs. time from end of subgrade construction to start of loading.

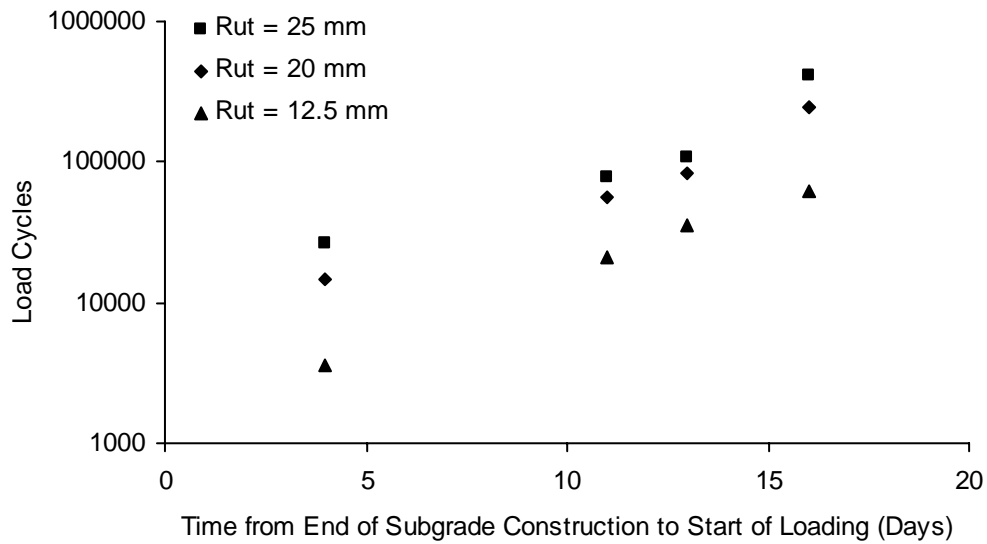


Figure 8.1.7 Load cycles for 25, 20 or 12.5 mm rut vs. time from end of construction to start of loading for unreinforced sections.

While the time between the end of subgrade construction and the start of loading influences the starting level of pore water pressure and the magnitude to which pore water pressure generates during pavement loading, other factors such as material set up may also be responsible for pore water pressure generation during loading and subsequent rutting behavior. Figure 8.1.8 shows the response of four reinforced sections having a nearly identical starting value of pore water pressure. The labeling of these sections is unique to Figures 8.1.8 and 8.1.9. The results indicate a unique relationship between pore water pressure generation and rutting behavior up to a certain point in the loading process. Figure 8.1.9 shows a plot between the number of load cycles necessary for 25, 20 and 12.5 mm of rutting versus time from the end of subgrade construction to the start of loading for three of these sections. These results show a similar relationship to that seen in Figure 8.1.7 indicating that the set-up time of the subgrade also influences the maximum pore water pressure that will develop during test section loading. Additional results to illustrate this effect are given in Section 8.2.

From the results of the unreinforced sections, it is seen that the subgrade used in these test sections readily develops positive pore water pressure during construction and pavement loading and that the magnitude of pore water pressure generation has a significant impact on pavement response defined in terms of rutting. The magnitude of pore water pressure generation during pavement loading appears to be dependent on the initial value of pore water pressure at the start of loading and the set-up time of the subgrade. The initial pore water pressure in turn appears to be dependent on the amount of compaction energy imparted to the constructed layers, the time for construction, and the time between end of construction and start of loading.

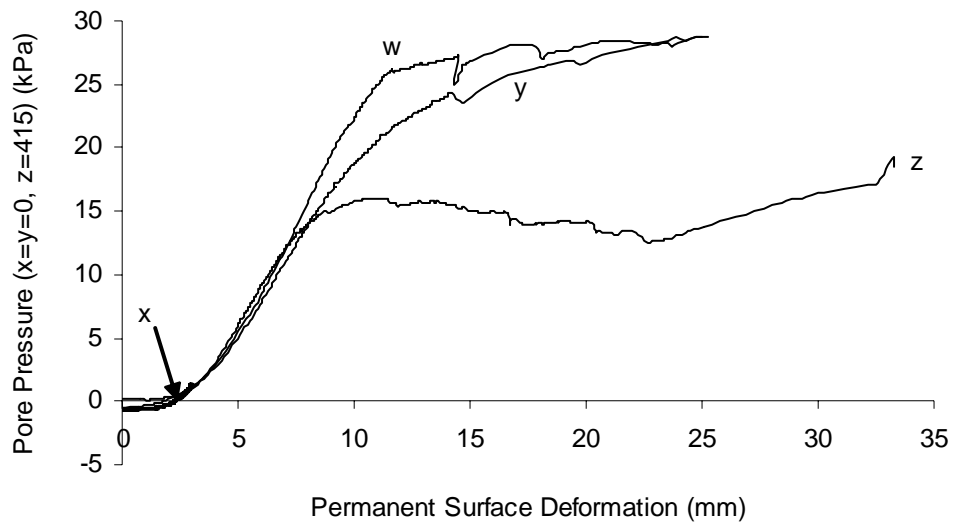


Figure 8.1.8 Pore water pressure vs. rutting for four reinforced sections.

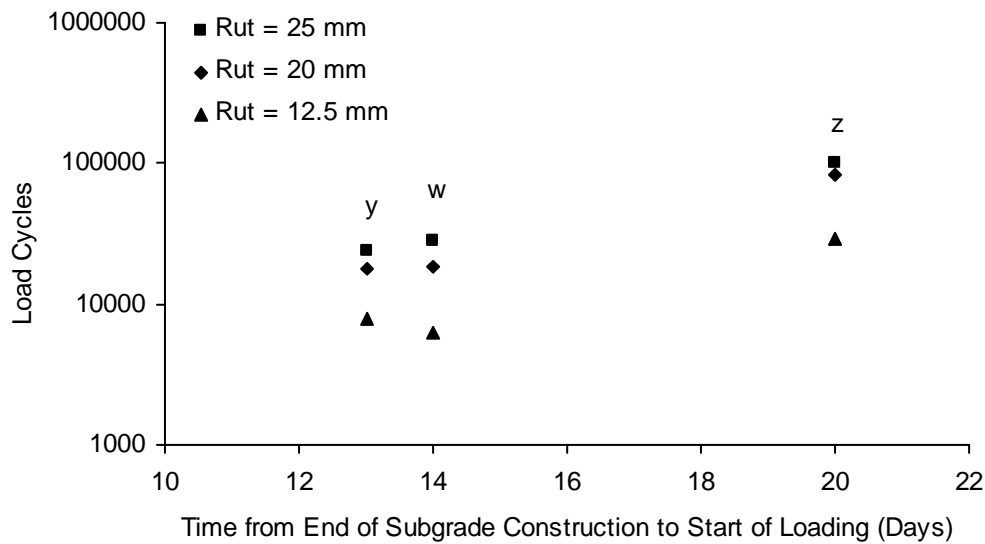


Figure 8.1.9 Load cycles for 25, 20 or 12.5 mm rut vs. time from end of construction to start of loading for three reinforced sections.

8.2 Response of Reinforced Sections

Evaluation of the reinforced sections is complicated by the pore water response issues discussed above. Figure 8.2.1 shows pore water pressure at the location $x=y=0$, $z=415$ mm for two reinforced sections constructed with different times between end of subgrade construction and

start of loading as noted on the figure. While each section shows a different starting value, the more significant characteristic of these figures is the difference in maximum pore water pressure seen during the course of loading. The section with the longer wait period shows a much lower maximum pore water pressure value. Figure 8.2.2 shows the same sections where pore water pressure is plotted against rut depth. Each section initially develops pore water pressure at approximately the same rate with rutting, however the section with the longer wait period time reaches a point where pore water pressure no longer develops but begins to decrease.

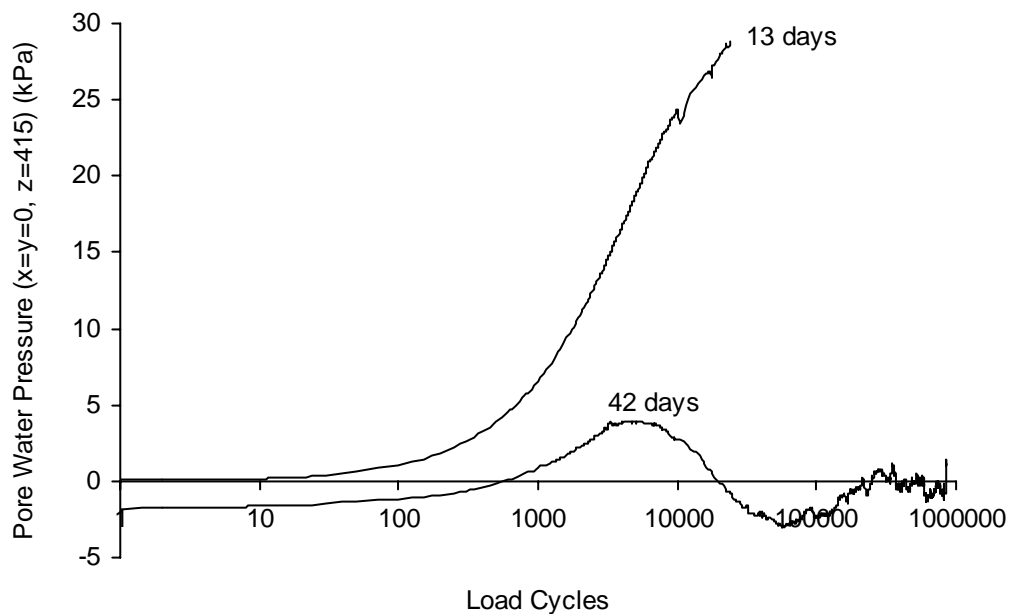


Figure 8.2.1 Pore water pressure vs. load cycles for two reinforced sections at different loading times.

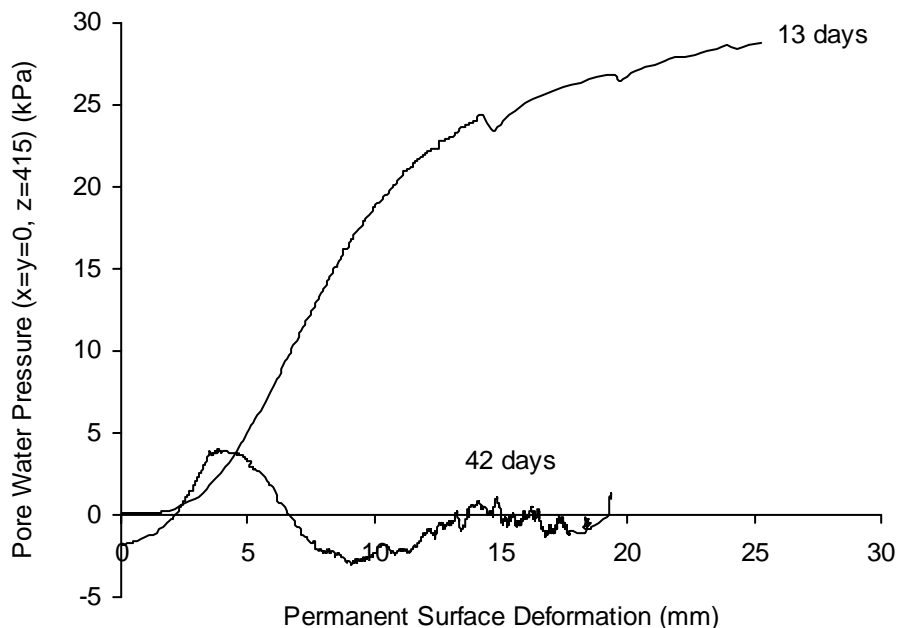


Figure 8.2.2 Pore water pressure vs. rutting for two reinforced sections at different loading times.

The number of load cycles necessary to reach 25, 20 and 12.5 mm of rutting is plotted against the time from the end of subgrade construction to the start of loading in Figure 8.2.3 for 5 of the reinforced sections. Number of load cycles necessary to reach 3 mm of rutting for 7 reinforced sections is also plotted in Figure 8.2.3. The data in this figure should not necessarily be expected to fall on a smooth curve as differences in geosynthetics should influence the amount of load cycles necessary to reach a given rut level. Given that the data does appear to fall on a relatively smooth curve is another indication that the performance of the test sections was largely governed by the pore water pressure issues discussed above.

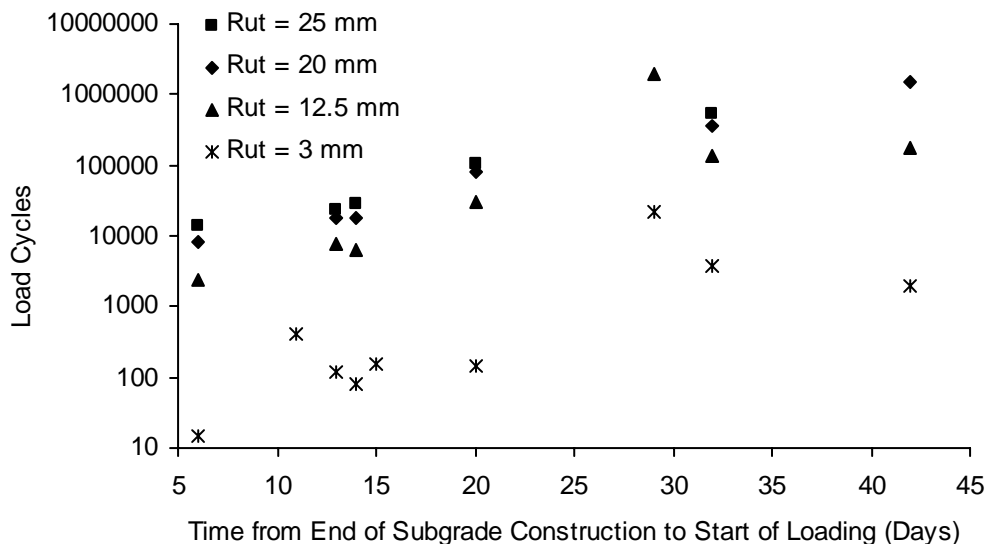


Figure 8.2.3 Load cycles for 25, 20 or 12.5 mm rut vs. time from end of construction to start of loading for 5 reinforced sections.

Testing protocols were established during the sequence of testing to address the pore water pressure issues that were discovered as the testing progressed. Starting with test section GTX5, the target moisture content was lowered to 27 %. This was done in an attempt to move the soil further from a fully saturated state and thus lessen the chance for pore pressure development during loading. Beginning with test section GTX6, it was recognized that the initial pore water pressure in the sections had an influence on rutting behavior. Time between the end of construction to start of loading was provided to allow initial pore water pressure from all the sensor locations to equilibrate back to a common level comparable to GTX5.

It was discovered that this process took different lengths of time and led to different degrees of material set-up which in turn influenced subsequent pore pressure development and rutting. For one reinforced test section, a delay in loading caused by the unavailability of asphalt material and holidays required a very long period of time between end of subgrade construction and start of loading (42 days). Considerably better performance of this section was noted. From the evaluation of data as presented in Figure 8.2.3, it became apparent that set-up time had an influence on test section performance and that large set-up times were required to obtain results that could be compared.

Beginning with test section GTX10, a two-stage loading program was established to verify the observations made above and to provide sufficient set-up times to allow comparison of

results. Test sections were constructed following a time schedule that was as close as possible to the number of days used for the majority of the sections from GTX5 onwards. This target time was 6 days from start to finish of construction. During this time, pore water pressure was closely monitored. The section was then allowed to sit such that the time from the end of subgrade construction to the start of the 1st loading was as comparable as possible between sections. This target time was 15 days of total time from end of subgrade construction to start of the 1st loading. It was expected that initial pore pressure would then be relatively constant between the sections. For sections GTX10 and GTX 11, 11 and 15 days were provided between end of subgrade construction and start of 1st loading, respectively. Comparison of initial pore pressure between sections GTX10 and GTX11 showed that pore pressure was slower to dissipate in section GTX11 resulting in higher initial pore pressures at the start of 1st loading. Given the additional changes in response that were observed with differences in set-up time, it was decided to begin the first loading at the target wait period.

The first loading of sections GTX10 and GTX11 was sufficient only to produce 3 mm of permanent surface deformation. This first loading was done primarily to confirm earlier findings that response was poor when set-up time was relatively low and secondarily to provide some conditioning to the pavement section. Results from these sections are contained in Figure 8.2.3 along with results of other reinforced sections and align with other findings. The sections were then allowed to sit for an additional 15 days, giving a total time from end of subgrade construction to start of loading of 29 and 32 days for GTX10 and GTX11. The sections were then loaded until 25 mm of surface deformation or 1 million load cycles was reached.

Figure 8.2.4 shows the response of sections GTX5 and for the first loading of GTX10 and GTX11. Comparison of sections within this diagram is not necessarily valid because the starting value of pore water pressure was different between each as illustrated in Figure 8.2.5. The results are presented together only to illustrate the relatively rapid development of pore water pressure and rutting for sections loaded at this level of set-up time.

Figures 8.2.6 and 8.2.7 show the response of sections GTX10 and GTX11 for the second loading. Like Figure 8.2.5, Figure 8.2.7 also shows that section GTX11 started at a higher pore water pressure as compared to GTX10 even though each section had approximately the same time between end of subgrade construction and start of each loading. This higher starting value of pore water pressure is partly responsible for the higher level of rutting seen in section GTX11.

Comparison of response between the first and second loading shows a much slower rate of rutting and pore pressure development and a limit to the maximum pore pressure that is developed before it begins to decrease. These results clearly indicate the importance of set-up time and initial pore water pressure on rutting response of the pavement.

To further substantiate the 2-stage loading technique, an additional control section is needed using this approach. Additional reinforced sections should then be constructed using this technique to provide useful comparisons between sections. Plans are in place for performing these sections. It is anticipated that these results will be issued as an addendum to this report.

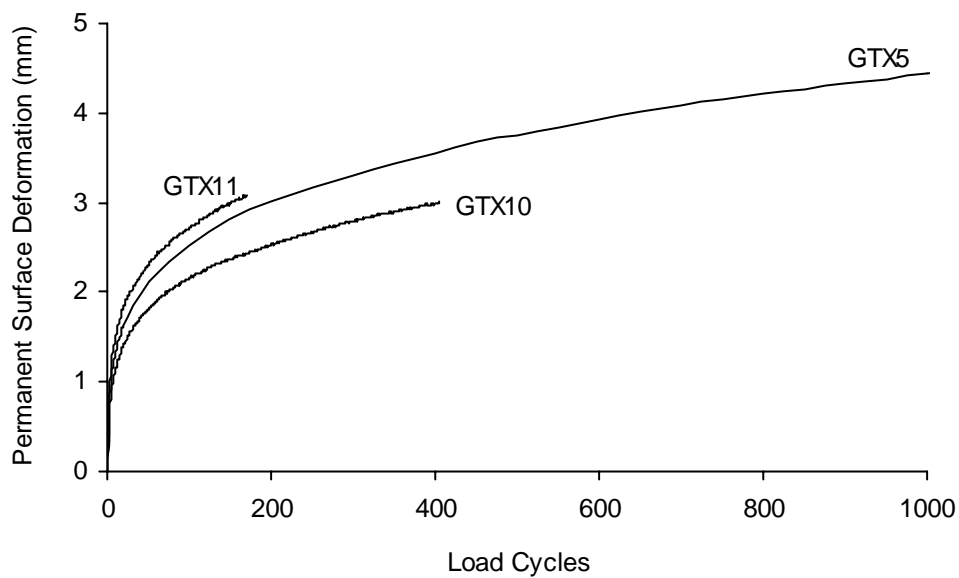


Figure 8.2.4 Rutting vs. load cycles for GTX5 and first loading of GTX10 and GTX11.

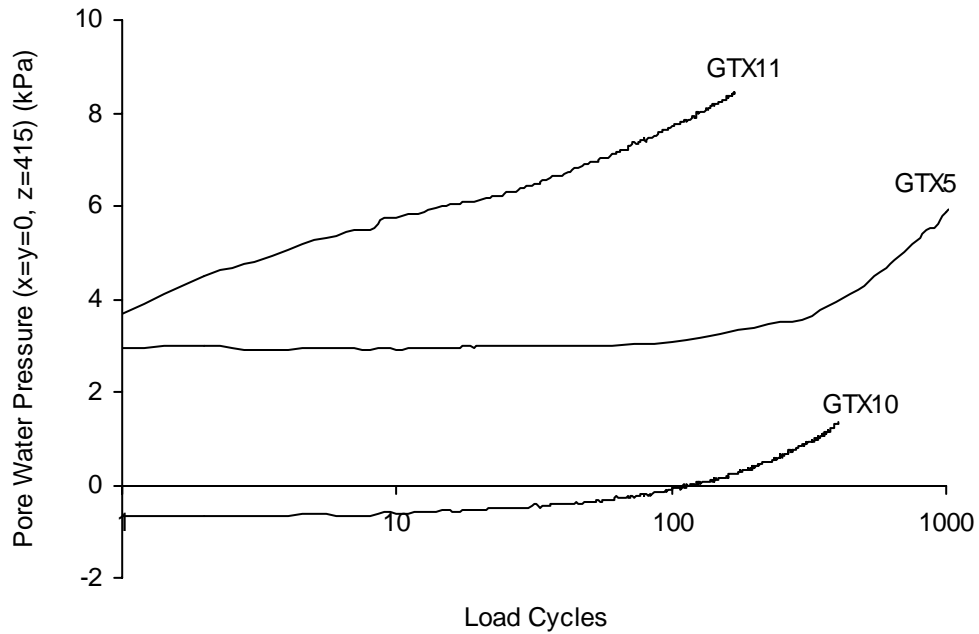


Figure 8.2.5 Pore water pressure vs. load cycles for section GTX5 and first loading of GTX10 and GTX11.

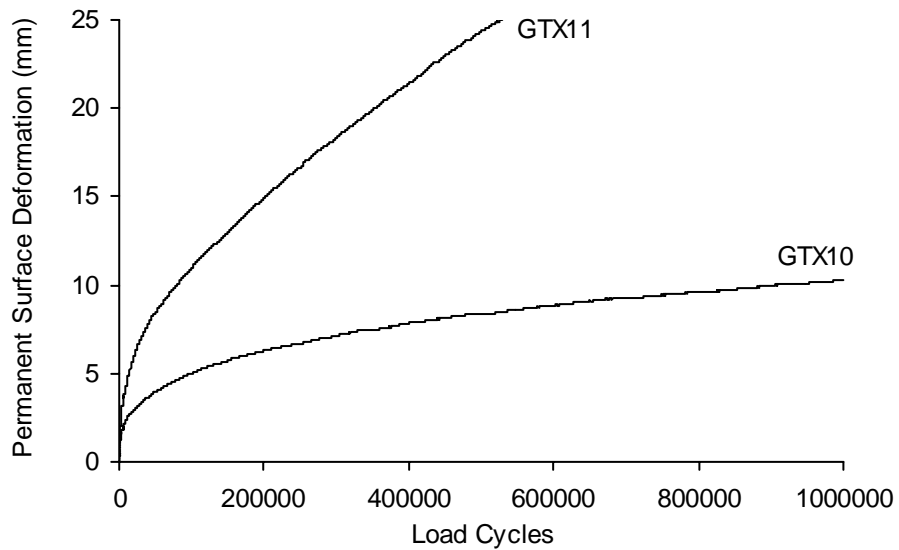


Figure 8.2.6 Rutting vs. load cycles for second loading of GTX10 and GTX11.

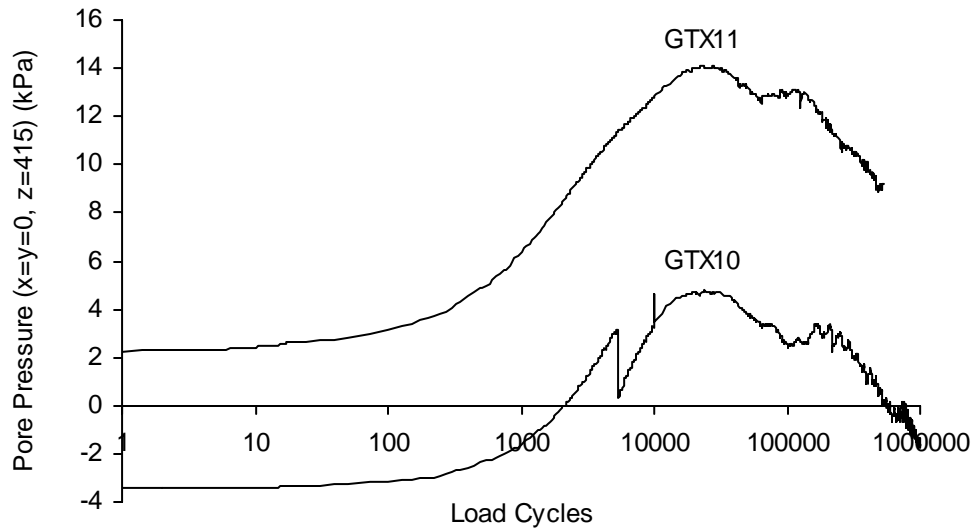


Figure 8.2.7 Pore water pressure vs. load cycles for second loading of GTX10 and GTX11.

9.0 CONCLUSIONS

Based on the work described in this report, the following conclusions are made:

1. Quality control measures taken during the construction and excavation of the test sections built in the CRREL, MSU and GTX test facilities indicated good control and reproducibility between the sections in a given test facility. Quality control measures were comparable to test sections described in an earlier project using the MSU test facility (Perkins, 1999).
2. The CRREL test sections loaded with a moving wheel load failed predominately by the development of surface rutting due to the development of permanent vertical strain in the asphalt concrete, base aggregate and subgrade layers.
3. Asphalt concrete cracking failures in two of the four test sections were due to delamination between the binder and surface courses due most likely to low material temperatures during paving.
4. The order of performance, as defined in terms of rutting, in the four CRREL test sections generally followed the same order observed in test sections described by Perkins (1999) using a cyclic load applied to a stationary plate. In order of increasing performance, the

CRREL sections gave CRREL1 (control), CRREL3 (geosynthetic A), CRREL2 (geosynthetic G) and CRREL4 (geosynthetic H).

5. The magnitude of reinforcement benefit, defined in terms of Traffic Benefit Ratio, was generally lower in the CRREL sections as compared to tests performed previously in the MSU test box. TBR values between MSU test box and CRREL sections was as follows: geosynthetic A: 8.5/9; geosynthetic G: 17/10; geosynthetic H: 56/32. The lower values in the CRREL sections for geosynthetics G and H may have been due to the sequence of test section loading and the development of pore pressure under sections CRREL2 and CRREL4 from prior loading of sections CRREL1 and CRREL3.
6. The determination of TBR was complicated by several sections showing an increase of deformation from one end of the section to the next. Forensic testing work did not provide any convincing evidence to indicate the cause for this. It is possible that the sequence of loading of the sections induced pore water pressures under adjacent sections negatively impacting their performance and leading to increased deformations at the ends of certain sections.
7. Stress and strain response measures from the CRREL test sections tend to show a marked difference between reinforced and unreinforced sections. The stress and strain measures showing a marked difference between reinforced and unreinforced sections included dynamic vertical stress on the top of the subgrade, dynamic vertical strain in the base and subgrade, dynamic transverse strain in the bottom of the base and top of the subgrade, and permanent vertical strain in the base and subgrade layers. Differences between the reinforced sections are apparent and tend to correspond to overall rutting behavior, but are not significant. Differences between reinforced sections tends to be more pronounced for permanent strain response than that seen for the dynamic stress/strain response
8. Reinforcement mechanisms observed from instrumentation placed in the CRREL test sections was similar in trend to that observed from test sections previously constructed in the MSU test box. These mechanisms included a reduction of horizontal strain in the bottom of the base and upper subgrade layers, greater spreading of vertical stress on the subgrade and reduction of dynamic and permanent vertical strain in the base and subgrade layers.

9. Test sections constructed with a reduced aggregate thickness in the MSU test box, where the reduced thickness was based on estimates using the 1993 AASHTO flexible pavement design equations and TBR values from previous test sections, indicated that the use of this approach is largely conservative except for conditions where the aggregate is excessively thin (less than 150 mm in thickness). Values of BCR predicted from the design model given in Perkins (2001b) are conservative with respect to the results obtained in this portion of the study.
10. Unreinforced test sections constructed with a rounded aggregate having a maximum particle size of 38 mm indicated superior performance as compared to unreinforced sections constructed with a crushed aggregate having a maximum particle size of 19 mm. The performance of reinforced sections using the rounded aggregate were generally inferior relative to those using a crushed aggregate. In addition, the order of performance to sections using two geosynthetic types was reversed when using the rounded aggregate. Results from direct shear tests yielding geosynthetic-aggregate interaction properties did not correspond to the results obtained.
11. An interaction shear modulus measured from direct shear tests on the geosynthetic-aggregate combinations used in this study provided insight into the behavior of test sections previously reported in Perkins (1999). Furthermore, the value of the reduction factor for interface shear used in the design model of Perkins (2001b) for the geosynthetics used in the previous test section study were substantiated by the direct shear tests. These results indicate that the direct shear test for the measurement of interaction shear modulus may be a useful tool in defining this reduction factor for interface shear.
12. While the use of direct shear tests to evaluate the interface shear modulus appeared to show promise, results with the rounded (MSU2) aggregate did not correspond to performance results from test sections. The lack of sample conditioning in this test also makes the modulus determined from the test susceptible to sample set-up procedures and conditions. A cyclic pullout test on short geosynthetic specimens is currently being examined as an alternate test.
13. The response of the test sections constructed in the GTX test box was dominated by pore water pressure generation due to several factors. The subgrade used in these test sections readily develops positive pore water pressure during construction and pavement loading.

The initial magnitude of pore water pressure prior to pavement loading has a significant impact on pavement response during loading as defined in terms of rutting. The magnitude of pore water pressure generation during pavement loading appears to be dependent on the initial value of pore water pressure at the start of loading and the set-up time of the subgrade. The initial pore water pressure in turn appears to be dependent on the amount of compaction energy imparted to the constructed layers, the time for construction, and the time between end of construction and start of loading.

14. Several sources of data point to an aging effect of the subgrade used in the GTX test sections. These sources include laboratory UU tests, portable FWD tests and vane shear tests. The aging effect (dictated by set-up time) appears to influence the generation of pore water pressure as load is applied.
15. The response of the majority of the reinforced sections constructed in the GTX test box were dominated by the pore water pressure issues described above. The last two sections constructed used a technique that involved two loading stages with a significant wait period in between. Results from the first loading stage when set-up time of the subgrade was relatively short showed a rapid development of rut depth and pore water pressure in the subgrade. Loading during the 2nd stage produced a much lower rate of rutting and pore pressure generation.
16. Additional unreinforced sections are needed using the GTX facility to show the relationship of performance for set-up times greater than 16 days and to establish a threshold time where set-up no longer influences performance behavior. Given the time needed for set-up, 2 months should be anticipated for the completion of one section. These tests are needed to further evaluate the utility of the 2-stage loading procedure.
17. Several reinforced sections need to be repeated using the protocol established for sections GTX10 and GTX11 such that valid comparison of sections can be made.
18. Sections corresponding to those described in items 16 and 17 are to be constructed after this report is finalized. It is anticipated that an addendum to this report will be issued and will contain the results of these sections.
19. The pore water pressure measurements in the GTX sections indicates the necessity of measuring pore water pressure in test sections involving materials that are close to 100 % saturated.

20. The pore pressure issues seen in the GTX sections point to the critical importance of pore water pressure on pavement performance and design. Additional research should be performed to examine pore water pressure build up in typical pavement conditions and methods for incorporating pore water pressure into pavement design methods.

10.0 REFERENCES

- Askegaard, V., Brink, A. and Ullidtz, P. (1997), "Pressure Cell Calibration Tests", *Transportation Research Board Annual Meeting Preprint*, Paper No. 970158.
- Janoo, V., Irwin, L., Knuth, K., Dawson, A. and Eaton, R. (1999), "Use of Inductive Coils to Measure Dynamic and Permanent Pavement Strains", *Proceedings of the International Conference on Accelerated Pavement Testing*, Reno, Nevada, USA.
- NCHRP (2000), *Harmonized Test Methods for Laboratory Determination of Resilient Modulus for Flexible Pavement Design, Volume 1, Unbound Granular Material*, NCHRP Project 1-28a Draft Report, 198p.
- Perkins, S.W. (2001a), *Numerical Modeling of Geosynthetic Reinforced Flexible Pavements*, Montana Department of Transportation, Helena, Montana, Report No. FHWA/MT-01/003/99160-2, 97p.
- Perkins, S.W. (2001b), *Mechanistic-Empirical Modeling and Design Model Development of Geosynthetic Reinforced Flexible Pavements: Final Report*, Montana Department of Transportation, Helena, Montana, Report No. FHWA/MT-01/002/99160-1A, 156p.
- Perkins, S.W. (2001c), *Mechanistic-Empirical Modeling and Design Model Development of Geosynthetic Reinforced Flexible Pavements: Appendix C - DARWin Output*, Montana Department of Transportation, Helena, Montana, Report No. FHWA/MT-01/002/99160-1B, 89p.
- Perkins, S.W. (1999), *Geosynthetic Reinforcement of Flexible Pavements: Laboratory Based Pavement Test Sections*, Montana Department of Transportation, Helena, Montana, Report No. FHWA/MT-99/8106-1, 140 p.
- Perkins, S.W. (1996), *In-Field Performance of Geosynthetics Used to Reinforce Base Layers; Phase I: Instrumentation Selection and Verification*, Montana Department of Transportation, Helena, Montana, Report No. FHWA/MT-96/8126-1, 160 p.
- Selig, E.T., Zhang, J. and Ebersöhn, W. (1997), "Evaluation of Dynamic Earth Pressure Cells for Subgrade", *Transportation Research Record 1596*, Washington DC, USA, pp. 1 - 6.
- Ullidtz, P., Askegaard, V. and Sjolín, F.O. (1996), "Normal Stresses in a Granular Material Under Falling Weight Deflectometer Loading", *Transportation Research Record 1540*, pp.24-28.
- Webster, S.L., Grau, R. and Williams, T. (1992), *Description and Application of Dual Mass Dynamic Cone Penetrometer*, Department of the Army, US Army Corps of Engineers.